Johann WALDAUF, BSc.

Development of a CFD Model for a Glass Melting Furnace with Electric Boosting

MASTER'S THESIS

to achieve the university degree of
Diplom-Ingenieur (Master of Science)

Master's degree programme:
Mechanical Engineering

submitted to

Graz University of Technology

Supervisor

Dipl.-Ing. Juraj Raič

Institute of Thermal Engineering
Head: Univ.-Prof. Dipl.-Ing. Dr.techn. Christoph Hochenauer

Graz, December 2020

Eidesstattliche Erklärung

Ich erkläre an Eides statt, dass ich die vorliegende Arbeit selbstständig verfasst, andere als die angegebenen Quellen/Hilfsmittel nicht benutzt, und die den benutzten Quellen wörtlich und inhaltlich entnommenen Stellen als solche kenntlich gemacht habe. Das in TUGRAZonline hochgeladene Textdokument ist mit der vorliegenden Masterarbeit identisch.

Affidavit

I declare that I have authored this thesis independently, that I have not used other than the declared sources/resources, and that I have explicitly indicated all material which has been quoted either literally or by content from the sources used. The text document uploaded to TUGRAZonline is identical to the present master's thesis.

_____	_____
Datum/Date	Unterschrift/Signature

Vorwort

Die vorliegende Masterarbeit wurde im Zuge einer Projektkooperation der Firma Messer Austria GmbH mit dem Institut für Wärmetechnik an der TU Graz erarbeitet. Ich habe mich für dieses Thema entschieden, da ich nach einer experimentellen Bachelorarbeit mein Kompetenzspektrum um den Bereich der numerischen Simulation erweitern wollte. Außerdem ermöglichte die Aufgabenstellung einen Einblick in eine sehr interessante Industriebranche.

An dieser Stelle möchte ich mich beim gesamten Institut für Wärmetechnik, insbesondere bei Herrn Dipl-Ing. Juraj Raič, Herrn Dr. Christoph Schluckner und Herrn Univ.-Prof. Christoph Hochenauer für die Betreuung und Beurteilung dieser Arbeit bedanken. Ein besonderer Dank gilt den Betreuern für die sehr angenehme und freundschaftliche Zusammenarbeit, für die kurzfristige Verfügbarkeit bei Fragen sowie für die überaus schnelle und sehr gewissenhafte Vorkorrektur der Arbeit.

Insbesondere möchte ich bei dieser Gelegenheit aber auch einen großen Dank an meine Familie aussprechen, welche mich während meines gesamten Studiums, aber besonders während des erfolgten Hausumbaus neben der Durchführung der Masterarbeit tatkräftig unterstützt hat. Auch bei meiner Freundin, meinen Freunden sowie der Reisegruppe Sägewerk möchte ich mich für den absolut notwendigen sozialen Ausgleich zum Studium von ganzem Herzen bedanken.

Graz, Dezember 2020

Johann Waldauf

Kurzfassung

Titel: Entwicklung eines CFD Modells für einen Glasschmelzofen mit Electric Boosting

Autor: Johann Waldauf, BSc.

1. Stichwort: Glasschmelzofen
2. Stichwort: Systemkopplung
3. Stichwort: Computational Fluid Dynamics (CFD)

Bei der industriellen Glasherstellung erfolgt das Einschmelzen der Rohstoffe zumeist in großen Glasschmelzöfen. Diese Ofenbauart hat sich aufgrund ihrer kontinuierlichen Betriebsweise durchgesetzt. Ein Glasschmelzofen besteht im Wesentlichen aus einer Glaswanne und einer darüber angeordneten Brennkammer. Die Befeuerung der Brennkammer mit mehreren Brennern führt zu einer Erwärmung und zum Schmelzen des Glases in der darunterliegenden Glaswanne. Die festen Rohmaterialien werden dazu an der Oberfläche der Glaswanne eingebracht. In der Glaswanne erfolgt der Aufschmelzprozess und das Läutern der Glasschmelze. Zur zielgerichteten Steuerung dieses Vorgangs sind in der Wanne zusätzlich mehrere stabförmige, elektrisch beheizte Elektroden angeordnet. Die entstehende Glasschmelze wird am Wannenende zur weiteren Verarbeitung kontinuierlich abgeführt.

In der vorliegenden Arbeit wurde ein quer befeuerter Oxyfuel-Glasschmelzofen mit Electric Boosting untersucht, der einen verminderten Wärmeübergang zwischen der Brennkammer und der Glaswanne aufweist. Ziel dieser Arbeit war die Untersuchung der Einflussfaktoren auf den Wärmeübergang durch die Entwicklung eines leistungsfähigen CFD Modells. Dieses Modell berücksichtigte sowohl die Vorgänge in der turbulenten Gasphase innerhalb der Brennkammer als auch das Schmelzen der festen Rohstoffe und die laminare Strömung innerhalb der Glaswanne. Um den Einfluss von Verbrennungsmodellen, Absorptionskoeffizienten und Strahlungsmodellen in einer angemessen kurzen Zeit abschätzen zu können, wurde zunächst ein 2D Modell entwickelt. Dabei wurden aufgrund der hohen Viskositätsunterschiede zwischen der festen, flüssigen und gasförmigen Phasen im Glasschmelzofen die CFD Simulationen auf zwei unterschiedliche Systeme für die Brennkammer und die Glaswanne aufgeteilt. Die Interaktion dieser beiden Systeme wurde durch eine Koppelung an der Schnittstelle auf der Glasoberfläche erreicht. Die gewonnenen Erkenntnisse wurden anschließend auf ein gekoppeltes 3D

Simulationsmodell übertragen. Die Validierung dieses CFD Modells erfolgte anhand von Temperaturmessdaten, welche mittels Thermoelementen aus insgesamt sechs Messpunkten in den Brennkammer- und Glaswannenwänden des physischen Glasschmelzofens gewonnen wurden.

Die Simulationsergebnisse der Brennkammer und der Glaswanne in 2D bestätigten die gewählten Randbedingungen und Modelle. Statt einer Implementierung des Glases als nicht-grauer Strahler mit wellenlängenabhängigem Absorptionskoeffizienten, wurden für einen konstanten Wert von 125 1/m bereits Resultate mit hoher Genauigkeit und deutlich geringerem Rechenaufwand erzielt. Die Validierung des gekoppelten 3D Simulationsmodells ergab eine relative Temperaturabweichung von weniger als 5 % in allen sechs Messpunkten. Basierend auf den Temperatur- und Geschwindigkeitsfeldern wurde ein rasches Aufschmelzen des Glasgemenges und die Bildung des charakteristischen Strömungsfeldes in der Glaswanne beobachtet. In der Brennkammer hingegen wurden negative Effekte auf den Wärmeübergang in die Glaswanne festgestellt. Die negativen Effekte wurden durch konkrete Mängel in der aktuellen Konfiguration der Ofengeometrie und der Brennerkonstruktion hervorgerufen. Die Behebung der aufgezeigten Mängel kann nicht nur die Glasqualität erhöhen, sondern auch die Lebensdauer des untersuchten Glasschmelzofens.

Abstract

Title: Development of a CFD Model for a Glass Melting Furnace with Electric Boosting

Author: Johann Waldauf, BSc.

1st keyword: Glass Melting Furnace
2nd keyword: System Coupling
3rd keyword: Computational Fluid Dynamics (CFD)

In the industrial glass production, the melting of raw materials is performed in large-scale glass melting furnaces. These types of furnaces are predominately used due to their continuous operation mode. In a glass melting furnace the combustion chamber is arranged above the glass tank. The raw materials are added at the glass surface of the tank and are subsequently melted due to the heat of combustion from several burners inside the combustion chamber. Inside the glass tank the melting and refining process is controlled and additionally accelerated by electrically heated electrodes. The finished glass melt leaves the glass tank at the outlet of the refiner for further processing.

In the present work, a cross-fired oxy-fuel glass melting furnace with electric boosting was investigated, which is characterized by reduced heat transfer between the combustion chamber and the glass tank. The goal of this work was to investigate influencing factors on the heat transfer by developing an advanced CFD simulation model. This model considered the processes in the turbulent gas phase inside the combustion chamber as well as the melting of the solid raw materials and the laminar flow inside the glass tank. In order to estimate the influence of combustion models, absorption coefficients and radiation models, a 2D model was developed first. Due to large differences in viscosity between the solid, liquid and gaseous phases, the CFD simulations were split into two different subsystems, one for the combustion chamber and one for the glass tank. The heat transfer at the glass surface, which acts as an interface between these two systems, was modelled by adopting an iterative coupling method. Utilizing the implications from the 2D simulations, a coupled 3D simulation model was developed. The validation of the 3D CFD model was conducted using temperature measurement data from a total of six thermocouples, positioned in the walls of the combustion chamber and the glass tank of the physical glass melting furnace.

The simulation results of the combustion chamber and the glass tank in 2D confirmed the validity of the chosen boundary conditions and models. Instead of implementing glass as a non-gray body, highly accurate results with low computation cost were achieved for a constant absorption coefficient of 125 1/m. The validation of the coupled 3D simulation model showed a relative temperature deviation of less than 5 % in all six measurement points. Based on the temperature and velocity fields, a rapid melting of the glass batch and the formation of the characteristic flow field for a glass tank was observed. However, in the combustion chamber adverse effects on the heat transfer into the glass tank were observed. These negative effects were caused by a faulty configuration in the furnace geometry and the burner design. Eliminating these deficiencies would increase both, the glass quality as well as the overall service life of the glass melting furnace.

Acronyms

Symbol	Description
AR	Aspect ratio
AZS	Aluminia zirconia silica
CAD	Computer aided design
CFD	Computational fluid dynamics
CH_4	Methane
CO	Carbon monoxide
CO_2	Carbon dioxide
CV	Control volume
DBS	Density-based solver
DNS	Direct numerical simulation
DO	Discrete ordinates
FVM	Finite-volume method
LES	Large eddy simulation
N_2	Nitrogen
NO_x	Nitrogen oxides
O_2	Oxygen
PBCS	Pressure-based coupled solver
PBSS	Pressure-based segregated solver
PDF	Probability density function
RANS	Reynolds averaged navier stokes
RTE	Radiative transfer equation
SFM	Steady diffusion flamelet model
Si	Silica
TC	Thermocouple
WSGGM	Weighted-sum-of-gray-gases model

Nomenclature

Symbol	Description	Unit
Latin symbols		
a	Absorption coefficient	$[1/m]$
A	Cross-section area	$[m^2]$
a_{th}	Thermal diffusivity	$[m^2/s]$
c	Specific heat capacity	$[J/(kg\,K)]$
C	Molar heat capacity	$[J/(mol\,K)]$
C^+	Empirical constant	$[-]$
e	Specific total energy	$[J/kg]$
E_{abs}	Absolute deviation	$[K]$
E_{rel}	Relative deviation	$[\%]$
$\mathbf{f}$	Force density vector	$[N/m^3]$
h	Specific enthalpy	$[J/kg]$
H	Enthalpy	$[J]$
H_u	Lower heating value	$[J/kg]$
I	Radiation intensity	$[W/sr]$
k	Turbulent kinetic energy	$[m^2/s^2]$
k_c	Thermal conductivity	$[W/(m\,K)]$
L	Characteristic length	$[m]$
$\dot{m}$	Mass flow	$[kg/s]$
n	Refractive index	$[-]$
Nu	Nusselt number	$[-]$
p	Pressure	$[Pa]$
P	Electrical power	$[W]$
Pr	Prandtl number	$[-]$
Q_{EAS}	Equiangular skewness	$[-]$
Q_{EVS}	Equilateral-volume-based skewness	$[-]$
$\dot{q}$	Heat flux	$[W/m^2]$
$\dot{Q}$	Rate of heat flow	$[W]$
Re	Reynolds number	$[-]$
s	Length/thickness	$[m]$
T	Absolute temperature	$[K]$
U	Velocity	$[m/s]$
U_T	Overall heat transfer coefficient	$[W/(m^2\,K)]$
$\bar{u}$	Time-averaged component of the velocity	$[m/s]$
u'	Fluctuating component of the velocity	$[m/s]$
$u_{i,j,k}$	Component of the velocity vector	$[m/s]$
u^+	Dimensionless velocity	$[-]$

Symbol	Description	Unit
$\mathbf{u}$	Velocity vector	$[m/s]$
V	Volume	$[m^3]$
$\dot{W}$	Technical power	$[W]$
x	Position	$[m]$
y	Wall distance	$[m]$
y^+	Dimensionless wall distance	$[-]$
Greek symbols		
α	Heat transfer coefficient	$[W/(m^2\,K)]$
α_r	Absorptivity	$[-]$
Γ	Diffusion coefficient	$[m^2/s]$
δ	Boundary layer thickness	$[m]$
Δ	Difference between two states	$[-]$
ε	Turbulent energy dissipation rate	$[m^2/s^3]$
ε_r	Emissivity	$[-]$
θ	Solid angle	$[°]$
κ	Von Kármán constant	$[-]$
λ	Wavelength	$[m]$
μ	Dynamic viscosity	$[Pa\,s]$
μ_T	Eddy viscosity	$[Pa\,s]$
ν	Kinematic viscosity	$[m^2/s]$
ρ	Density	$[kg/m^3]$
ρ_r	Reflectivity	$[-]$
σ	Stefan-Boltzmann constant	$[W/(m^2\,K^4)]$
σ_s	Scattering coefficient	$[1/m]$
τ	Shear stress	$[N/m^2]$
$\boldsymbol{\tau}$	Stress tensor	$[N/m^2]$
τ_r	Transmissivity	$[-]$
τ_λ	Optical Thickness	$[-]$
ϕ	Arbitrary physical quantity	$[-]$
Indices		
∞	External flow	
0	Reference level	
abs	Absolute value	
CC	Combustion chamber	
$chem$	Chemical reaction	
$crit$	Critical value	
e	Equiangular	
ext	External	
F	Fluid	
FG	Flue gas	
GT	Glass tank	
in	Incoming	
int	Internal	
λ	Depending on wavelength	
m	Mean	

Symbol	Description	Unit
M	Molar	
Meas	Measured value	
max	Maximum	
min	Minimum	
out	Outgoing	
p	Constant pressure	
rel	Relative value	
Sim	Simulation value	
T	Thermal	
W	Wall	
x	Local quantity	

Contents

1 Introduction

Glass is a unique and indispensable material due to its optical properties and various application possibilities. Its applications range from window panes or mirrors, bottles and glasses, to high-quality crystal products for jewelry. The beginnings of glass production reach back to 1000 BC and production processes have been the subject of continuous improvements. However, the industrialization of glass production was significantly influenced by the invention of the continuously operating tank furnace in the 19th century. This invention made mass production of glass possible for the first time and led to an enormous increase in production [20].

Today's glass production takes place within the framework of recycling processes. In addition to new raw materials, a large proportion of cullet from float glass and bottle glass is remelted. Nevertheless, this recycling process requires an enormous amount of energy. While in 1928 the specific heat demand of a glass melting furnace was at 5600 kWh/t, this value decreased to 1100 kWh/t in modern melting furnaces [11]. Since the installed production plants are usually in operation for several decades, an adequate design and calculation of the system in advance is of utmost importance. In recent years, there has been a significant progress in the field of oxy-fuel combustion, which is particularly interesting for applications in high-temperature processes such as in the glass industry. The advantages of oxy-fuel combustion, apart from higher process temperatures, are mainly the elimination of measures for heat recovery and for binding of nitrogen oxides [6]. The development of a CFD model of the oxy-fuel fired glass melting furnace provides such a calculation tool for the optimization of the energy demand.

The aim of this work is to develop a detailed CFD model of an oxy-fuel fired glass melting furnace with electric boosting, which takes into account both, the processes in the gas phase inside the combustion chamber as well as the melting of the solid raw materials and the laminar flow inside the glass tank. With the CFD model the glass batch input, the glass melting process with the running reaction chemistry, the behavior of the glass flow in the glass tank as well as the oxy-fuel combustion and the formation of emissions in the furnace should be modelled. Due to the complex task, a working model should be developed first in 2D and finally transferred to 3D. This leads to lower computation cost and consequently to a shorter overall development time of the 3D CFD model.

2 Theoretical Basics

2.1 Heat Transfer

Heat transfer is the subject that deals with energy transfer as a result of temperature differences. From a thermodynamic point of view, energy transfer is a product of thermodynamic imbalances. Energy transfer is driven by the transport of either heat, other types of energy or mass. The first law of thermodynamics for an open, non adiabatic and stationary system is introduced in Equation (2.1). Furthermore, the equation shows that it is possible to transfer or convert energy, but not to produce or to destroy it.

$$\dot{Q} + \dot{W} = \dot{m} \cdot (h_2 - h_1) \tag{2.1}$$

Temperature differences between two or more phases or within a single phase are the driving force for heat transfer. Heat flows from areas of higher temperatures to areas of lower temperatures. Thermodynamics deals with systems in equilibrium [15]. In contrast, heat transfer provides information how energy is transferred between systems before they reach a new equilibrium. In literature heat transfer is classified into three different modes: Thermal conduction, thermal convection and thermal radiation [5].

2.1.1 Thermal Conduction

This mode of heat transfer takes place in solids, liquids and gases. When there is a temperature gradient within a body, heat transfer manifests itself in the form of heat conduction. The transferred heat per unit area $\dot{Q}_x/A$ is proportional to the temperature gradient $\partial T/\partial x$ in the direction of the heat flux. This is expressed in Equation (2.2), which is called Fourier's law of heat conduction. The constant of proportionality is the thermal conductivity k_c of the material and the negative sign consideres the second law of thermodynamics: Heat must flow in the direction of the temperature gradient from high to low temperatures.

$$\dot{q}_x = \frac{\dot{Q}_x}{A} = -k_c \cdot \frac{\partial T}{\partial x} \tag{2.2}$$

For a wall (thickness s, thermal conductivity k_c) between two systems with the surface temperatures $T_{W2} > T_{W1}$ the heat flux density is written in Equation (2.3) as:

$$\dot{q} = \frac{k_c}{s} \cdot (T_{W2} - T_{W1}) \tag{2.3}$$

2.1.2 Thermal Convection

In fluids, energy is not only transferred by thermal conduction, but also by convection. Convective heat transfer occurs between fluids and solids of different temperatures. At the surface of a solid wall surrounded by a fluid with different temperature the formation of a temperature profile normal to the wall surface is recognized. The temperature profile with the thickness δ_T is called thermal boundary layer. Replacing the wall thickness s in Equation (2.3) with δ_T leads to the convective heat transfer coefficient α as written in Equation (2.4).

$$\alpha = \frac{k_F}{\delta_T} \tag{2.4}$$

The coefficient k_F represents the thermal conductivity of the fluid. Equation (2.5) introduces the heat flux due to convection, with T_W representing the temperature of the solid wall and T_∞ representing the free stream temperature.

$$\dot{q} = \alpha \cdot (T_\infty - T_W) \tag{2.5}$$

There are two fundamental types of convective heat transfer:

- **Forced convection**
  The fluid flow is caused by external forces such as pumps or fans.

- **Natural convection**
  The fluid flow is caused by internal forces as a result of temperature dependent density gradients. In fluid mixtures density gradients also result from gradients in concentration.

For simple geometries and flow fields analytical calculations of α are possible. Unfortunately most industrial applications are too complex, so the values have to be determined experimentally or with simulation tools.

2.1.3 Thermal Transmission

A common effect is the transfer of heat between two fluids, which are separated by a solid. This process is known as thermal transmission. As shown in Figure 2.1, this process is characterised by convective heat transfer from the fluid to the wall on both sides of the solid and thermal conduction inside the solid.

The overall heat transfer coefficient U for the wall (thickness s, thermal conductivity k_W) in Figure 2.1 is expressed in Equation (2.6) similar to a parallel circuit of electric resistors.

$$U = \left[\frac{1}{\alpha_1} + \frac{s}{k_W} + \frac{1}{\alpha_2} \right]^{-1} \tag{2.6}$$
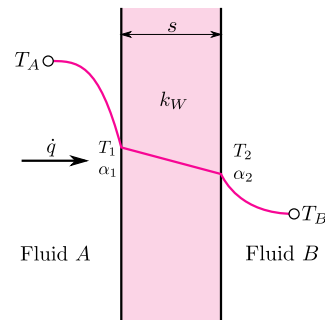
Figure 2.1: Overall heat transfer through a plane wall.

Subsequently, the resulting heat flux is calculated in Equation (2.7) by using the temperature difference of the fluids $T_A - T_B$.

$$\dot{q} = U \cdot (T_A - T_B) \qquad (2.7)$$

2.1.4 Thermal Radiation

At temperatures greater than absolute zero, every body emits energy via electromagnetic waves. Therefore this mode of heat transfer is called thermal radiation [5]. All previous modes of heat transfer were caused by interaction on the atomic level of media. In contrast, thermal radiation allows the transport of energy independently from media, even in vacuum.

On a body, the incident radiation is partly reflected, absorbed and transmitted as shown in Figure 2.2. Furthermore, the body emits a certain amount of radiation. Conservation of energy for the incident radiation leads to the balance in Equation (2.8). Division by the incident radiation in Equation (2.9) gives a better scale for the reflected (ρ_r), absorbed (α_r) and transmitted parts (τ_r) of radiation.
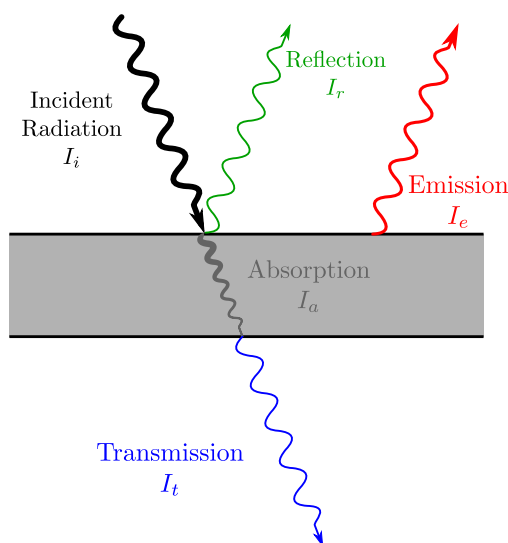

Figure 2.2: Radiation through a semi-transparent medium.

$$I_i = I_r + I_a + I_t \tag{2.8}$$

$$1 = \rho_r + \alpha_r + \tau_r \tag{2.9}$$

Intensity and wave length of the emitted radiation of a body depend on its temperature and material properties. So called black bodies are able to absorb all incident radiation and, depending on their temperature, to emit radiation at maximum intensity. The emitted radiation spectra of a black body are described by Planck's radiation law. For technical calculations the heat flux emitted from a black body with temperature T is a relevant variable. The heat flux is calculated with the Stefan-Boltzmann law in Equation (2.10) [7].

$$\dot{q} = \sigma \cdot T^4 \tag{2.10}$$

The constant σ in Equation (2.10) is called Stefan-Boltzmann constant and has a value of:

$$\sigma = 5.6696 \cdot 10^{-8} \frac{W}{m^2 \cdot K^4} \tag{2.11}$$

Not all bodies are able to emit radiation at maximum intensity. In several applications, bodies are assumed as gray bodies. A gray body is characterized by an equal level of absorption and emission independent of wavelength ($\alpha_r = \varepsilon_r < 1$). The emissivity ε_r represents the radiation intensity of a body compared to the radiation intensity of a black body.

The difference between absorbed and emitted radiation of a body yields a net heat flux. At a positive value the body absorbs more thermal radiation than it emits and the body temperature increases until a new state of equilibrium is reached. In equilibrium, that means at constant temperature, according to Kirchhoff's law of thermal radiation, the emissivity of a body is equal to its absorptance α_r [7].

For non-black bodies the emitted heat flux in Equation (2.12) is reduced by the emissivity of the body.

$$\dot{q} = \varepsilon_r \cdot \sigma \cdot T^4 \tag{2.12}$$

In addition to solids and liquids several gases with two or more atoms participate at thermal radiation. Thus, for the calculation of radiation in combustion processes, only heteropolar gases like water vapor (H_2O), carbon monoxide (CO) and carbon dioxide (CO_2) are taken into account. In general, gases absorb and emit radiation just in narrow wavelength bands. Subsequently, the approximation as gray body is not reasonable.

2.2 Fluid Mechanics

Most problems in fluid mechanics are directly related to heat transfer. In contrast, heat transfer can also be the reason of a developing flow. The type of heat transfer is highly depending on the present flow conditions. Incoming and outgoing heat fluxes influence the flow field significantly. Furthermore, the media in the system under consideration and their states have an influence on flow and heat transfer. This inseparable connection between heat transfer and fluid mechanics leads to the fact, that thermal and flow problems are always treated in parallel. In general, the fundamental equations of fluid mechanics already contain this connection.

2.2.1 Fundamental Equations

The basic principles of fluid mechanics are balance of mass, linear momentum and energy. These three basic principles are summarized in the fundamental equations of fluid mechanics. A descriptive representation of this set of equations is given by means of infinitesimal control volumes (CV) and the differential form of the fundamental equations derived at these volume elements. The Continuity Equation (2.13) represents the balance of mass. The Momentum Equation (2.14) and the Energy Equation (2.15) complete the set of equations. Further information can be found in the relevant literature [19, 28].

$$\frac{\partial \rho}{\partial t} + \nabla \cdot [\rho \mathbf{u}] = 0 \tag{2.13}$$

$$\frac{\partial}{\partial t} [\rho \mathbf{u}] + [\rho \mathbf{u} \mathbf{u}] \cdot \nabla = -\nabla p + [\boldsymbol{\tau} \cdot \nabla] + \mathbf{f_b} \tag{2.14}$$

$$\frac{\partial}{\partial t} (\rho e) + \nabla \cdot [\rho \mathbf{u} e] = -\nabla \dot{q}_s - \nabla \cdot [p \mathbf{u}] + [\boldsymbol{\tau} \cdot \mathbf{u}] \cdot \nabla - \mathbf{f_b} \cdot \mathbf{u} + \dot{q}_V \tag{2.15}$$

Only for simple problems it is possible to solve this set of equations analytically. For many engineering problems the equations can only be solved numerically.

However, the Ansys Fluent software used in this thesis is based on a finite volume solver which used a discretized form of the integral fundamental equations. The integral form of the conservation equation for a physical quantity ϕ is represented by the transport equation (2.16).

$$\frac{\partial}{\partial t} \int_V \rho \phi \cdot dV + \int_S \rho \phi \mathbf{u} \cdot n dS = \int_S \Gamma \nabla \phi \cdot n dS + \int_V q_V \cdot dV \tag{2.16}$$

The single terms can be interpreted as follows:

$$\frac{\partial}{\partial t} \int_V \rho \phi \cdot dV \quad \text{...Transient change within the CV}$$

$$\int_S \rho \phi \mathbf{u} \cdot n dS \quad \text{...Convective flow through the surface of the CV}$$

$$\int_S \Gamma \nabla \phi \cdot n dS \quad \text{...Diffusive flow through the surface of the CV}$$

$$\int_V q_V \cdot dV \quad \text{...Generation or dissipation in the CV}$$

2.2.2 Dimensionless Numbers

Writing the conservation equations in non-dimensional forms, leads to the dimensionless numbers that are very useful for performing parametric studies of engineering problems [19]. This enables the simple comparison of flows in model experiments, as well as significantly simplified solutions of similar flow fields. The derivation of the characteristic numbers is carried out by dimensional analysis of the differential form of the fundamental equations. They are calculated from geometrical and physical parameters of the flow. Some of the most important dimensionless numbers are reviewed below.

Reynolds Number

The Reynolds number in Equation (2.17) is the most frequently used number in fluid mechanics. With knowledge of the Reynolds number it can be determined whether a flow is laminar or turbulent. The transition region is characterized by a critical Reynolds number. The critical Reynolds number Re_{crit} represents the beginning of the transition from laminar to turbulent flow. The ratio in Equation (2.17) can be used as an interpretation for the Reynolds number. For small Reynolds numbers, as present in laminar flows, the damping effect of the viscous forces dominates. However, if $Re < Re_{crit}$, then the inertial forces are dominant in the flow field and the disturbances are further increased.

$$Re = \frac{U_\infty \cdot L}{\nu} = \frac{\text{Inertial forces}}{\text{Viscous forces}} \tag{2.17}$$

Furthermore, the fundamental equations can be simplified for very small or very large Reynolds numbers. The Reynolds number is calculated with the characteristic parameters of the geometry in the flow. These include the incident flow velocity U_∞, the caracteristic length L and the kinematic viscosity ν of the fluid.

According to Equation (2.18) the local boundary layer thickness δ_x of a laminar flow along a flat plate depends on the Reynolds number [22].

$$\frac{\delta_x}{L} = \frac{5}{\sqrt{Re}} \cdot \sqrt{\frac{x}{L}} \tag{2.18}$$

Prandtl Number

The Prandtl number can be interpreted as a material property. It is calculated in Equation (2.19) as the ratio of the momentum diffusivity (kinematic viscosity) and the thermal diffusivity a_{th}.

$$Pr = \frac{\nu}{a_{th}} = \frac{\text{Momentum diffusivity}}{\text{Thermal diffusivity}} \quad \text{with} \quad a_{th} = \frac{k_c}{\rho \cdot c_p} \tag{2.19}$$

In addition, it can also be interpreted in Equation (2.20) as the ratio of the boundary layer thicknesses of laminar flow and temperature.

$$Pr = \frac{\delta}{\delta_T} \tag{2.20}$$

Thus, for media with $Pr > 1$ the flow boundary layer is thicker than the thermal boundary layer. Conversely, for media with $Pr < 1$ the flow boundary layer is thinner than the thermal boundary layer.

Nusselt Number

This dimensionless number weights the heat transfer due to convection against the heat transfer due to conduction. The calculation of the Nusselt number in Equation (2.21) is based on the heat transfer coefficient α, the characteristic length L of the body and the thermal conductivity of the fluid k_F. Thus, at $Nu > 1$, thermal convection contributes more to heat transfer than thermal conduction. At $Nu < 1$, thermal convection contributes less to heat transfer than thermal conduction.

$$Nu = \frac{\alpha \cdot L}{k_F} = \frac{\text{Convective heat transfer}}{\text{Conductive heat transfer}} \tag{2.21}$$

The equation above does not yet give any indication of a relation between flow field and heat transfer coefficient. However, referring to Equation (2.4) the heat transfer coefficient α is influenced by the thermal boundary layer thickness. Via the Prandtl number as material property in turn there is a link to the flow boundary layer thickness. Finally according to Equation (2.18) the Reynolds number appears as influencing parameter. Therefore a relation between the individual dimensionless groups can be derived as written in Equation (2.22).

$$Nu = f(Pr, Re) \tag{2.22}$$

The determination of the heat transfer coefficient α with known Nusselt number, geometry and material properties is possible in some special cases. However, usually the heat transfer coefficient is determined by either empirical approaches, experimentally or by simulations.

2.2.3 Turbulence

Turbulence is still one of the greatest challenges in the field of fluid mechanics. Strong fluctuating movements normal to the flow direction are a characteristic feature of turbulent flows. In this case the flow can be formulated as the sum of a temporally constant mean value and a time-dependent value of fluctuations as described in Equation (2.23) [17].

$$u(x,y,z,t) = \bar{u}(x,y,z) + u'(x,y,z,t) \tag{2.23}$$

By inserting this relationship into the differential form of the Navier-Stokes equations in tensor notation, Equation (2.24) is obtained. It is well known as the so called Reynolds Averaged Navier Stokes equation (RANS).

$$\rho \left[\frac{\partial \bar{u}_i}{\partial t} + \frac{\partial}{\partial x_j} \left(\bar{u}_j \bar{u}_i \right) \right] = -\frac{\partial \bar{p}}{\partial x_i} + \frac{\partial}{\partial x_j} \left[\mu \left(\frac{\partial \bar{u}_i}{\partial x_j} + \frac{\partial \bar{u}_j}{\partial x_i} \right) - \rho \overline{u'_i u'_j} \right] \tag{2.24}$$

The mixed term $\rho \overline{u'_i u'_j}$ on the righthand side is denoted Reynolds Stress tensor. It is a symmetric tensor of second order with six components, which describe the unknown turbulent stresses. Turbulence modelling deals with the implementation of mathematical models for the Reynolds stress tensor [17].

2.2.4 Boundary Layer Theory

The boundary layer concept is based on the fact that flows at the wall must fulfill certain conditions. The no-slip condition means that the fluid velocity at the wall is equal to zero. The corresponding formulation for this is $U(y = 0) = 0$. In contrast, at a sufficient distance from the wall the free stream velocity $U = U_\infty$ is present in the external flow. The fluid temperature behaves similarly. At the wall it must be equal to the wall temperature with $T(y = 0) = T_W$, while in the external flow the free stream temperature $T = T_\infty$ is present [22].

In Figure 2.3 the course of the temperature and velocity profile are shown. The formation of transition zones in which temperature and velocity adapt to those of the external flow can be clearly seen. However, in the boundary layers there is no sharp separation between boundary layer and free external flow.
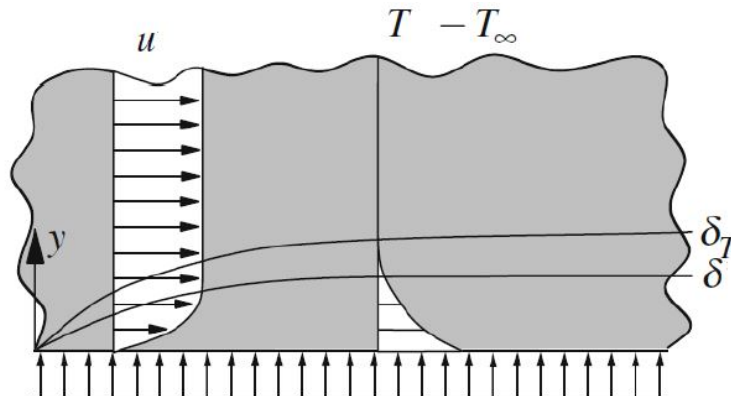

Figure 2.3: Development of the flow and thermal boundary layer on a flat plate [14].

An exact value for the thickness of the boundary layer cannot be given easily since the frictional influence in the boundary layer decreases asymptotically towards the external flow field. The thickness of the velocity boundary layer is defined by the relationship in Equation (2.25). This

means that the boundary layer extends from the wall to a distance with a flow velocity of $U = 0.99 \cdot U_\infty$.

$$\delta_{99} = y(U = 0.99 \cdot U_\infty) \tag{2.25}$$

The structure of the boundary layer in turbulent flows is more complex. In the viscous sublayer close to the wall there are only small flow velocities and thus small Reynolds numbers or a laminar region. At increasing distances from the wall the boundary layer flow changes into a turbulent flow. In the boundary layer model the boundary layer is divided into several layers. According to Schlichting et al. [22], the separation is done by means of the dimensionless wall distance. The shear stress on the wall of a flat plate oriented parallel to the flow field is represented by Equation (2.26).

$$\tau_W = \lim_{y \to 0} \mu \cdot \frac{\partial U}{\partial y} \tag{2.26}$$

With the help of the wall shear stress the dimensionless velocity can be formulated according to Equation (2.27).

$$u^+ = \frac{U}{U_\tau} \quad \text{with} \quad U_\tau = \sqrt{\frac{\tau_W}{\rho}} \tag{2.27}$$

Consequently, the dimensionless wall distance follows from Equation (2.28).

$$y^+ = \frac{y \cdot U_\tau}{\nu} \tag{2.28}$$

The turbulent boundary layer can be divided into an inner region ($0 < y < 0.2\delta$) and an outer region ($0.2\delta < y < \delta$). Based on the dimensionless wall distance the inner region can be divided into three zones, depending on the dimensionless velocity [2]:

1. **Viscous sublayer**
   For $0 < y^+ < 5$, linear correlation:
   $u^+ = y^+$

2. **Buffer layer**
   For $5 < y^+ < 30$, neither linear nor logarithmic correlation:
   Requires the implementation of mathematical models

3. **Fully turbulent region (log-law region)**
   For $30 < y^+ < 400$ ($y/\delta = 0.1 - 0.2$), logarithmic correlation (law of the wall):
   $u^+ = \frac{1}{\kappa} \ln(y^+) + C^+$

It should also be mentioned that the heat transfer coefficient in turbulent boundary layers is much higher than in laminar boundary layers due to the strong transverse movements, which results in strong convective mixing. Therefore, an accurate modelling of the boundary layers is of high importance, since even small deviations can impact the results greatly.

3 Basics in CFD

As mentioned in chapter 2.2.1, numerical methods have to be implemented to find solutions for existing (three-dimensional, turbulent, unsteady, etc.) flow problems. The numerical investigation is done by means of Computational Fluid Dynamics (CFD). This usually includes the numerical solution of the fundamental equations. The most established techniques are:

- Finite-difference method
- Finite-element method
- Finite-volume method

The software package used in this thesis – Ansys Fluent – is based on the finite-volume method (FVM). For that reason, only this method is now described in detail.

3.1 Finite-Volume Method

The key reason for the success of the finite-volume method is the principle of local conservation in CFD [2]. To solve the equations, the computational domain is spatially discretized with a grid. In the case of transient problems an additional temporal discretization is necessary. With the help of various mathematical models for simplification (turbulence models, radiation models, etc.) the fundamental equations are converted into algebraic equations. This step is called discretization. Subsequently these equations are solved by means of a solution algorithm which is also known as solver.

Thereby various input parameters are required to solve the problem:

- Material properties for solids and fluids
- Fundamental equations and models with appropriate model parameters
- Boundary conditions for the flow at the edge of the computational domain
- Initial conditions for start values in the domain
- Solver methods with parameters and solution controls

Subsequently, a qualitative presentation of the simulation results is provided by a large number of possibilities for graphical post-processing. A quantitative representation of the results in form of the solution values is possible as well.

3.2 Meshing

In CFD simulation, the flow variables are determined in a finite number of points in the computational domain. The calculation grid determines the spatial distribution of these points in the domain and on their edges. The computational domain is usually provided in the form of a geometry from a CAD programme. Grid generation, which is called meshing, is of great importance for the whole modelling process [23].

3.2.1 Types of Elements

Depending on the complexity of the geometry, but also on a manifold of other aspects, meshing is done in 2D as well as in 3D with cells of several different geometric types. In figure 3.1 the most common element types for mesh grids are shown.
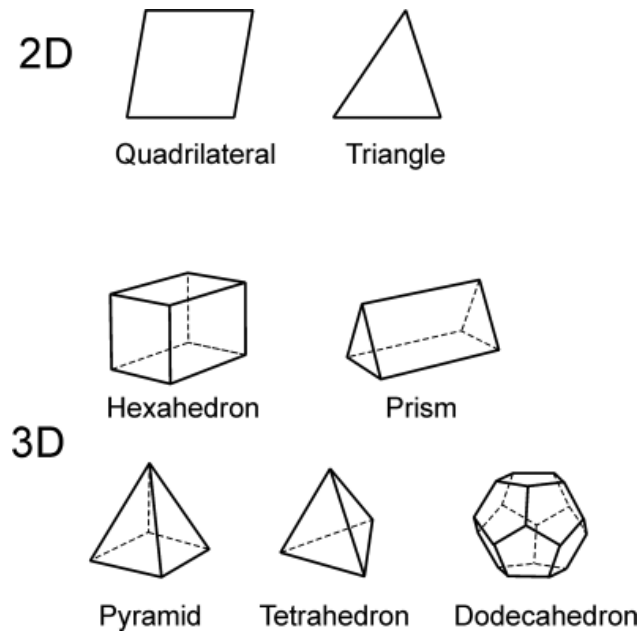

Figure 3.1: Element types for meshing in 2D and 3D [2].

Quadrilateral (short "Quad") elements in 2D and hexahedral (short "Hex") elements in 3D have the best properties for CFD. Structured grids are built only with such elements. Structured grids are characterized by a low number of elements, thus fast converging solutions with low memory requirements. Unfortunately more complex geometries are not realizable with structured grids. In addition to Quad and Hex elements, unstructured grids contain triangular (short "Tri") and tetrahedron-shaped (short "Tet") elements. In order to realize the transitions from Hex to Tet elements in the mesh grid, pyramid elements are used. Furthermore prismatic elements ("Wedges") with triangular base are used [2].

Even though Tets are characterized by their high flexibility, Hex or Wedges are prefered. In addition to their significanty lower cell demand, they also provide better convergence behavior and more accurate simulation results.

3.3 Mesh Quality

A grid with insufficient quality leads to large errors in the CFD model, which can lead to solutions with poor quality and at worst, cause a failure of the whole CFD simulation [23]. Even just one bad cell can lead to huge challenges for the solver. For this reason the mesh quality is of great importance. The quality of the mesh grid cells is described by the following criteria.

3.3.1 Skewness

For mesh quality, the skewness is one of the most important criteria. Skewness describes how close a cell is to ideal shape (equilateral or equiangular). It is divided into equiangular skewness (Q_{EAS}) and equilateral-volume-based skewness (Q_{EVS}). Equilateral-volume-based skewness applies only to Tet's. Since the equiangular skewness, formulated in Equation (3.1), is applicable to all cell shapes, it is the more representative quality measure.

$$Q_{EAS} = \max\left\{\frac{\theta_{max} - \theta_e}{\theta_e}, \frac{\theta_e - \theta_{min}}{\theta_e}\right\} \tag{3.1}$$

Here, θ_{max} represents the maximunm and θ_{min} the minimum edge angle of a cell. The angle of an equiangular cell is represented by θ_e (such as 60° for Tri and Tet, 90° for Quad and Hex). According to the definition of skewness, a value of 0 indicates an equilateral cell (best quality) and a value of 1 indicates a completely degenerated cell. The skewness of the worst cell in the grid should not exceed 0.9, while the mean value of the skewness should ideally be much lower [3].

3.3.2 Aspect Ratio

The aspect ratio (AR) describes the stretching of a cell. This measure is defined as the ratio of the distance from the cell centroid to the furthest corner to the normal distance from the cell centroid to the closest face [3]. Figure 3.2 depicts the aspect ratio for a cuboid element.
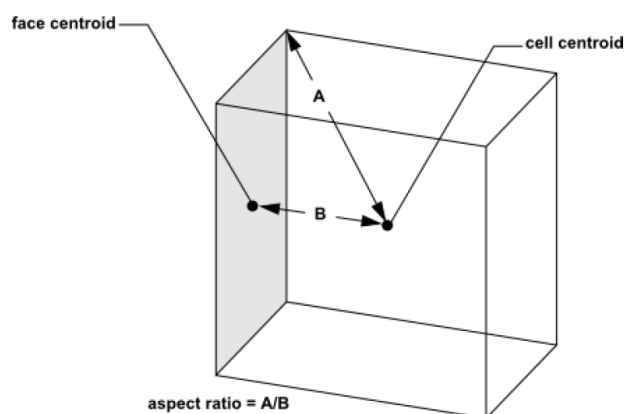

Figure 3.2: Definition of the aspect ratio [3].

In cells oriented in the flow direction, for instance in boundary layers, a much higher aspect ratio is acceptable than in unoriented cells. Nevertheless, the aspect ratio should not exceed a value of 100 as the absolute upper limit. Generally, it is best to avoid sudden and large changes of cell aspect ratios in areas where the flow field exhibits large changes or strong gradients [16].

3.3.3 Orthogonal Quality

This measure is computed with the normal vector of the face and the direction vector between the centroid of the cell and the neighbouring cell or the direction vector between the centroid of the face and the cell. The values of orthogonal quality are in the region of 0 (worst) to 1 (best), but should not fall below a value of 0.01. However, the average of all cells should be clearly at higher values. The inverse orthogonal quality is also commonly used as quality parameter. In this case a value of 0 means best quality and the value of the worst cell should be below 0.99 [3].

3.4 Modelling of Turbulence

In most technical applications, turbulent flows are present. For this phenomena, there are several model approaches. They are distinguished based on their resolved flow structures.

- **Direct Numerical Simulation (DNS)**
  This approach represents the computationally most expensive approach. The turbulent motion of the flow field is computed directly by solving the fundamental equations. In order to solve turbulence completely, a very fine mesh grid is necessary. Mesh grids which are fine enough to resolve the turbulence processes on a microscopic level are not computationally feasible in state of the art industrial applications. Since the computational demand is extremely high, it can be only handled with supercomputers, and as a consequence DNS is hardly used beyond research.

- **Large Eddy Simulation (LES)**
  This model is based on the computation of the spatially filtered continuity and Navier-Stokes equations. This means that only large-scale turbulence is resolved. The scale is determined by a previously selected filter width. Compared to DNS the fixed filter already reduces computing time by an order of magnitude. Nevertheless, for most applications LES is still to expensive.

- **RANS-based models**
  For these models the RANS equations are used to compute the mean flow and turbulence parameters. However, the effect of the unresolved turbulence on the mean flow must be approximated by a suitable turbulence model. The computational effort varies considerably between theses models. The following turbulence models are available:

  - **Reynolds Stress Models**
    With these models the individual components of the Reynolds stress tensor are computed algebraically or by means of transport equation models. Thus the directional

dependency of the turbulence is considered. However, the computational costs are high [18].

– **Eddy-Viscosity Models**
Based on the eddy-viscosity concept the Reynolds stresses are replaced by a turbulent viscosity, also known as eddy viscosity. The turbulence model can be seen as a set of equations to determine this viscosity. In industrial applications usually two-equation models are used [2].

Within the scope of this work, the realizable $k - \varepsilon$ model was used to model turbulence. It is an algebraic two-equation model based on the Boussinesq hypothesis. With this hypothesis the Reynolds stress term is modelled according to Equation (3.2) by introducing the eddy viscosity μ_T and the turbulent kinetic energy k [2].

$$-\rho \overline{u_i' u_j'} = \mu_T \left(\frac{\partial \overline{u_i}}{\partial x_j} + \frac{\partial \overline{u_j}}{\partial x_i} \right) - \frac{2}{3} \rho k \delta_{ij} \tag{3.2}$$

Two additional equations have to be solved, one for the turbulent kinetic energy and one for the turbulent energy dissipation rate ε. From these equations the eddy viscosity is computed. The eddy viscosity is not a material property, but a property of the turbulent flow [19]. The realizable $k - \varepsilon$ model is an improved version of the standard $k - \varepsilon$ model with better performance in complex flows [2].

In general, there is no unique path for the modelling of turbulence that can be applied to each flow problem. Which model is applied to a specific problem depends on various factors. On the one hand it depends on the available computational power, on the other hand on the flow properties. An important aspect is also the numerical stability of the individual models.

3.5 Modelling of Boundary-Layers

In laminar flows the boundary layer is modelled by a sufficiently fine mesh near the wall to account for the no-slip condition. As mentioned in Chapter 2.2.4, there are regions in turbulent boundary layers, where turbulence models for high Reynolds numbers cannot provide useful results. For modelling turbulence with algebraic models there are two approaches to consider the influence of the wall on the flow field [4]:

- **Near-Wall Model**
  In this approach the viscosity-affected region is resolved with a mesh all the way to the wall. A requirement for this is the use of a turbulence model, which is also suitable for small Reynolds numbers, for instance the $k - \omega$ model. Care must be taken to place the first cell at the wall in the range $y^+ = 1$. Further thin layers of grid cells must be applied. This results in a mesh with fine resolution within this region. The limits of cell growth and aspect ratio lead to a very high number of cells in the mesh, which increases the required computing power. The advantage of this method is the more accurate calculation of the boundary layer effects, including the occuring shear stresses and heat transfer coefficients [4].

- **Wall Functions**
  Here, the boundary layer effects are numerically modelled with the help of a wall function based on the data of the free external flow and semi-empirical relations. This method is often completely sufficient to consider the wall effect in the flow calculations. The use of wall functions is available in turbulence models for high Reynold numbers as the realizable $k - \varepsilon$ model.

- **Enhanced Wall Treatment**
  A combination of the two general approaches is implemented in the Enhanced Wall Treatment. The viscous sub-layer is resolved by the generated mesh, whereby the first cell can be placed at $y^+ = 5$. The remaining boundary layer is resolved by 10 to 15 further cell layers. The free external flow field is meshed without restrictions due to the boundary layer. This wall modell combines the advantages of the two models explained above [4].

3.6 Modelling of Radiation

The transport of thermal radiation in participating media is formulated by the Radiative Transfer Equation (RTE). It is given by the following equation:

$$\frac{dI(s,\omega)}{ds} = a\frac{\sigma T^4}{\pi} + \frac{\sigma_s}{4\pi} \int_0^{4\pi} I(s,\omega)\Phi(\omega)d\omega - (a + \sigma_s) \cdot I(s,\omega) \tag{3.3}$$

Looking at the individual terms of this equation, they can be understood as follows:

$$\frac{dI(s,\omega)}{ds}$$ ...Change of I along the path segment ds through the gas volume

$$a\frac{\sigma T^4}{\pi}$$ ...Change of I due to emission from surfaces

$$\frac{\sigma_s}{4\pi} \int_0^{4\pi} I(s,\omega)\Phi(\omega)d\omega$$ ...Change of I due to incoming scattering

$$(a + \sigma_s) \cdot I(s,\omega)$$ ...Change of I due to absorption and outgoing scattering

The optical thickness τ_λ is a criteria for the selection of the simulation model for radiative heat transfer. An optically thin or grey medium, for example air, is characterized by an optical thickness $\tau_\lambda \ll 1$. For $\tau_\lambda \gg 1$ optically thick media are described, for instance glass. Calculation of the optical thickness is done with the mean beam length L as characteristic geometrical dimension, the absorption coefficient and the scattering coefficient of the participating medium according to Equation (3.4). For many applications scattering is negligable ($\sigma_s = 0$).

$$\tau_\lambda = (a + \sigma_s) \cdot L \tag{3.4}$$

Since thermal radiation is transported from any emitting surface or cell at the speed of light to other cells or surfaces, modelling of radiation is rather complex. For the numerical CFD simulation this means interaction of all cells in the computational domain with each other. Different calculation models are used for this enormous number of interactions between the individual cells. Radiation models are, analogous to turbulence models, based on specific applications. These individual models are chosen according to the following aspects:

- Optical thickness of the medium
- Scattering in the medium
- Solids content of the medium
- Transparency and reflectivity of the walls
- Non-gray emitters in the computational domain
- Local heat radiation sources in the computational domain
- Non-participating media

In the scope of this work the following radiation models were examined in detail [4]:

1. **Discrete Ordinates (DO) Model**
   For solving the RTE with this model the solid angle is split up into a finite number of discrete directions. Using this angular discretization, the RTE is calculated in each quadrant (2D) or octant (3D) for N_θ x N_ϕ discrete ordinates as represented in Figure 3.3. The radiation intensity is assumed as constant within each segment of the solid angle. Thus, the number of transport equations to be solved depends on the number of solid angle segments. In the 3D case with eight octants 8 x N_θ x N_ϕ additional transport equations have to be solved. The larger the number of these angular segments becomes, the more computing time is needed for calculation.
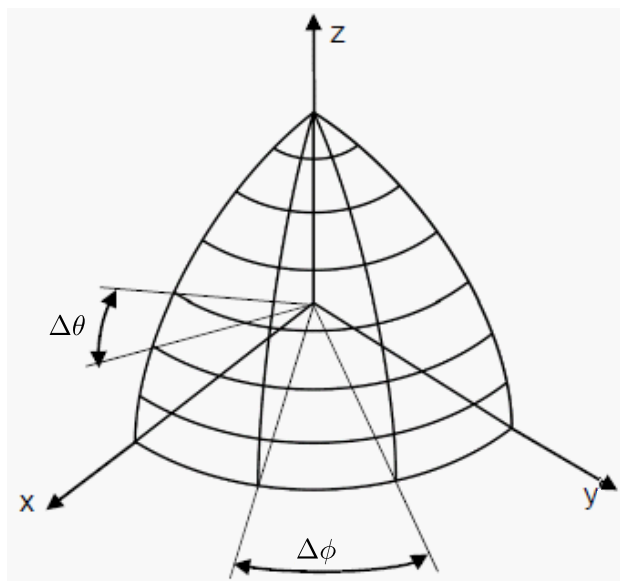

Figure 3.3: Angular discretization of an octant in solid angle segments.

The DO model is characterized by its wide range of applications. It works within the full range of optical thickness. Modelling of non-gray radiation is possible by means of a gray-band model as well as the consideration of scattering. Furthermore the DO model takes radiation exchange between gas and particles into account. Additionally radiation in semi-transparent walls and specular reflexion can be modelled [4].

2. **Rosseland Model**
   In this model radiative equilibrium is assumed in the medium and diffuse radiative heat transfer is implemented to the energy equation with a source term. Consequently, there is no demand for any additional transport equations and the computational effort for this model is insignificant. Application of the Rosseland model is limited for optically thick media with $\tau_\lambda > 3$. Furthermore, the model is suitable when taking scattering and the emissivity of walls into account [4].

3.7 Modelling of Combustion Processes

Combustion processes are a special kind of species transport and reaction chemistry problem. In CFD the transport and mixing of chemical species can be modelled by solving balance equations for convection, diffusion and reaction sources for each species [4]. This is possible for multiple simultaneous reactions in the fluid volume, on walls and particle surfaces. Currently a large number of CFD models for species transport and combustion are used for various applications. A distinction has to be made between models for reaction chemistry in process engineering on the one hand and models for combustion chemistry in the wide range of mechanical engineering on the other hand. Further insight into turbulent mixing and chemical reactions in CFD is given in relevant literature [2].

In this thesis the "Partially Premixed Steady Diffusion Flamelet" model, implemented in Ansys Fluent, was used to model combustion processes. This model calculates three additional transport equations. The first two transport equations treat the so-called mixture fraction and its variance. The last one consideres the reaction-progress variable C. At the inlets of fuel and oxidizer the progress variable is defined per definition as $C = 0$ and represents the unburnt mixture. At the maximum of $C = 1$ the progress variable describes the burnt mixture. Since these additional transport equations do not include any source terms, the model is called conservative. In principle, the complex processes, which are relevant for combustion, are simplified to a mixing problem. No equations have to be solved for single species. Instead, relations between the flow field and the chemical state are computed in advance and stored in the form of a Probability Density Function (PDF) table. Due to this preliminary step the simulation is accelerated because the results for the interaction between the flow field and the combustion are already available in a final form and only need to be read from the table by the solver [4].

In general, the mixing rate of the reactive species differs from the chemical reaction rate in the reaction volume. This results in non-equilibrium effects, which are considered by using the "steady flamelet" approach.

3.8 Solver

In the iterative solution procedure, the set of equations is solved in each cell. The minimum set of equations in CFD applications includes the continuity and momentum equation. Whether further equations for species transport, energy, turbulence, radiation and others have to be solved, depends on the models used. In the software package Ansys Fluent 19.0 three different types of solvers are implemented. The respective schemes of each solver are sketched in Figure 3.4.
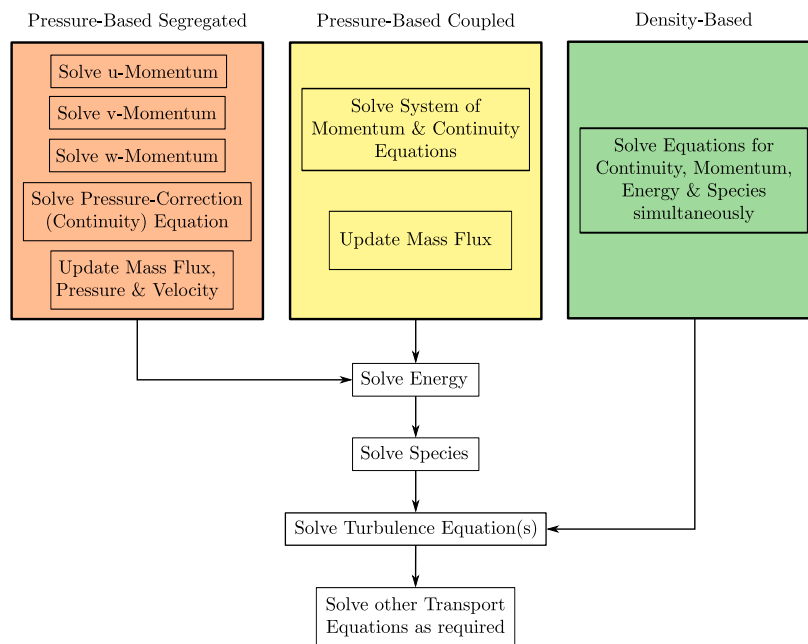
Figure 3.4: Solution procedures of the different solvers.

The Density-Based Solver (DBS) computes the set of equations together in vector form. Its application is limited to compressible flows. The basic equations are strongly coupled and significant density gradients can be determined. The pressure is computed via an equation of state.

When using the Pressure-Based Segregated Solver (PBSS) the fundamental equations are solved sequentially. The pressure is computed by means of a pressure-correction equation so that the velocity field fulfils the continuity equation. Subsequently the velocity field is updated. Except in transonic regions or at supersonic flow, Pressure-Based Solvers are suitable for a wide range of applications.

With the Pressure-Based Coupled Solver (PBCS) the continuity and momentum equation are solved simultaneously. Due to the more complex approach, computing time per iteration is increased, although a convergent result will often be achieved faster than with the PBSS. The PBCS is a very stable solution process which, however, has the disadvantage compared to the PBSS, that it requires about double the memory.

In this thesis the different fluids were assumed to be incompressible, therefore all computations were conducted with Pressure-Based Solvers.

3.9 Evaluating Convergence

Poor convergence is the most common reason for poor simulation results. A numerical method is said to be convergent if the solution of the discretized equations tends to the exact solution of the differential equation as the grid spacing tends to zero [13]. For the recording of the deviation of the solutions over the individual iteration steps, residuals are used. Based on these, it is possible to evaluate convergence.

A converged solution is found once the residuals fall below predefined values. Convergence is achieved once the residuals for the energy, radiation and species equations are below 10^{-6} and for the continuity and momentum equations below 10^{-3}. However, the residuals can rise again after further iterations and indeed the solution is not yet convergent. In some cases it can be also observed, that the residuals for a (more accurate) 2nd order discretization are orders of magnitude higher than for a (less accurate) 1st order discretization.

The evaluation of the residuals is not sufficient to judge the convergence of a solution. For instance, cells with poor grid quality in regions of secondary interest for CFD computation often lead to high residuals. However, these cells may not influence the solution in more relevant regions. For this reason, additional tools are used to assess convergence:

- **Monitors**
  The user can set up such monitors to record values of physical quantities that are of particular interest. For instance, mean wall temperatures, pressures or velocities at certain positions in the flow field may be monitored.

- **Flux Reports**
  With the help of flux reports the difference between incoming and outgoing fluxes can be determined quantitatively. This is especially useful when checking the mass and energy balance, based on Equation (2.13) and (2.15), respectively. The errors for mass and energy balance should not exceed 0.2 %.

In conclusion, a convergent result is not necessarily a physically correct result. The task of simulation software is to solve sets of mathematical equations iteratively. But the user has to find suitable models and boundary conditions which also reflect reality to a sufficient degree. It is essential that simulation results are checked for physical plausibility, grid independence and to validate them by means of experiments.

3.10 Error Influences in Simulation

All numerical approaches are based on iterative or approximative calculations of discretized equations and a discretization of the computational domain. The fundamental equations are not solved exactly. For this reason, deviations in the simulation results occur in the form of errors. Various sources of errors are described below [27]:

- **Discretization Error**
  This type of errors is due to the difference between the symbolically exact solutions of the governing equations and the approximated solution with discretized equations, mesh and time steps. In practice, proper meshing has the greatest impact on this kind of errors.

- **Round-Off Error**
  The difference between the true value of a quantity and the value of this quantity on the memory of a computer is called Round-off error. Due to a limited number of significant digits, each numerical value must be rounded off.

- **Convergence Error**
  Convergence errors exist due to the difference between the fully converged numerical solution and a numerical solution which has not fully reached convergence.

- **Pyhsical Modelling Error**
  These errors are due to inaccuracies in the formulation of the chosen models for turbulence, radiation, combustion processes, etc. Additionally, these types of errors includes simplifications of the physical geometry.

- **Human Error**
  All previous types of errors have numerical reasons. In contrast, human errors appear in two different forms. First, errors which concern human mistakes made by the programmers of the CFD software. These errors can be eliminated by systematic software test procedures. Second, application errors through the user due to improper meshing, inexperience in handling the various models, inadequate setting of boundary conditions. Nevertheless, human errors can be reduced with proper training and – even more important – the accumulation of experience.

Discretization errors and round-off errors account for the majority of the numerical error. They have the tendency to accumulate through computational processes and may yield unphysical CFD solutions [27]. In practice, it is not possible to determine the magnitude of the simulation error in a sufficient way.

However, a possibility is to check whether the two primary sources of errors have a significant influence on the total error. The discretization error is addressed thereby with grid independence studies. If these studies do not show significant differences, the discretization error is at an acceptable level. In contrast, the round-off error can be estimated quite easily by comparing the solutions for the solver options "single precision" and "double precision".

4 The Physical Glass Melting Furnace

For the large-scale industrial fabrication of glass products such as bottles, glass sheets for windows and screens or glass wool, liquid glass must be available without any interruptions. This continuous glass melting process is sketched in Figure 4.1. The glass batch consists of cullet from recycling and raw materials. It is fed into a glass melting furnace laterally from two inlets. For the melting of the batch and the heating of the glass melt, six gas burners are located in the combustion chamber. The glass melting furnace is closed at the top by a self-supporting domed structure, called furnace crown. In the glass tank a homogeneous glass melt is achieved after a sufficiently long time. After passing the throat and the refiner, the glass leaves the glass tank at the outlet.
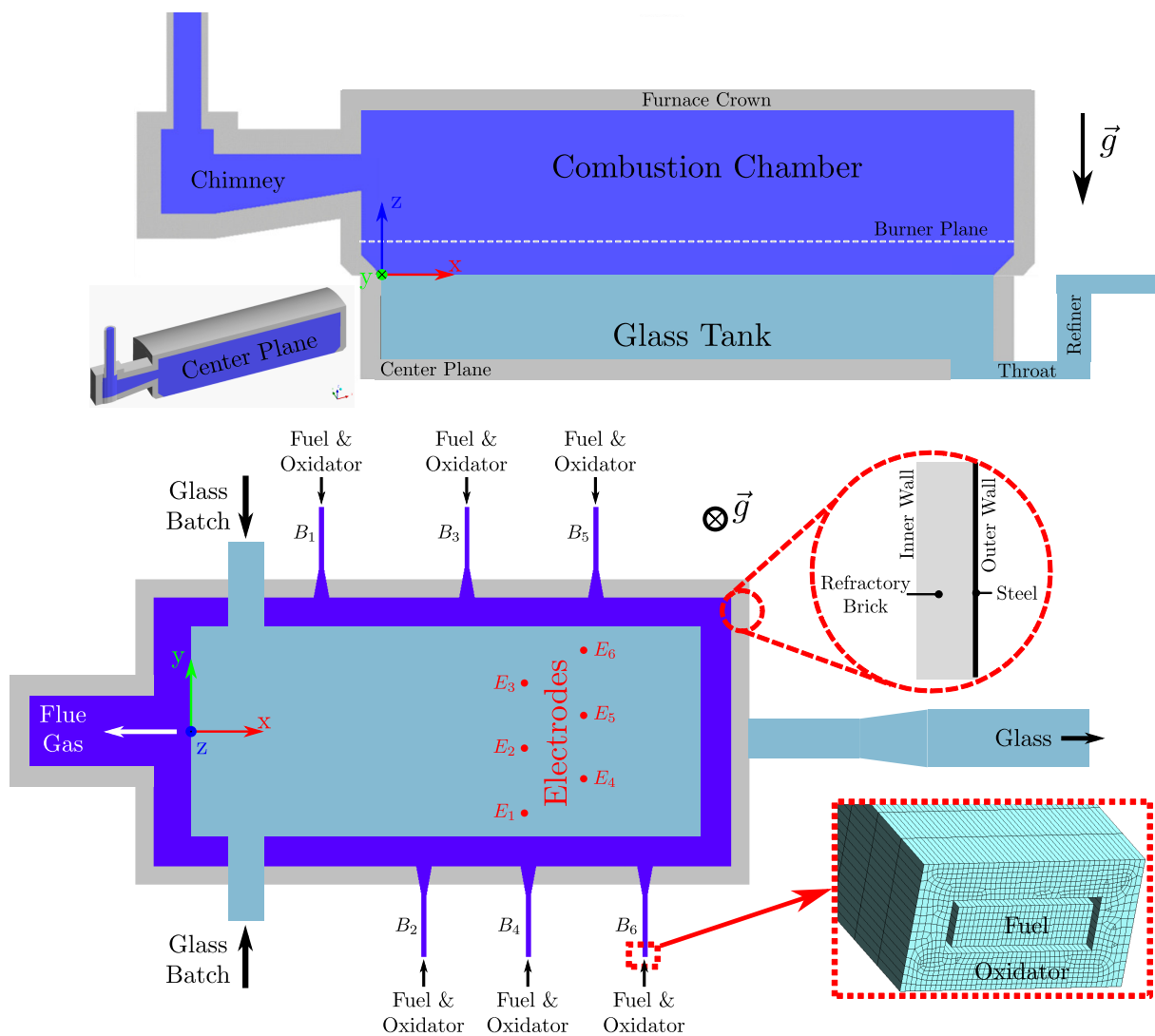
Figure 4.1: Schematic depiction of a cross-fired glass melting furnace.

In general the burners are operated with natural gas and preheated air. A crosswise arrangement of the burners is useful for an optimal temperature distribution. This prevents excessive temperature peaks from occurring on the glass surface. A view of the burner positions and the flame pattern inside the furnace is given in Figure 4.2. The hot flue gases from the combustion process leave the furnace through a chimney.

In the melting furnace temperatures of over 1000 °C are permanently present. Therefore the walls of the combustion chamber and the glass tank are made of refractory materials, which are surrounded on the outside by a steel shell. These materials are used in many high temperature processes. They are characterized by a low thermal conductivity, low thermal expansion and high resistance to high temperatures, thermal shocks, mechanical wear and corrosion.

For a better homogenization of the glass melt, various methods are used to influence the flow in the glass tank. In the present application, this was achieved by employing electric boosting. Six electrically heated electrodes are installed at the bottom of the tank and additionally heat the glass in this area. The resulting lifting forces ensure improved mixing of the liquid glass.

In the scope of this work, a glass melting furnace for the production of glass wool was investigated. A selection of the relevent technical data is given in Table 4.1. The key feature of this furnace was the use of pure oxygen instead of air as oxidizer.
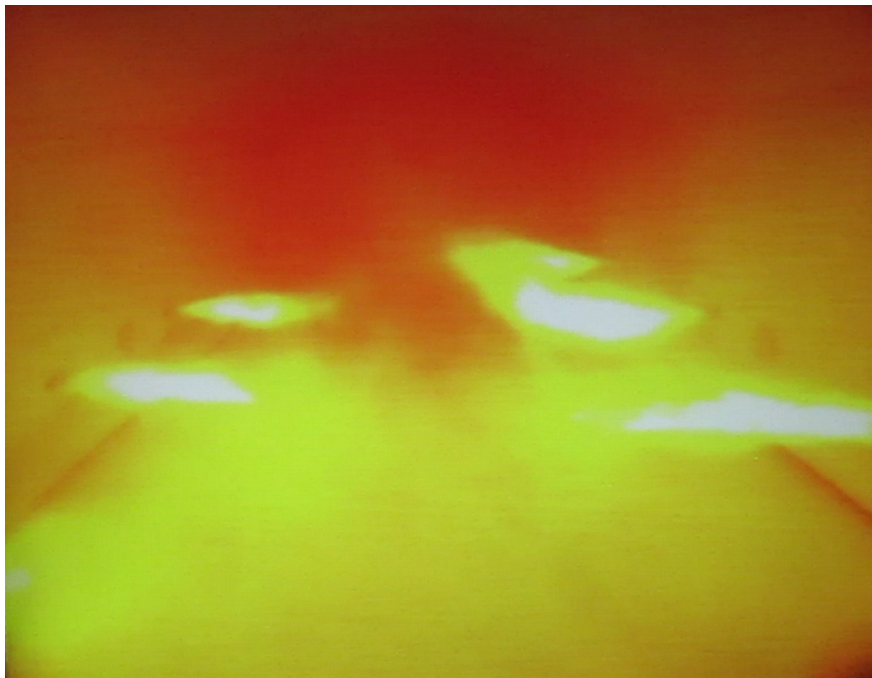

Figure 4.2: View into the combustion chamber of the examined glass melting furnace.

Table 4.1: Technical data of the glass melting furnace.

Production	Unit	Comment
Product		Soda-lime glass
Glass output	t/d	97.5
Cullet content in glass batch	wt%	77.4
Glass output temperature	°C	1130 - 1160
Furnace	**Unit**	**Comment**
Furnace type		Cross-fired oxy-fuel
Dimensions of melting area	m x m	8.8 x 3.8
Glass depth	m	1.2
Type of boosting		Electrical barrier
Number of electrodes	pcs.	6
Additional energy through boosting	kW	600
Specific energy consumption	kWh/kg melted glass	1
Burners	**Unit**	**Comment**
Number of burners	pcs.	6
Type of burner		Eclipse PrimeFire 300
Capacity of the burner	kW	293 - 1172
Fuel type		Natural gas
Fuel flow	Nm³/h	325
Oxidizer		Oxygen (O_2)
Residual oxygen in flue gas (dry)	vol%	3

Advantages of oxy-fuel furnaces are lower specific nitrogen oxides (NO_x) emissions (kg NO_x/ton molten glass) due to the absence of nitrogen (N_2) in the oxidizer and subsequently significantly reduced flue gas volumes. Furthermore, the furnace designs are cheaper because costly heat recovery systems for preheating O_2 are hardly utilized. Oxy-fuel firing also leads to a reduction in fuel consumption that may exceed the costs for oxygen supply.

4.1 Physical Properties of Glass

In the following chapter some essential information about glass and its characteristic behavior will be provided. It seems that glass is in a solid state at room temperature but in a liquid state at the temperatures inside the glass melting furnace. However, a closer look shows that glass is rather described as a supercooled liquid than a solid. In science the term "glass" is used more as a physical state of materials. According to Shelby, glass can be defined as an amorphous solid completely lacking in long range, periodic atomic structure, and exhibiting a region of glass transformation behavior. Any material, inorganic, organic, or metallic, formed by any technique which exhibits glass transformation behavior is a glass [24].

The meaning of the mentioned glass transformation behavior becomes clear with a look at Figure 4.3, where the enthalpy is plotted over temperature. In a crystalline material, cooling the melt to any temperature below the melting temperature T_m would lead to the transformation into the criystalline state with the formation of a long-range, periodic, atomic structure. Thereby the enthalpy decreases abruptly to the corresponding value for the crystal. Further cooling leads to a further decrease in enthalpy according to the heat capacity of the crystal.
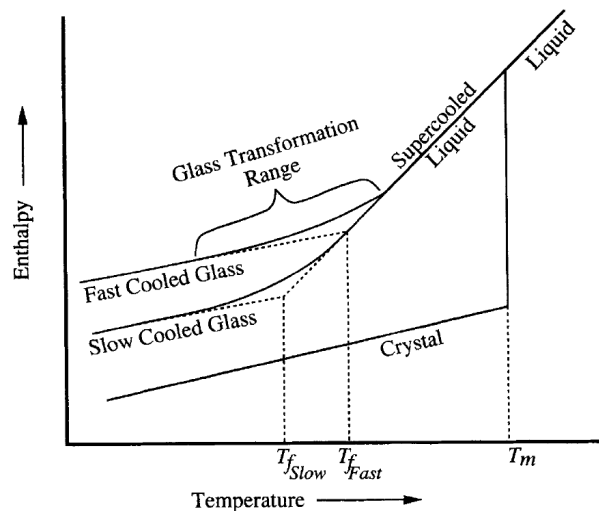
Figure 4.3: Effect of temperature on the enthalpy of a glass forming melt [24].

In contrast, the transformation of a melt to the vitreous state takes place, if the melt can be cooled below T_m without crystallization. In this case a supercooled liquid is formed. As the cooling of the liquid is more advanced, the viscosity increases. This viscosity increase finally becomes so large that the atoms can no longer completely rearrange to the equilibrium structure of the liquid within a sufficient time. This leads to a deviation of the enthalpy from the equilibrium line with a curve of steadily decreasing gradients and ends with a gradient corresponding to the heat capacity of the frozen liquid. That means, that the viscosity of the liquid becomes so high that the structure of the liquid is fixed and no longer temperature-dependent. The frozen liquid is called glass. The temperature range between the beginning and the end of the curve is called the glass transformation region.

If the liquid is cooled down at a lower cooling rate, the enthalpy will follow the equilibrium line longer and glass will be gradually formed at lower temperatures. The resulting glass will have a lower enthalpy than one with a higher cooling rate. The atomic structure will change as well to the characteristic structure of the liquid at a lower temperature. Due to this fact, it is useful to define a parameter that allows to draw conculsions about the thermal history of the obtained glass. For this purpose, the fictive temperature T_f is determined by extrapolationg the equilibrium line representing the supercooled liquid and the line of the frozen liquid.

In Summary, the most important aspect for this work is that – in contrast to common expectations – no heat of fusion has to be applied when reheating the glass for melting. Thus, a continuous enthalpy increase takes place without sudden increases.

4.2 Batch Melting and Fining Process

To better understand the design requirements for the glass melting furnace, the processes taking place inside the furnace have to be explained first. The conversion from a glass batch to a homogeneous glass melt is divided into different steps as shown in Figure 4.4. The flow profile in glass tanks divides the reaction space into relatively well separated subspaces. The aim is to form a double vortex. The hot spot is the area of maximum temperature in the melt. The individual processes assigned to the flow pattern are described below [11, 24, 26].
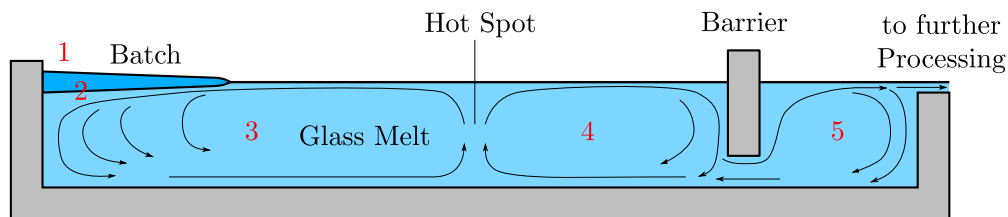
Figure 4.4: Schematic process steps with flow field in a glass tank.

1. **Batch Charging**
   The glass batch is transported in the tank in a charging stem, the so-called doghouse. This happens either at the front over the entire width of the tank or from the side at several points, as shown in Figure 4.1. The glass batch is inserted either in the form of heaps, a strand or a wide carpet and floats on the surface of the molten glass [26].

2. **Batch Melting**
   The glass batch is melted equally at the top and bottom side. Heating of the batch results in the release of gases. Beside water vapor and several other gases also carbon dioxide (CO_2) is released due to the decomposition of carbonates. This process is called calcination. The release of these gases promotes mixing and stirring action in the tank. However, calcination gases result in the formation of bubbles, which have to be removed from the melt before leaving the tank. The raw melt has a temperature of about 1200 °C. Batch melting is the most energy consuming process step with an energy demand of 80-90 % of the total energy demand for the melting and fining process.

3. **Quartz Dissolution**
   The raw melt still contains a substantial amount of solid impurities and grains of quartz (silica). The chemical reactions to dissolve these particles require higher temperatures of up to 1400 °C and a certain amount of convection for mixing in the tank. During these reactions a considerable amount of bubbles is generated in the melt.

4. **Fining**
   After quartz dissolution the melt contains a great number of small and tiny bubbles filled with gases such as CO_2, O_2 and N_2. The extremely time-consuming process of expelling these bubbles is called fining. Only larger bubbles are able to leave the melt on the surface by lifting forces. This happens in the region of the hot spot, where the temperature reaches up to 1500 °C. A chemical reaction is therefore used to create a swarm of relatively large bubbles, which absorbs the small bubbles. As already mentioned, the lift can be increased

by additional measures. Electric boosting causes the heated melt to rise to the surface due to lower density. Another option is the injection of gas bubbles at the bottom of the tank. This method is called bubbling and achieves very good results.

5. **Refining**
   Before leaving the tank for further processing, the melt has to be refined and homogenized. Consequently, the melt is conditioned to temperatures of 1050-1250 °C and stilled. During conditioning the remaining bubbles are dissolved again in the melt. With the exception of tanks used in the float glass industry, region 5 in Figure 4.4, the so-called working tank or refiner is thermally and fluidically separated by a small opening, the throat [11].

In summary, the batch melting and fining process is complex, still subject of research and very dependent on the glass composition. An idea of the challenge to obtain a homogeneous, bubble-free glass melt is given by the fact, that the average residence time of the inserted materials in the batch melting region is only about 40-60 min. However, the average residence time until leaving the tank is significantly higher with about 16-24 h. So, the time consuming processes are the fining and homogenization of the glass melt [11].

5 CFD-Simulation of the Glass Melting Furnace

The numerical simulation of an entire glass melting furnace including the burners, combustion space, chimney, doghouse, glass tank and glass outlet is a challenging problem. In the scope of this work, the software package Ansys Fluent 19.0 was used to perform a range of tasks starting with the generation of the geometry and ending with post-processing of the simulation results.

First, one of the main challenges was the fact, that there are three different phases in the glass melting furnace:

1. The turbulent gas phase in the combustion chamber
2. The solid raw materials in the glass batch
3. The laminar liquid phase of the glass melt

For this reason, the glass melting furnace was split into two autonomous CFD submodels. To receive simulation results for the whole system subsequently, these two submodels were coupled on the glass surface. At this interface the submodels interacted with each other to depict the heat transfer between the gas phase in the combustion chamber and the glass in the tank.

It was decided to investigate the problem in 2D first, since this procedure reduces the time demand for simulation results. Additionally, wrong approaches on the way to a verified model can be detected earlier. This finally reduces the time for the development of a suitable simulation model significantly.

The glass melting furnace under investigation is fired by an oxy-fuel combustion process. Hereby, pure oxygen is used as oxidizer and natural gas as fuel. The combustion chamber is fired by six PrimeFire 300 burners with a total thermal input of 3.35 MW. The fuel, oxidizer and glass batch are supplied at ambient temperature. The glass tank provides a melting area of 33.44 m². It additionally offers the possibility of electric boosting. Therefore, the tank is equipped with 6 electric heating rods with a total electric input of 600 kW, which ensure a better mixing of the melt. Via two opposite inlets 97.5 t/d of batch raw materials with a cullet content of $\mu_C = 77.4\%$ are fed into the glass tank, from which approximately 93.8 t/d of soda-lime glass is produced. According to the manufacturer, the refractory material with a thickness of 0.3 m has a thermal conductivity of approximately 0.5 W/(mK) in the combustion chamber and glass tank. However, it is assumed that due to high thermal stresses and cracks in the refractory material, the thermal conductivity has increased over the decades to 1.5 W/(mK) in the combustion chamber and 3.0 W/(mK) in the glass tank.

5.1 Mass and Energy Balances

In order to estimate the influence variables and to define boundary conditions for the CFD-simulation, a mass and energy balance of the system had to be drawn up at first. As fuel in all further considerations instead of natural gas its main component methane (CH_4) was used.

At the combustion chamber, the incoming mass flows are determined by the sum of the mass flows of fuel $\dot{m}_{CH_4}$ and oxidizer $\dot{m}_{O_2}$ as well as an additional mass flow of carbon dioxide (CO_2) $(1 - \mu_C)\dot{m}_{CO_2}$. The latter is released in the glass tank due to chemical calcination reactions during glass batch melting from the raw materials dolomite, lime and soda and will be discussed in more detail later. It must be taken into account that the melting of the added cullet does not produce reaction gases. The outgoing mass flows are only determined by the mass flow of the flue gas $\dot{m}_{FG}$, which leaves the combustion chamber through the chimney. The incoming and outgoing mass flows at the combustion chamber are quantified in Equations (5.1) and (5.2).

$$\dot{m}_{CC,in} = \dot{m}_{CH_4} + \dot{m}_{O_2} + (1 - \mu_C)\dot{m}_{CO_2} = 5.8 + 23.3 + 3.7 = \mathbf{32.8\,t/d} \tag{5.1}$$

$$\dot{m}_{CC,out} = \dot{m}_{FG} = \mathbf{32.8\,t/d} \tag{5.2}$$

In the glass tank the solid glass batch of the mass flow $\dot{m}_{glass,in}$ is supplied, while the liquid glass melt and the calcination gases are discharged with the fluxes $\dot{m}_{glass,out}$ and $(1 - \mu_C)\dot{m}_{CO_2}$. The incoming and outgoing mass flows are balanced in Equations (5.3) and (5.4).

$$\dot{m}_{GT,in} = \dot{m}_{glass,in} = \mathbf{97.5\,t/d} \tag{5.3}$$

$$\dot{m}_{GT,out} = \dot{m}_{glass,out} + (1 - \mu_C)\dot{m}_{CO_2} = \mathbf{97.5\,t/d} \tag{5.4}$$

The energy balances of the combustion chamber and the glass tank are shown in Figure 5.1 and 5.2. The heat fluxes transferred between the two submodels combustion chamber and glass tank are coloured in orange. Supplied electric power is coloured in red. All other incoming and outgoing heat fluxes at both submodels are coloured in black.

At the burners in the combustion chamber, the fuel and the oxygen are supplied at ambient temperature T_1 with the heat fluxes $\dot{Q}_{CH_4}$ and $\dot{Q}_{O_2}$. In Figure 4.1 the arrangement of the fuel inlet in the center and the oxygen inlet in the outer ring is sketched. With the fuel the heat of combustion is additionally supplied, which is denoted $\dot{Q}_{u,CH_4}$ and determined in Equation (5.5). In the energy balance the heat fluxes of all six burners are summarized as total heat of combustion for one single burner.

$$\dot{Q}_{u,CH_4} = \dot{m}_{CH_4} \cdot \frac{\Delta H_M(T^0)}{M_{CH_4}} = \dot{m}_{CH_4} \cdot H_{u,CH_4} = \mathbf{3.350\,MW} \tag{5.5}$$

The energy released due to the oxy-fuel combustion inside the combustion chamber is used to heat and melt the glass in the tank. This is considered in the heat flux $\dot{Q}_{melt}$, which is transferred over

the glass surface. The flue gas leaving the combustion chamber via the chimney is represented by the heat flux $\dot{Q}_{FG}$. Additionally, the wall losses of the combustion chamber are considered as $\dot{Q}_{CC,W}$. Due to melting reactions in the glass batch, a certain amount of CO_2 is released at the glass surface. This CO_2 supplied to the combustion chamber is considered in the energy balance by the heat flux $\dot{Q}_{CO_2}$.
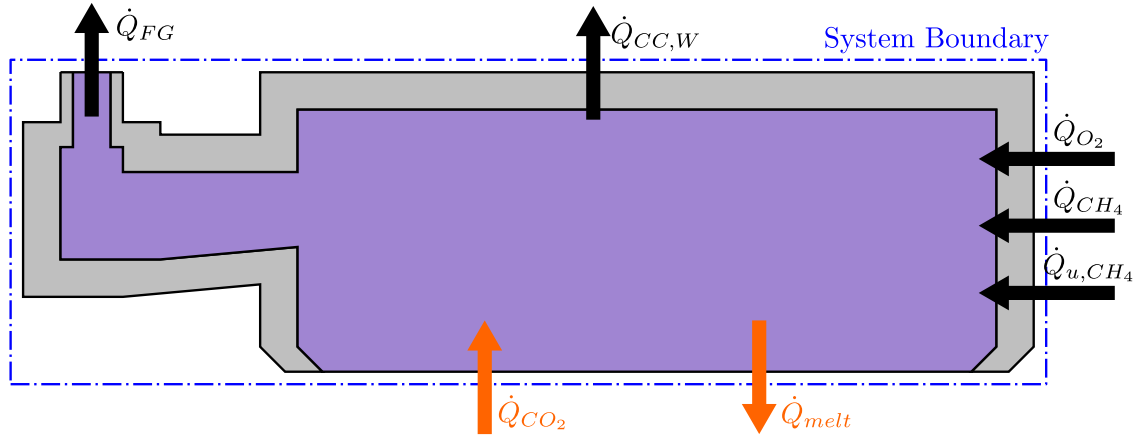

Figure 5.1: Energy balance of the combustion chamber.

The overall supplied energy and the individual heat fluxes are given in Equations (5.6) - (5.9).

$$\dot{Q}_{CC,in} = \dot{Q}_{CH_4} + \dot{Q}_{O_2} + \dot{Q}_{u,CH_4} + \dot{Q}_{CO_2} = \mathbf{3.409\,MW} \tag{5.6}$$

$$\dot{Q}_{CH_4} = \dot{m}_{CH_4} \cdot \frac{C_{mp,CH_4}\big|_{T_1}}{M_{CH_4}} \cdot \left(T_1 - T^0\right) = \mathbf{3.6\,kW} \tag{5.7}$$

$$\dot{Q}_{O_2} = \dot{m}_{O_2} \cdot \frac{C_{mp,O_2}\big|_{T_1}}{M_{O_2}} \cdot \left(T_1 - T^0\right) = \mathbf{6.1\,kW} \tag{5.8}$$

$$\dot{Q}_{CO_2} = \left(1 - \mu_C\right)\dot{m}_{CO_2} \cdot \frac{C_{mp,CO_2}\big|_{T_2}}{M_{CO_2}} \cdot \left(T_2 - T^0\right) = \mathbf{48.6\,kW} \tag{5.9}$$

To fulfill the energy balance, the outgoing heat fluxes have to be equal to the incoming heat fluxes. The overall heat losses and the individual heat fluxes are written in Equations (5.10) - (5.13).

$$\dot{Q}_{CC,out} = \dot{Q}_{CC,in} = \dot{Q}_{FG} + \dot{Q}_{CC,W} + \dot{Q}_{melt} = \mathbf{3.409\,MW} \tag{5.10}$$

$$\dot{Q}_{FG} = \dot{m}_{FG} \cdot \frac{C_{mp,FG}\big|_{T_3}}{M_{FG}} \cdot \left(T_3 - T^0\right) = \mathbf{1.102\,MW} \tag{5.11}$$

$$\dot{Q}_{CC,W} = k_{CC,W}\frac{A}{s} \cdot \left(T_{CC,W,int} - T_{CC,W,ext}\right) = \mathbf{0.711\,MW} \tag{5.12}$$

$$\dot{Q}_{melt} = \dot{Q}_{CC,out} - \dot{Q}_{FG} - \dot{Q}_{CC,W} = \mathbf{1.596\,MW} \qquad (5.13)$$

The temperatures used to establish the energy balance of the system are listed in Table 5.1. For the ambient temperature T_1 a reasonable assumption was made. The temperature of the glass melt T_2 and the temperature of the flue gas T_3 were calculated analytically, while the temperatures of the internal and external side of the walls $T_{W,int}$ and $T_{W,ext}$ at the combustion chamber and the glass tank were estimated by using empirical values. As reference value for the calculation of all heat fluxes the standard temperature T^0 was used.

Table 5.1: Relevant temperatures for the energy balance.

Temperature	[K]	[°C]
T^0	273.15	0
T_1	298.15	25
T_2	1274.55	1001,4
T_3	1951.66	1678,51
$T_{CC,W,int}$	2036.68	1763,53
$T_{CC,W,ext}$	518.36	245,21
$T_{GT,W,int}$	1546.46	1273,31
$T_{GT,W,ext}$	434.51	161,36

In the glass tank, the melting heat $\dot{Q}_{melt}$ transferred from the combustion chamber is considered as an input. The energy transfer of the released reaction gas $\dot{Q}_{CO_2}$ during glass batch melting takes place in the opposite direction. Thus it is treated as an outout at the glass tank. With the glass batch the heat flux $\dot{Q}_{glass,in}$ is supplied to the tank at the beginning of the process. At the end of the process the glass melt leaves the combustion chamber with the heat flux $\dot{Q}_{glass,out}$. Additionally, the electric power P is supplied to the tank for electric boosting. The wall losses of the tank are considered in $\dot{Q}_{GT,W}$. Furthermore, the chemical reactions during glass batch melting require a certain amount of energy. This is considered in form of an outgoing heat flux $\dot{Q}_{u,glass}$.
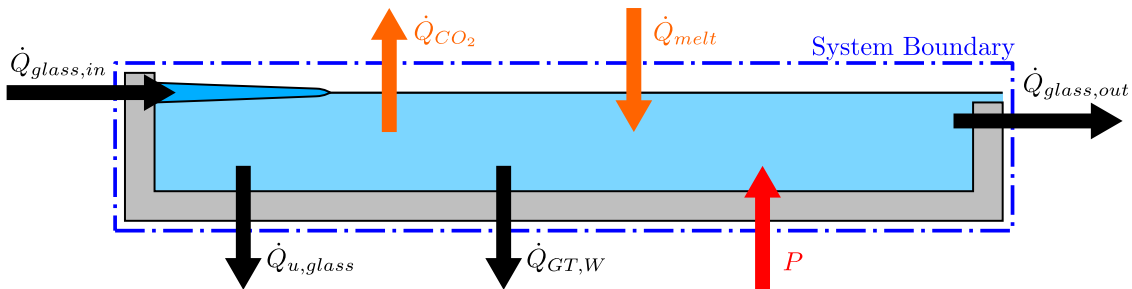
Figure 5.2: Energy balance of the tank.

The overall energy supplied to the glass tank and the heat flux due to the glass batch input, depending on its composition, are formulated in Equations (5.14) and (5.15).

$$\dot{Q}_{GT,in} = \dot{Q}_{glass,in} + P + \dot{Q}_{melt} = \mathbf{2.220\,MW} \qquad (5.14)$$

$$\dot{Q}_{glass,in} = \sum_i \dot{n}_i \cdot C_{mp,i} \cdot \left(T_1 - T^0\right) = \mathbf{24.5\,kW} \tag{5.15}$$

The overall energy output of the glass tank and the individual heat fluxes are summarized in Equations (5.16) - (5.18).

$$\dot{Q}_{GT,out} = \dot{Q}_{glass,out} + \dot{Q}_{u,glass} + \dot{Q}_{CO_2} + \dot{Q}_{GT,W} = \mathbf{2.220\,MW} \tag{5.16}$$

$$\dot{Q}_{GT,W} = k_{GT,W}\frac{A}{s} \cdot \left(T_{GT,W,int} - T_{GT,W,ext}\right) = \mathbf{773\,kW} \tag{5.17}$$

$$\dot{Q}_{u,glass} = \left(1 - \mu_C\right)\dot{m}_{glass,in} \cdot \Delta H^0_{chem} = \mathbf{132.3\,kW} \tag{5.18}$$

5.1.1 Reaction Chemistry and Melting Process

In the following subsection, the theoretical background for the calculation of the mass flow rate and the heat flux of the released CO_2 is presented.

First, the amount of released CO_2 was determined. Glass batches in general contain significant amounts of carbonates. During the melting process, these carbonates decompose and CO_2 is released into the combustion chamber atmosphere. The exact composition of the recycled cullet and the newly melted raw materials in the glass melting furnace was not known. For this reason, a simple model composition for soda-lime glass was used according to the approach by Conradt [10]. The model composition is given in Table 5.2. In the left column the raw material composition of the inserted glass batch is listed. The composition of the oxides formed during batch melting in the glass tank is listed in the middle column. And finally the composition of the resulting phases with their respecitve chemical formula in the glass melt is listed in the right column. All values in Table 5.2 refer to one ton of melted glass.

Table 5.2: Model for the glass composition in terms of raw materials, oxides and phases [10].

Raw material i	[kg/t]	Oxide j	[kg/t]	Phase k	[kg/t]
Sand	666.96	SiO_2	720.00	SiO_2	227.05
Feldspar	77.15	Al_2O_3	15.00	$Na_2O{\cdot}Al_2O_3{\cdot}6SiO_2$	77.15
Dolomite	182.98	MgO	40.00	$MgO{\cdot}SiO_2$	99.62
Limestone	34.54	CaO	75.00	$Na_2O{\cdot}3CaO{\cdot}6SiO_2$	263.34
Soda ash	240.91	Na_2O	150.00	$Na_2O{\cdot}2SiO_2$	332.84
		CO_2	202.54		
Σ	1202.54		1202.54		1000.00

In the glass batch composition from the chosen model, the amount of CO_2 released is 202.54 kg/t of melted glass. In Equation (5.19) the mass fraction w_{CO_2} of formed CO_2 is determined by the fraction of CO_2 to the sum of all formed oxide species.

$$w_{CO_2} = \frac{m_{CO_2}}{m_{tot}} = \frac{202.54\,\text{kg/t}}{1202.54\,\text{kg/t}} = \textbf{0.1684} \tag{5.19}$$

Subsequently, the amount of formed CO_2 during melting is calculated according to Equation (5.20) by multiplying the CO_2 mass fraction and the amount of incoming glass batch. Due to the share of cullet in the glass batch the amount of released CO_2 reduces to $(\mathbf{1} - \boldsymbol{\mu_C})\dot{\mathbf{m}}_{\mathbf{CO_2}}$. This results in a value of **0.043 kg/s** released CO_2, in other terms 3.7 t/d.

$$\dot{m}_{CO_2} = w_{CO_2} \cdot \dot{m}_{glass,in} = 0.1684 \cdot 1.1285\,\text{kg/s} = 0.19007\,\text{kg/s} \tag{5.20}$$

Second, the heat flux due to the released CO_2 was determined. The calculation was conducted according to Equation (5.9) and yields:

$$\dot{Q}_{CO_2} = \left(1 - 0.7741\right) \cdot 0.19007\,\text{kg/s} \cdot \frac{49.70\,\text{J/(mol K)}}{0.044\,\text{kg/mol}} \cdot \left(1274.55\,\text{K} - 273.15\,\text{K}\right) = \textbf{48.6 kW} \tag{5.21}$$

Finally, the chemical reaction heat $\dot{Q}_{u,glass}$ was calculated. Conradt determined for the standard enthalpy of reaction a value of ΔH^0_{chem} = 144.2 kWh per ton of melted glass for the chosen model batch [10]. Thus, Equation (5.18) results in:

$$\dot{Q}_{u,glass} = \left(1 - 0.7741\right) \cdot 1.1285\,\text{kg/s} \cdot 144.2\,\text{kWh/t} = \textbf{132.3 kW} \tag{5.22}$$

As shown in Equation (5.18), an increasing cullet percentage at the glass batch results in a monotonous reduction of the required chemichal reaction heat. This correlation is visualized in Figure 5.3. For example, a reaction heat of 585.8 kW would be required to operate the glass melting furnace without cullets. In contrast, when using pure cullet for the glass batch, the required heat of reaction is equal to zero. In the glass industry this aspect is used to steadily maximize the percentage of cullet in the batch composition.
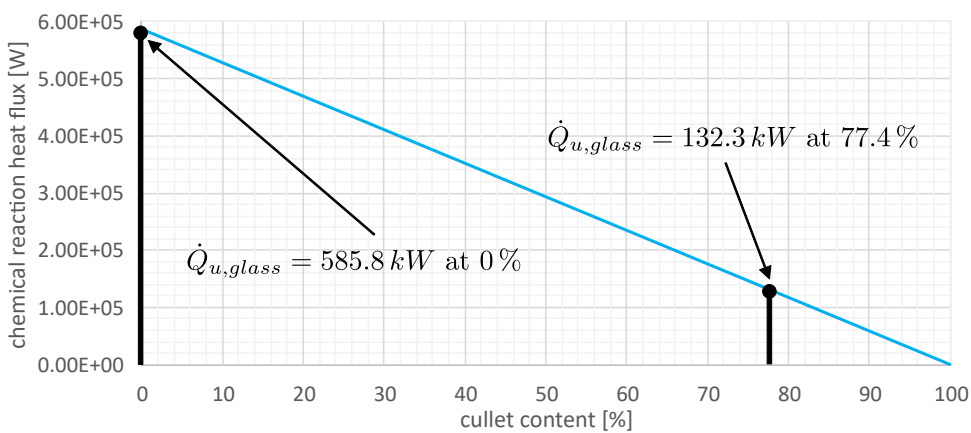
Figure 5.3: Chemical reaction heat in dependence of the cullet content.

It is worth noting, that besides CO_2 also other gases like water vapor (H_2O), sulfur oxides, oxygen, etc., are released during glass batch melting. However, for the soda-lime glass under investigation

in the present application the released H_2O was negligible. Depending on the moisture content of the glass batch, a significant amount of vapor can also be released in the glass melting furnace. A consideration of this species in addition to CO_2 is also reasonable because of the participation at radiative heat transfer in the gas space of the combustion chamber.

In the following step, two different approaches for considering the chemical reaction heat in the CFD simulation are presented:

1. As a source term, which is uniformly distributed over the entire glass volume. It results from dividing the chemical reaction heat $\dot{Q}_{u,glass}$ by the volume of the glass melt to approximately -3.3 kW/m³.
2. In the specific heat capacity of the glass $c_{p,glass,new}$, which was derived from Equation (5.24):

$$\underbrace{\dot{Q}_{glass,out} + \dot{Q}_{u,glass}}_{} + \dot{Q}_{CO_2} + \dot{Q}_{GT,W} = \dot{Q}_{glass,in} + P + \dot{Q}_{melt} \tag{5.23}$$

$$\dot{m}_{glass,out} \cdot c_{p,glass} \cdot \left(T_2 - T^0\right) + \dot{Q}_{u,glass} = \dot{m}_{glass,out} \cdot c_{p,glass,new} \cdot \left(T_2 - T^0\right) \tag{5.24}$$

For solution path 2 it was assumed that most of the CO_2 is released in the temperature range between 700 °C and 1000 °C. Thus, the new specific heat capacity curve, shown in Figure 5.4 was obtained.
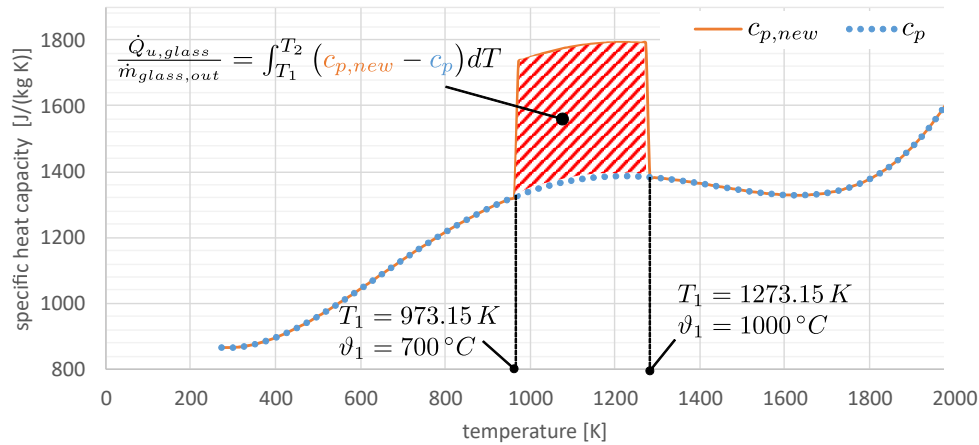
Figure 5.4: Development of the specific heat capacity of the glass.

As already described, the batch gases were taken into account in the CFD simulation as well. The focus in the present CFD simulation was on CO_2. For this purpose, a new method was developed in which the released amount of CO_2 was first analytically calculated. The released CO_2 was subtracted from the mass flow of the incoming glass batch and subsequently added to the oxidizer mass flow in the combustion chamber. Thus, the mass balance of the entire system was respected. In this way possible chemical reactions in the combustion chamber could be simulated, which only take place after the CO_2 batch gas comes into contact with the other combustion gases.

5.2 Grid Independence Study

Besides a good mesh quality, the resolution of the mesh should also be selected appropriately. A too fine grid only unnecessarily increases the computing time and memory requirements. A too coarse grid does not reflect reality sufficiently. For this reason, already before all further investigations a grid independence study was carried out for each task. In order to find a computational cheap but still independent mesh grid, the grid is normally refined several times according to certain criteria, for example, the temperature gradient of neighboring cells. Only when the solution does not change with the refinement of the mesh, grid independency can be assumed. In this work the inverse approach of mesh coarsening was chosen for the 2D simulations in order to get a stable and convergent solution at the beginning. This approach was well suited because of the rather small mesh sizes in 2D.

At the glass tank four different mesh versions were created with the mesh grid parameters given in Table 5.3. Especially at the glass tank it was mandatory to resolve the entire domain with a fine mesh at the beginning to identify zones with high gradients for temperature, velocity and material properties. In further consequence, regions with low gradients were meshed more and more coarsely for generation of the remaining three mesh versions. As a simulation result with high information content the outlet temperature was used for the evaluation of the mesh grid independence. Therefore, for all mesh grid versions absolute and relative deviations to the outlet temperature of the fine mesh grid V6 were calculated.

Table 5.3: Mesh grid parameters at the glass tank.

Grid version	V6	V11	V16	V18
Number of cells [–]	448417	319705	199039	147515
Outlet temperature [K]	1387.0	1385.2	1383.5	1358.1

The absolute and relative deviations of the outlet temperature over the number of cells are shown in Figure 5.5.
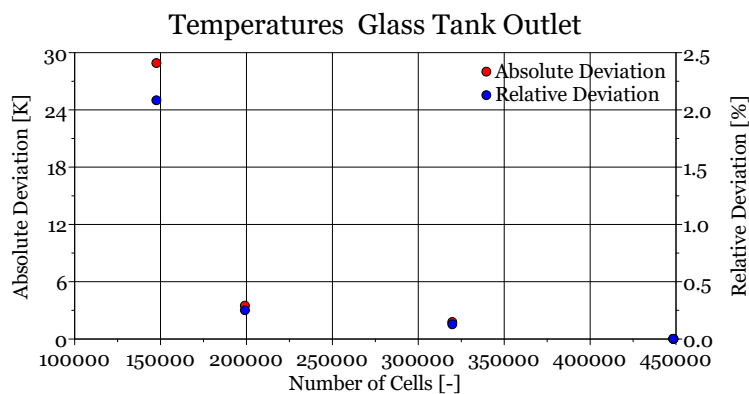
Figure 5.5: Temperature deviations at the glass outlet of different mesh grids.

In comparison to the reference mesh V6 with almost 450000 cells and an outlet temperature of 1387.0 K, the temperature deviation of the mesh grids V11 and V16 increased almost linear to a number of slightly less than 200000 cells at V16 and an absolute deviation of 3.5 K, which is a

relative value of 0.25 %. With further reduction to about 147500 cells, the temperature deviation increased strongly to a value of 28.9 K, which is a relative deviation of 2.08 %.

At the combustion chamber four different mesh versions were created as well with the mesh grid parameters given in Table 5.4. The entire domain was resolved with a fine mesh at the beginning to identify zones with high gradients for temperature, velocity and species fraction. In further consequence, regions with low gradients were meshed more and more coarsely for generation of the remaining three mesh versions. In analogy to the glass tank, the outlet temperature was used as a simulation result with high information content for the evaluation of the mesh grid independence. Therefore, at all mesh grid versions absolute and relative deviations to the outlet temperature of the fine mesh grid V6 were calculated.

Table 5.4: Mesh grid parameters at the combustion chamber.

Grid version	V6	V8	V12	V13
Number of cells [–]	297096	202999	96311	56228
Outlet temperature [K]	1691.6	1693.1	1703.5	1711.7

Compared to the reference mesh V6 with almost 300000 cells and an outlet temperature of 1691.6 K, the temperature deviations of the mesh grids V8, V12 and V13 indicated an exponential increase with decreasing number of cells. At mesh grid V13, with approximately 56000 cells for instance, the temperature deviation had a value of 20.1 K, which is a relative deviation of 1.19 %. The absolute and relative deviations of the outlet temperature over the number of cells for the different mesh grid versions are shown in Figure 5.6.
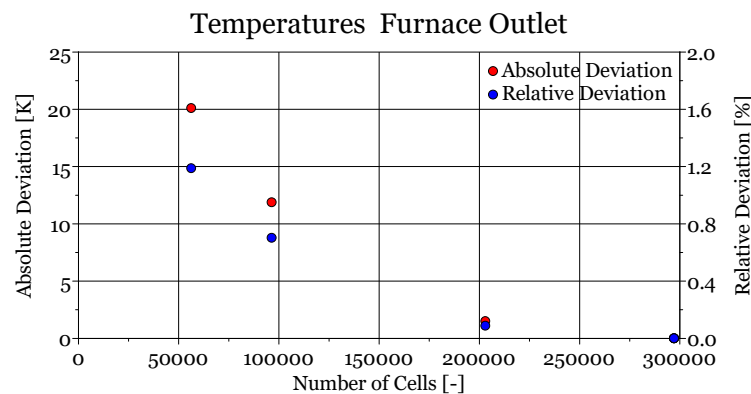
Figure 5.6: Temperature deviations at the flue gas outlet of different mesh grids.

As criterion for the evaluation of the mesh grid deviations and subsequent mesh grid selection at combustion chamber and glass tank, a maximum relative deviation of 1 % was defined. Based on the gained knowledge, all further combustion chamber simulations were performed with combustion chamber mesh grid V12 and all further glass tank simulations with glass tank mesh grid V11.

5.3 Simulation of the Combustion Chamber

First, the simulation of the combustion chamber is treated in this work. In this part of the system primarily an oxy-fuel combustion with the admixture of CO_2 released from the melting glass takes place. The six burners of the glass melting furnace are individually supplied with CH_4 and oxygen. They are operated with a fixed equivalence ratio corresponting to 3 vol% O_2 in the dry flue gas. The hot flue gas heats the glass below and is then discharged via the chimney. The position of the hot spot on the glass surface is adjusted with the individual fuel flows in each burner.

5.3.1 Geometry and Mesh

The geometry of the combustion chamber was generated with the DesignModeler in Ansys Workbench 19.0 based on a design drawing, which was provided by the project partner. In order to convert this drawing into a 2D geometry, various simplifications had to be made. The real circumstances were still represented as good as possible. The more the geometry can be simplified, the more efficient the subsequent simulation process will be. For this purpose, the six burners were reduced to one single burner, which was located on the right side of the combustion chamber without any modifications in mounting hight. Both, the inlet length at the burner and the outlet length at the chimney were stretched to avoid negative effects due to flow deflections. The entire chimney was not resolved in the 2D simulation in order to achieve the lowest possible number of elements during meshing with the aim of optimizing the computation time. The combustion chamber walls made of refractory material were not resolved in the geometry. With regard to subsequent meshing, the geometry was already split up into a number of suitable small sections in the DesignModeler.

The meshed geometry of the combustion chamber is depicted in Figure 5.7. The mesh grid was generated with Meshing in Ansys Workbench 19.0. Different sections in the geometry were defined in a way that it was feasible to apply a structured mesh with Quads to large parts of the whole geometry.
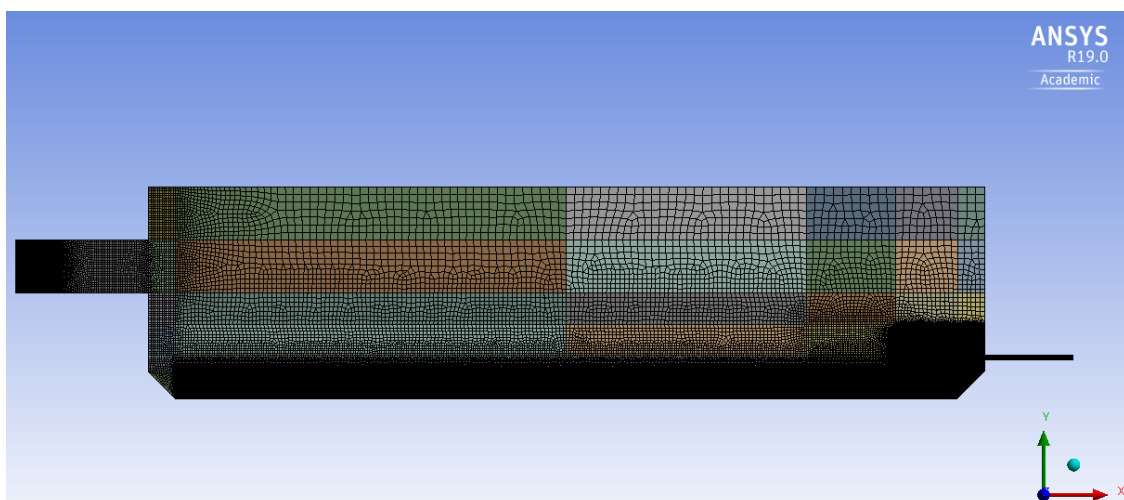

Figure 5.7: Mesh grid of the combustion chamber.

Special attention was paid to very fine meshing of areas with potentially high gradients for temperature, flow variables and species concentration. This was the case in the region of the fuel and oxygen inlets, the reaction zone of the oxy-fuel combustion and the region above the glass surface. A fine mesh was also generated at the flue gas outlet in the chimney in order to prevent backflows. A rather coarse mesh was applied to uncritical regions where gradients were smaller. The maximum element size was defined with a value of 7.5 cm. The sections between regions with different mesh sizes were meshed, so that the compensation between the different element sizes was done with Tris.

In order to check the quality of the created mesh, the corresponding mesh parameters were reviewed and summarized in Table 5.5. A moderate number of cells was found for the rather high number of individual faces. Thus, it was also expected that the computation effort would not be too high. The values for skewness, aspect ratio and orthogonal quality are within the usual range for two-dimensional CFD simulations.

Table 5.5: Mesh grid parameters of the combustion chamber.

Parameter	Value
Number of faces	53
Number of cells	96311
Max. skewness (Q_{EAS})	0.83
Mean skewness (Q_{EAS})	0.08
Max. aspect ratio	10.99
Mean aspect ratio	1.21
Min. orthogonal quality	0.29
Mean orthogonal quality	0.97

5.3.2 Models and Input Parameters

To define the present material in the computational domain, appropriate materials were created in Ansys Fluent. In this context a gas mixture was assigned to the entire meshed domain. The heat transfer at the combustion chamber walls was modelled with an additionally created refractory material. The chosen material properties for both materials are shown in Table 5.6.

For the refractory material typical average values for AZS fused zirconia corundum refractory bricks were used [25, 29]. The combustion chamber walls consist of many individual bricks. The spaces between all these bricks have a considerable influence on the thermal conductivity of the wall. Therefore, no characteristic material value was used. The chosen value was provided by the industrial partner. It is based on temperature measurements at the outer wall of the combustion chamber. For the material properties with small changes, constant values were used. In contrast, the density was determined using the PDF. The specific heat was calculated via the mixing law and the absorption coefficient via the domain based weighted-sum-of-gray-gases model (WSGGM).

Table 5.6: Material properties for the combustion chamber model.

	Refractory	Gas mixture
Density $\rho\,[kg/m^3]$	3700	pdf
Specific heat capacity $c_p\,[J/(kgK)]$	1000	mixing law
Thermal conductivity $k_c\,[W/(mK)]$	1.5	0.0454
Viscosity $\mu\,[Pa\,s]$	-	$1.72 \cdot 10^{-5}$
Absorption coefficient $a\,[1/m]$	0	wsggm-domain-based
Scattering coefficient $\sigma_s\,[1/m]$	0	0
Refractive index $n\,[-]$	1	1

Already while the geometry was generated, the boundaries of the computational domain were split into different sections. The sections, shown in Figure 5.8, were highlighted in different colours and additionally labeled from (a) to (g). Thus, particular boundaries were defined for the two oxidizer inlets (a), for the fuel inlet (b) between them and for the flue gas outlet (c) on the opposite side as well. Furthermore, separate boundaries were defined for the entrance areas of the inlets (d), the indirect (e) and direct zone (f) on the glass surface and the combustion chamber walls (g). At the glass surface a distinction between direct and indirect zone, which corresponds to the burner positions, was made to roughly approximate the actual temperature profile. The indirect zone was defined from $0\,m \leq x < 4.4\,m$ and from $7.1\,m \leq x \leq 8.8\,m$. The direct zone from $4.4\,m \leq x < 7.1\,m$.
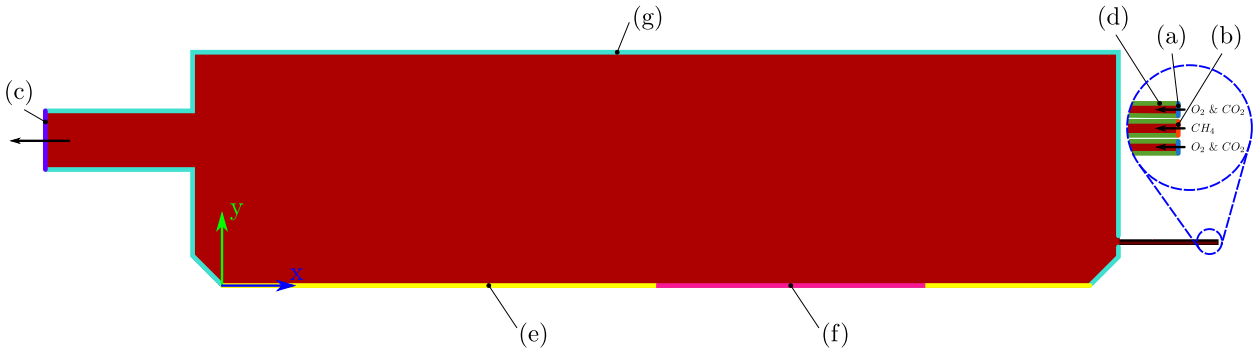
Figure 5.8: Combustion chamber boundary conditions numbered and indicated in different colors.

Detailed parameters of all boundary conditions at the combustion chamber are listed in Table 5.7. The oxidator inlets (a) as well as the fuel inlet (b) were configured as mass flow inlets with a predefined mass flow rate and inflow temperature. The flue gas outlet (c) was defined as pressure outlet. Beside the gauge pressure, the hydraulic diameter and temperature for possible backflows were specified. The latter was defined in accordance with the calculations for the energy balance in Table 5.1. To represent the common situation in chimneys, a slightly negative gauge pressure was chosen. For the mentioned inlets and outlets the turbulent intensity was assumed with 5 %. The entrance areas of the inlets (d) were defined as adiabatic walls. At both boundaries on the glass surface (e) and (f) a predefined temperature was imprinted. For the remaining combustion chamber walls (g) a mixed boundary was configured. With this boundary type convection and radiation is considered on both sides of the wall as well as heat conduction through the wall. For the wall the material refractory was assigned with a certain thickness. With respect to the radiation behavior, all walls were assumed to be opaque. Additionally, all walls were defined as stationary walls with no slip.

Table 5.7: Boundary condition parameters at the combustion chamber.

Location	Parameter	Unit	Value
(a)	Mass flow rate	kg/s	0.262
	Hydraulic diameter	m	0.0253
	Temperature	K	300
(b)	Mass flow rate	kg/s	0.0646
	Hydraulic diameter	m	0.0268
	Temperature	K	300
(c)	Gauge pressure	Pa	-200
	Backflow hydraulic diameter	m	0.6
	Backflow temperature	K	1950
(e)	Temperature	K	1573
	Emissivity	–	0.9
(f)	Temperature	K	1973
	Emissivity	–	0.9
(g)	Heat Transfer coefficient	W/(m²K)	10
	Free stream temperature	K	300
	External emissivity	–	0.8
	External radiation temperature	K	300
	Internal emissivity	–	0.5
	Wall thickness	m	0.3

Gravity was considered in negative y-direction as well. Further models were used in Ansys to treat the activities inside. For turbulence modelling the realizable $k - \varepsilon$ model with standard wall functions for near-wall treatment was used. The use of standard wall functions was feasible with $y^+ \approx 100$ for the chosen mesh. Radiation was considered with the DO model every 10 iteration steps. In this case, the angular discretization was done with 2 divisions and 1 pixel in each direction. Due to lower computational effort, the discretization was just increased to 4 divisions and 3 pixels in each direction, when an almost convergent solution was reached. For modelling the oxy-fuel combustion, the non-adiabatic partially premixed combustion model was used with the steady diffusion flamelet model (SFM). The spatial species composition of the gas mixture in the domain was obtained by the "skeletal25" reaction mechanism. It includes 17 different species and 25 reversible chemical reactions. The composition of the oxidizer was defined with a mole fraction of $\nu_{O_2} = 0.89707$ and $\nu_{CO_2} = 0.10293$ taking into account the required residual oxygen in the flue gas and the CO_2 released due to the glass melting process.

The present set of equations was solved in steady state with the pressure-based segregated solver and the SIMPLE scheme for pressure-velocity coupling. The spatial discretization was performed for the gradients with "Least Squares Cell Based", for the pressure in "Second Order", for radiation in "First Order Upwind" and for all remaining equations in "Second Order Upwind". The applied under-relaxation factors for the pressure-based solver are shown in Table 5.8.

Table 5.8: Under-relaxation factors for the solver at the combustion chamber.

Parameter	Value
Pressure	0.3
Density	0.3
Body forces	0.7
Momentum	0.7
Turbulent kinetic energy	0.8
Turbulent dissipation rate	0.8
Turbulent viscosity	0.6
Energy	0.99
Temperature	0.99
Discrete ordinates	0.98
Progress variable	0.9
Mean mixture fraction	0.999
Mixture fraction variance	0.999

5.3.3 Discussion and Results

In the following, some results of the 2D CFD simulations are presented and the resulting findings and implications for the 3D CFD simulations are discussed. A quantitative comparison was not possible due to the highly simplified geometry in 2D. This was especially due to the reduction to one single burner and the mandatory change of the burner position in 2D from the side combustion chamber walls to the outlet combustion chamber wall. The aim of the CFD simulations in 2D was to optimize the computation time and to confirm the applicability of the different computation models.

For this purpose, Figure 5.9 shows the velocity magnitudes with streamlines and direction vectors at the top and the temperature distribution in the combustion chamber at the bottom. Although the position of the flame did not correspond to reality, several conclusions could be drawn. Approximately 1 m after leaving the burner, the flow field was significantly deflected downwards and separated into two paths. The first one built a vortex in the lower right corner of the combustion chamber. This secondary vortex increased the mixing rate between fuel and oxidizer at the burner inlet for a proper combustion. The second and main path moved along the glass surface with hardly any disturbances to the outlet at the opposite side of the combustion chamber. At the outlet no backflows were recognized. In the region below the furnace crown, moderate secondary flows were detected close to the outlet. They were caused by the deflection of the main stream into the chimney. Above the glass surface the velocity magnitude in the flow field reached maximum values of 7 m/s. At the fuel and oxidizer inlet the velocity magnitudes were below 1 m/s. However, the actual magnitudes at the inlets were within a range of 14-16 m/s. The reason for this significant lower velocity magnitudes in the simulation results was the neglected combustion chamber depth normal to the view plane in Figure 5.9. Indeed, in this plane the combustion chamber had an extension of 3.8 m, but the burner only had an extension of about 15 cm. For 2D problems Ansys assumed a reference value of 1 m for the depth of all geometries in the computation domain.
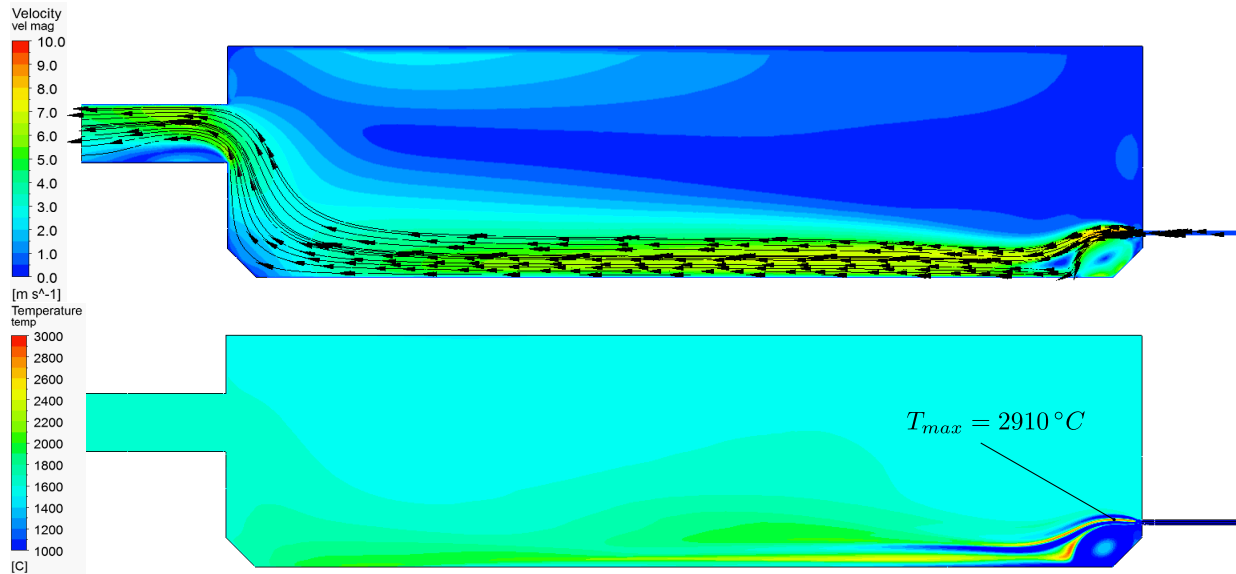
Figure 5.9: Results of the 2D CFD simulation of the combustion chamber. Top: Velocity magnitudes, streamlines and direction vectors. Bottom: Temperature field.

The simulation results for the temperature distribution showed a rather homogenous development with a magnitude of 1500-1700 °C in the whole domain outside the region with direct influence of the combustion. This region of direct influence extended from the burner inlets to the opposite end of the glass surface, similar to that of the flow field. The temperature level in this region was noticeably higher. The highest value of 2910°C was computed inside the flame. This simulation result devidated from reality, because the adiabatic flame temperature of a stoichiometric methane combustion with oxygen is only 2860 °C. On the glass surface close to the burner inlets the temperature was 2600 °C. Up to the end of the glass surface the temperature level decreased towards 2000 °C. In the area of the secondary vortex in the lower right corner of the combustion chamber a temperature level of slightly above 1000 °C was reached. The influence of both temperature boundary conditions at the glass surface on the temperature field was clearly visible. Due to the sharp temperature gradients at the glass surface, large heat fluxes were forced from the combustion chamber to the glass tank.

In contrast to the 2D simulation results for the flow field, in the real glass melting furnace an upward deflection of the flames was observed according to Figure 4.2. This effect reduces the convective heat transfer significantly. The upward deflection is caused by the asymmetrical arrangement of the burners and their orientation normal to the outlet. An additional reason is the thermal lift from the glass surface due to low burner velocities.

The performed simulations were very stable in all variations. To control the convergence behavior, monitors were set up for the total heat transfer rate, temperatures at several positions below the furnace crown. Furthermore, mean values for temperature, velocity and concentration of OH radicals in the entire computation domain as well as temperature and mass flow at the outlet were monitored. The convergence behavior was very satisfying with regard to both, the residuals and the monitors.

Convergent solutions were achieved after only a few thousand iteration steps as shown at the residuals in Figure 5.10. All residuals fell by at least three orders of magnitude to a level below $1 \cdot 10^{-3}$. Especially the residuals for energy and DO-intensity, which are characteristic for heat transfer, showed a very steady decreasing tendency to a sufficient level below $1 \cdot 10^{-6}$.
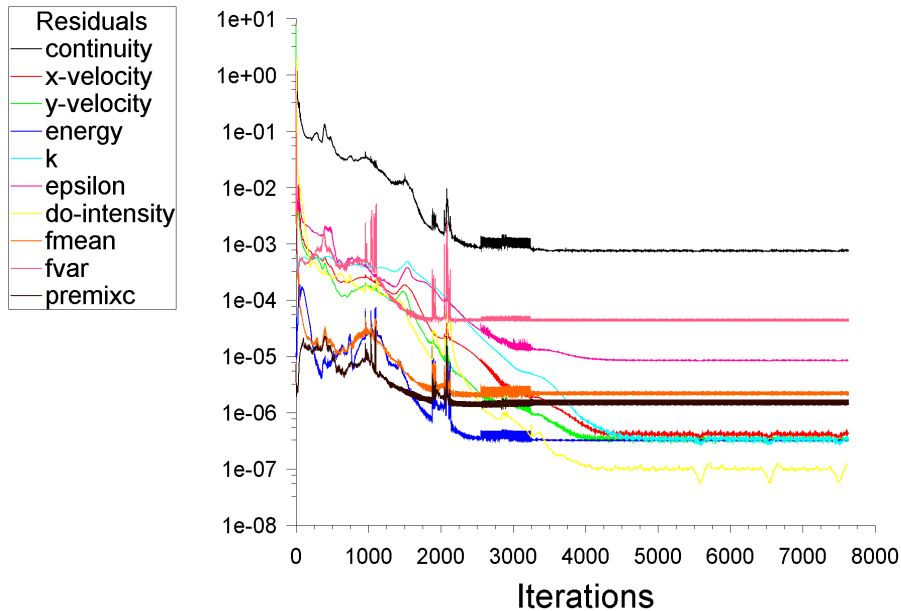
Figure 5.10: Residuals plot of the combustion chamber simulation.

The monitor for the flue gas temperature at the outlet shown in Figure 5.11 remained at a constant value after a rather short settling phase at the begin. The steady value of 1880 K was another strong indicator for a convergent solution.
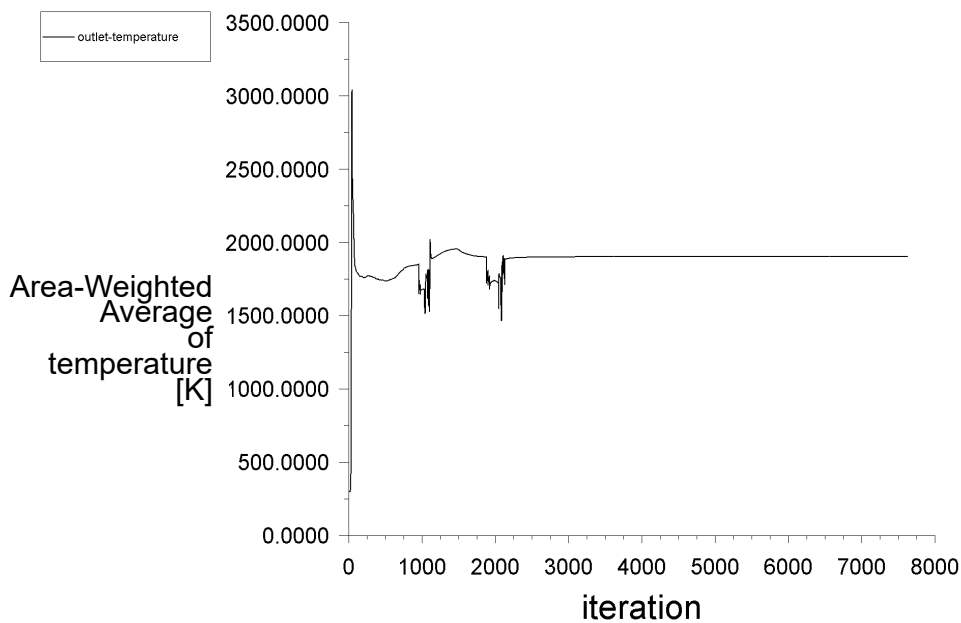
Figure 5.11: Monitor of the combustion chamber outlet temperature.

In summary, through the variety of 2D simulations with different parameters important insights were gained for the further steps, for coupling of the combustion chamber and glass tank in 2D as well as for the further 3D simulations. The most important findings are listed here:

1. During a hybrid initialization no formation of OH radicals in the computational domain was observed. Thus, it was derived that no ignition of the combustion process has occured. This was solved by using a standard initialization at ambient temperature.

2. The specification of a heat flux at the outer walls should be avoided, because this led to high fluctuations in the calculation, which resulted in divergence in extreme cases. By using a mixed boundary condition and the specification of a heat transfer coefficient the stability of the simulation was increased significantly.

3. Despite the use of the sophisticated DO model for radiation, the computational effort remained low. Especially the lower angular discretization with 2 divisions and 1 pixel in each direction at the beginning contributed to this. By an increase to 4 divisions and 3 pixels in each direction for the last several hundred iterations, the residuals and the energy balance error was reduced sufficiently. So it was assumed that time-efficient calculations with the DO model are also possible in the 3D case.

4. Variations in the mesh grid showed that a finer resolution of the mesh in the flame region significantly increased the stability of the simulation and therefore should be also realized for the 3D case. Further details about the different mesh grids were given in Chapter 5.2.

5.4 Simulation of the Glass Tank

After examining the simulation of the stand-alone combustion chamber model, this section deals with the simulation of the glass tank. In this part of the system, primarily the melting and convective mixing of the glass takes place. The glass batch is fed into the doghouse via two conveyor screws. They are located 30 cm above the glass surface. Six individually controllable electrodes for electric boosting are installed in the bottom of the tank. Additionally three electrodes are installed in the throat and and refiner in front of the outlet for conditioning the glass melt.

5.4.1 Geometry and Mesh

As with the combustion chamber, several simplifications were made for the geometry of the glass tank. The two glass batch inlets at the sides were reduced to one single inlet. It was positioned at the opposite side of the tank outlet, directly under the glass surface. An inlet hight of 20 cm was assumed. In analogy to the combustion chamber, the refractory walls of the glass tank were not resolved in the geometry. In the 2D geometry the electrodes for electric boosting were modelled in the form of two rectangular cuttings with a hight of 80 cm. The electrodes were placed in x-direction at the positions $x = 5550\,mm$ and $x = 6450\,mm$. At the glass outlet a vertical geometry piece was added to avoid a hydrostatic pressure gradient along the outlet surface due to gravity forces on the glass. In analogy to the combustion chamber, the outlet geometry of the glass tank was also stretched to avoid negative effects due to flow deflections. The glass tank geometry was also split up in many small sections to simplify the subsequent meshing.

Compared to the combustion chamber, the mesh of the glass tank was much finer in order to increase the stability of the solver. As marked in Figure 5.12, a big part of the geometry was meshed with Tris to improve the information transport between the cells in the expected convection vortices and in the drain to the glass outlet.
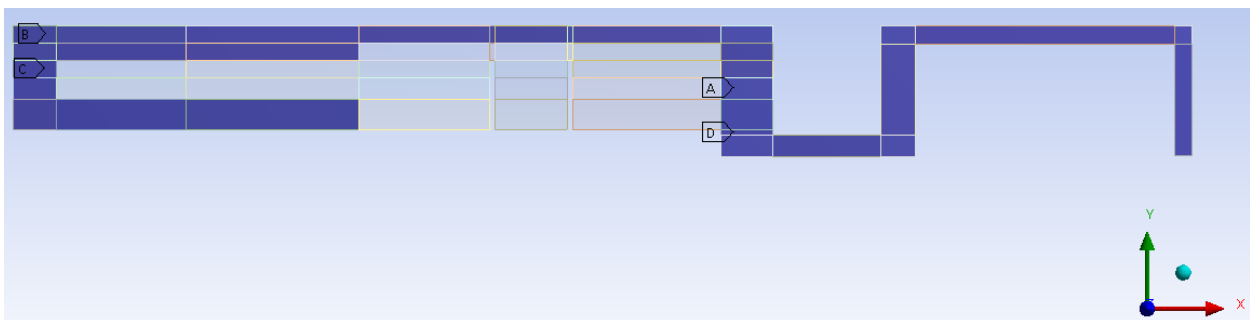
Figure 5.12: Marked sections with Tri elements in the glass tank.

As shown in Figure 5.13, inflation layers were applied to the glass surface in the direction of the combustion chamber and to the electrodes in order to resolve the temperature gradients resulting from the heat transfer into the melt. Furthermore, the region around the glass batch inlet was finely resolved over a large area in order to show the viscosity gradients during melting of the glass in an adequate manner.
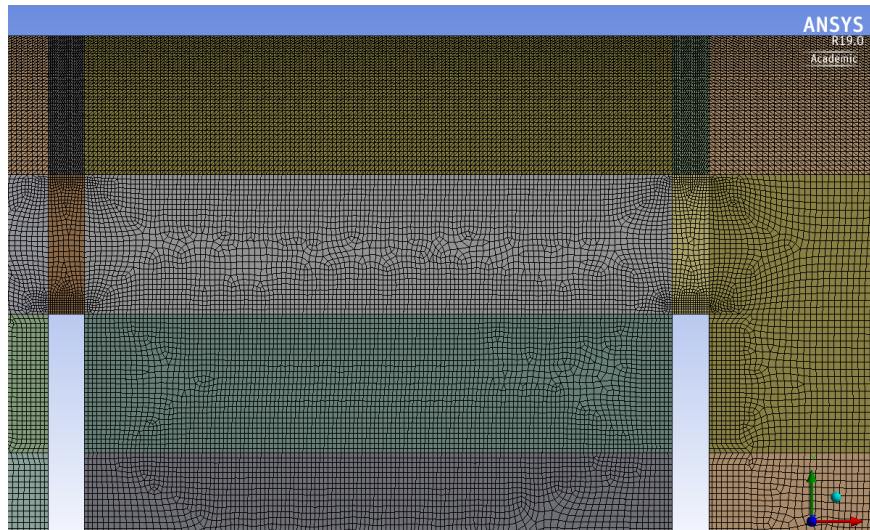
Figure 5.13: Inflation layers at the electrodes and the glass surface.

The corresponding parameters for the mesh of the glass tank were reviewed and summarized in Table 5.9. The more than doubled number of cells compared to the combustion chamber was still no problem for the further computations. The values for common quality measures of the worst cells were also within a satisfying range.

Table 5.9: Mesh grid parameters glass tank.

Parameter	Value
Number of faces	48
Number of cells	199039
Max. skewness (Q_{EAS})	0.78
Mean skewness (Q_{EAS})	0.23
Max. aspect ratio	4.80
Mean aspect ratio	1.69
Min. orthogonal quality	0.35
Mean orthogonal quality	0.13

5.4.2 Models and Input Parameters

The material glass was assigned to the entire computational domain. In this context, special attention was dedicated to the melting of raw materials and the associated phase transition. On the one hand, as already mentioned in Chapter 4.1, for the melting process of glass no heat of fusion has to be applied. Strictly speaking, this only applies to the reheating of cullet. On the other hand, for melting the additionally inserted raw materials a heat of fusion is required in the form of the already mentioned chemical reaction heat $\dot{Q}_{u,glass}$. For this reason, the material glass was defined as a fluid in Ansys, even if it is present in solid form as bulk material before the melting process. Additionally, also for the glass tank submodel a refractory material was created to model the heat transfer at the walls.

The chosen material properties for both, the refractory material and the glass are listed in Table 5.10. Beside the the thermal conductivity, all refractory properties were left the same as in the combustion chamber model. However, for the thermal conductivity the project partner provided a value based on temperature measurements on the outer walls of the tank as well.

Table 5.10: Material properties for the glass tank model.

	Refractory	Glass
Density $\rho \, [kg/m^3]$	3700	See Table 5.11
Specific heat capacity $c_p \, [J/(kgK)]$	1000	See Figure 5.14
Thermal conductivity $k_c \, [W/(mK)]$	3	1.049
Viscosity $\mu \, [Pa\,s]$	-	See Figure 5.15
Absorption coefficient $a \, [1/m]$	0	50 or 125
Scattering coefficient $\sigma_s \, [1/m]$	0	0
Refractive index $n \, [-]$	1	1.5

For the material properties of glass, values from Pye et al. [21] were used, which refer to the SciGlass material database. This database contains data for more than 360 000 glasses in the latest version. It works with data extracted from a large variety of published papers, theses, reports and other sources.

The glass density was assumed to be piecewise linear in terms of temperature. This was necessary because the density above and below the glass transformation region behaves differently. Above the glass transformation region the density was determined based on the material database values. Due to the rather linear behavior, only one additional density value at a temperature of 3000 °C was considered. Since the material inserted to the glass melting furnace is not a solid glass block but rather a loose bulk material, a distinction had to be made for the density below the glass transformation region. Due to the existing air spaces in a bulk material, the density in bulk state is considerably lower than in solid state for the same material. To take this aspect into account, an average of the bulk densities measured in [9] was calculated for the available bulk materials "Cullet, Glass, Average", "Glass Batch Material" and "Glass Powder". This estimate resulted in a value of 1500 kg/m³. Thus, the density definition in Ansys was based on the data points listed in Table 5.11.

Table 5.11: Data points for the piecewise linear density function.

	Temperature [°C]	Density [kg/m³]
Point 1	0	1500
Point 2	650	2423.9
Point 3	3000	2126.9

A temperature-dependent relation based on the SciGlass values was also chosen for the specific heat capacity. A 4th order polynomial with 5 coefficients was considered the best choice. Figure 5.14 shows the temperature effect on the specific heat as well as the mathematical formulation.

$$c_p(T) = 1.099 \cdot 10^{-9}\,T^4 - 4.595 \cdot 10^{-6}\,T^3 + \\ + 0.006163\,T^2 - 2.504\,T + 1178.94$$
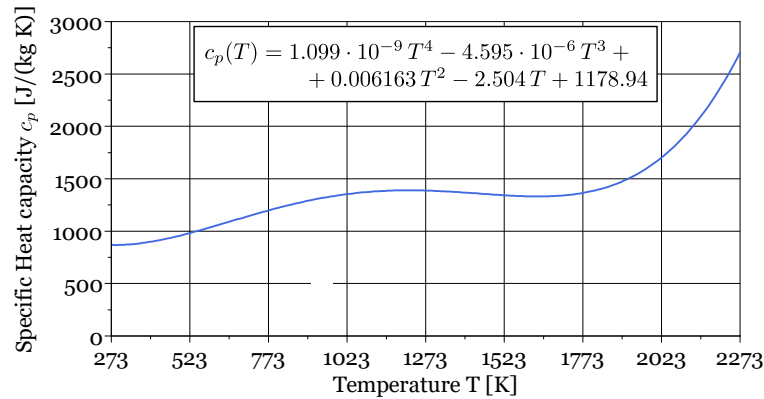
Figure 5.14: Temperature-dependent polynomial for the specific heat capacity.

Additionally, the dynamic viscosity was implemented as temperature-dependent function. A sufficiently accurate approximation of the target values with only one polynomial was not possible. Therefore, the viscosity was approximated piecewise with two different polynomials. Furthermore, a cut-off below 600 °C was performed to ensure the numerical stability of the CFD simulations. In general, for variable material properties the maximum and the minimum value of the respective property should not differ by more than 5 orders. Consequently, a cut-off value of 2050 Pa s was chosen here. The viscosity curve from literature and the approximation subdivided into three areas with constant cut-off and two 6$^{\text{th}}$ order polynomials with 7 coefficients for each of them are shown in Figure 5.15.

$$\mu_1 = 2050\,Pa\,s$$

$$\mu_2(T) = 2.247 \cdot 10^{-12}\,T^6 - \\ - 1.570 \cdot 10^{-8}\,T^5 + \\ + 4.563 \cdot 10^{-5}\,T^4 - \\ - 0.07070\,T^3 + 61.58\,T^2 - \\ - 2.860 \cdot 10^4\,T + 5.538 \cdot 10^6$$

$$\mu_3(T) = 1.668 \cdot 10^{-17}\,T^6 - \\ - 2.388 \cdot 10^{-13}\,T^5 + \\ + 1.414 \cdot 10^{-9}\,T^4 - \\ - 4.430 \cdot 10^{-6}\,T^3 + \\ + 7.755 \cdot 10^{-3}\,T^2 - \\ - 7.201\,T + 2775.3$$
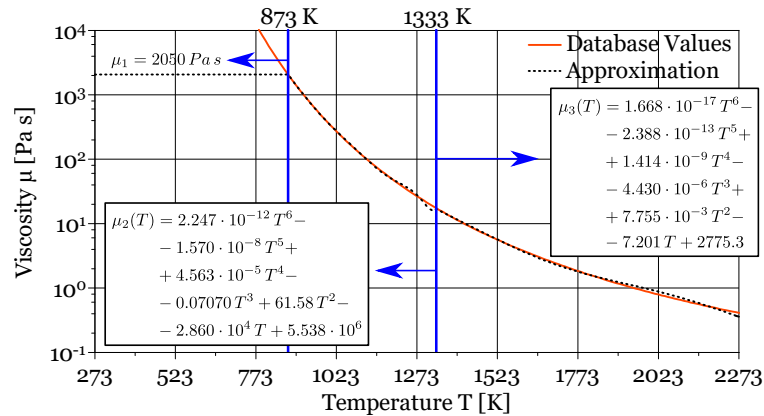
Figure 5.15: Temperature-dependent piecewise polynomials for the dynamic viscosity.

The thermal conductivity was defined with a constant value due to its weak temperature dependence. At this point, it should be mentioned that the heat transport in the glass tank is highly temperature dependent and nonlinear. However, at the high temperatures in the melt, heat transport takes place mainly due to thermal radiation, which is characterized by the absorption coefficient.

The challenge in choosing an adequate absorption coefficient was due to the great variation of the values over the wavelength spectra. In addition, the glass composition also has a considerable effect on the absorption behavior. Since the exact glass batch composition was not known, a familiar absorption spectra of float glass (cullet) from the SciGlass database was used. Most glasses show a sharp increase of the absorption coefficient between a wavelength of 2.5-3 µm, as

shown in Figure 5.16. At an expected temperature level of 1723 K in the glass melting furnace, the incident radiation spectra, shown in Figure 5.16 for blackbody radiation with the Planck's law, is in the range of the low absorption value with a share of 76 %. In order to better estimate the degree of influence on the simulation results, it was decided to perform the simulations with two different values for the absorption coefficient. First, only the mean absorption coefficient of 50 1/m in the area of low absorption was used. Second, the mean absorption coefficients of the areas with low and high absorption were weighted with the respective share of the incident radiation. This resulted in a value of 125 1/m.
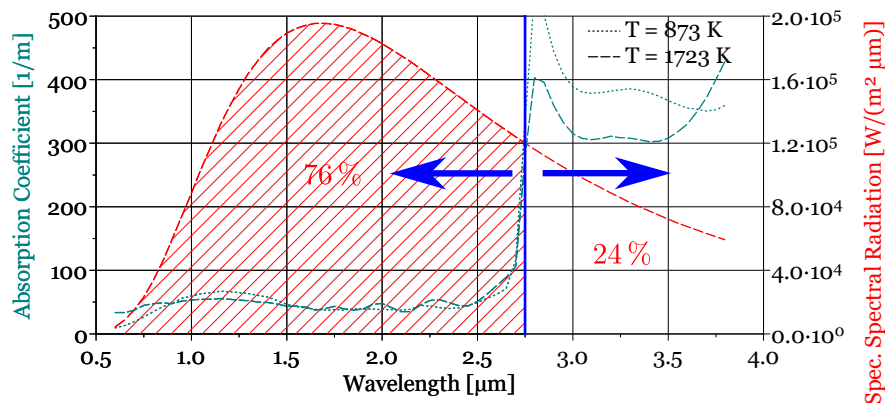
Figure 5.16: Absorption spectra of float glass (cullet) and blackbody radiation.

As with the combustion chamber simulation, scattering was neglected in glass. This was not the case for refraction. For the refractive index a constant value was defined, since this value has only a slight wavelength dependence.

The different sections of the boundaries for applying the appropriate boundary conditions at the glass tank were also highlighted and indicated with the letters (a) to (h), as shown in Figure 5.17. Thus, boundaries were defined for the glass batch inlet (a) and for the glass outlet (b) on the opposite side. Furthermore, separate boundaries were defined for the walls at the outlet area (c), the electrodes for electric boosting (d) as well as for the indirect (e) and direct zone (f) on the glass surface. In analogy to the combustion chamber, at the glass surface a distinction was made between direct and indirect zone to roughly approximate the actual temperature profile. Compared to the combustion chamber model, the extensions of the two zones remained unchanged. Additional boundary conditions were defined for the refractory walls (g) and the free surface at the glass channel behind the glass melting combustion chamber (h), which is in contact with the ambient atmosphere.
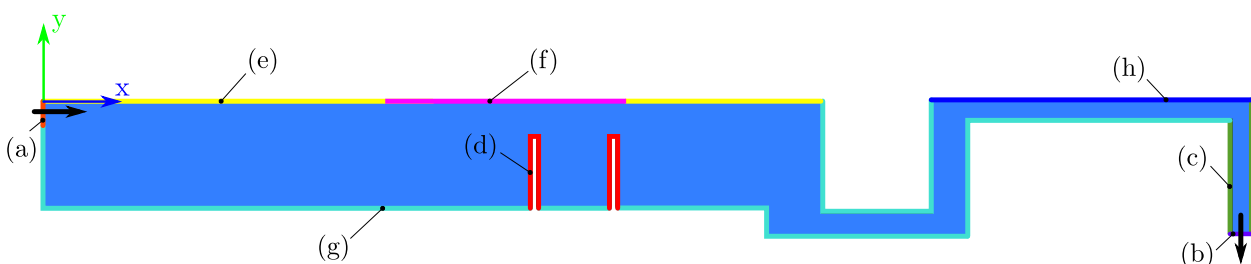
Figure 5.17: Glass tank boundary conditions numbered and indicated in different colors.

Detailed parameters for all boundary conditions at the glass tank are listed in Table 5.12. The glass batch inlet (a) was configured as mass flow inlet with a mass flow rate and inflow temperature. The glass outlet (b) was defined as pressure outlet. Besides the gauge pressure, the temperature for possible backflows was specified in accordance with the calculations for the energy balance in Table 5.1. The walls at the outlet area (c) were defined as adiabatic walls. At the surfaces of the electrodes for electric boosting (d) a heat flux was predescribed. It was calculated by referring the transferred electric power to the electrode surface with the electrode perimeter and a reference value of 1 m for depth.

At both boundaries on the glass surface (e) and (f) a certain temperature was given. The temperature values were determined empirically. Analogous to the combustion chamber, a mixed boundary condition was imprinted on the remaining glass tank walls. Therefore, the wall was specified with a certain thickness and the material refractory. Whereas the free surface (h) was specified as stationary wall with a mixed boundary, zero wall thickness and no shear stresses to guarantee free stream velocity at the boundary.

Table 5.12: Boundary condition parameters at the glass tank.

Location	Parameter	Unit	Value
a	Mass flow rate	kg/s	1.086
	Temperature	K	300
b	Gauge pressure	Pa	0
	Backflow temperature	K	1275
d	Heat flux	W/m²	181500
	Emissivity	–	0.9
e	Temperature	K	1573
	Emissivity	–	0.9
f	Temperature	K	1973
	Emissivity	–	0.9
g	Heat transfer coefficient	W/(m²K)	10
	Free stream temperature	K	300
	External emissivity	–	0.8
	External radiation temperature	K	300
	Internal emissivity	–	0.5
	Wall thickness	m	0.3
h	Heat transfer coefficient	W/(m²K)	2
	Free stream temperature	K	300
	External emissivity	–	0.8
	External radiation temperature	K	300
	Internal emissivity	–	0.5

Due to low expected velocities in the flow field in the order of some mm/s, no turbulence model was required and a laminar viscosity model was chosen. Radiation was considered first with the rosseland model because of its good suitability for optically thick media and the low computational costs. However, Choudhary et al. [8] found an increasing error of the rosseland

model for glasses with relatively low optical thickness compared to the more general and complex DO model. For this reason, it was additionally checked whether the use of the DO model leads to a significantly higher calculation effort. The settings for the DO model were the same as in the combustion chamber simulation.

The pressure-velocity coupling was solved with the SIMPLE scheme. The spatial discretization was performed for the gradients with "Least Squares Cell Based" and for the pressure it was done "Body Force Weighted". With this scheme lifting forces can be simulated better. For radiation the spatial discretization was performed in "First Order Upwind" and for all remaining equations in "Second Order Upwind". The applied under-relaxation factors for the pressure-based solver are shown in Table 5.13.

Table 5.13: Under-relaxation factors for the solver at the glass tank.

Parameter	Value
Pressure	0.7
Density	1
Body forces	1
Momentum	0.3
Energy	0.99
Discrete ordinates	0.99

5.4.3 Discussion and Results

As already mentioned for the combustion chamber, a quantitative comparison was not possible in 2D due to the highly simplified geometry. At the glass tank one reason for this was especially the reduction to one single glass batch inlet, which was placed on the opposite side of the outlet in the 2D geometry, in contrast to the actual position on both side walls. This led to an expansion of the glass batch blanket on the glass surface, which was not representative for the real situation. Another reason was the arrangement of the electrodes for electric boosting. In the 2D geometry, the two rectangular cuttings formed a barrier for the glass melt, which could only be passed via the small area above the electrodes. Thus, the glass tank was unintentionally separated into three regions with limited interaction. The aim of the CFD simulations in 2D was to determine the influence of different absorption coefficients, to confirm the applicability of the different computation models and to establish the appropriate radiation model for further simulations. An additional focus was put on optimizing the computation time.

The obtainted simulation results for the two chosen absorption coefficients were evaluated and compared in detail. The temperature fields of the glass tank are shown in Figure 5.18. The overall temperature level in the tank was approximately 500 K higher at an absorption coefficient of 50 1/m than at an absorption coefficient of 125 1/m. At high absorption the temperature in the region between inlet and electrodes was mainly around 600 °C. In contrast, low absorption resulted in this region homogeneous thermal stratification with temperatures between 1000 °C at the bottom of the tank and just above 1900 °C close to the glass surface. The blue band of low temperature at the inlet near the glass surface indicated the glass batch blanket. In any case, the

glass batch blanket was much larger at high absorption and and covered approximately half the length of the glass tank. However, at low absorption, the glass batch blanket only reached a length of about 1 m. Across the entire glass tank, a thermal separation into three regions by the electrodes was clearly visible. The temperature levels became steadily higher towards the outlet. Also a noticable energy input by electric boosting took place in the tank and was clearly visible by hot spots just behind the electrodes. After leaving the glass tank, the temperature in the glass channel and the outlet geometry remained quite stable without a noticable drop in temperature. The temperature at the outlet was 1750 °C at low absorption, but only 1220 °C at high absorption.

$a = 50 \ 1/\text{m}$

Temperature in °C

$a = 125 \ 1/\text{m}$
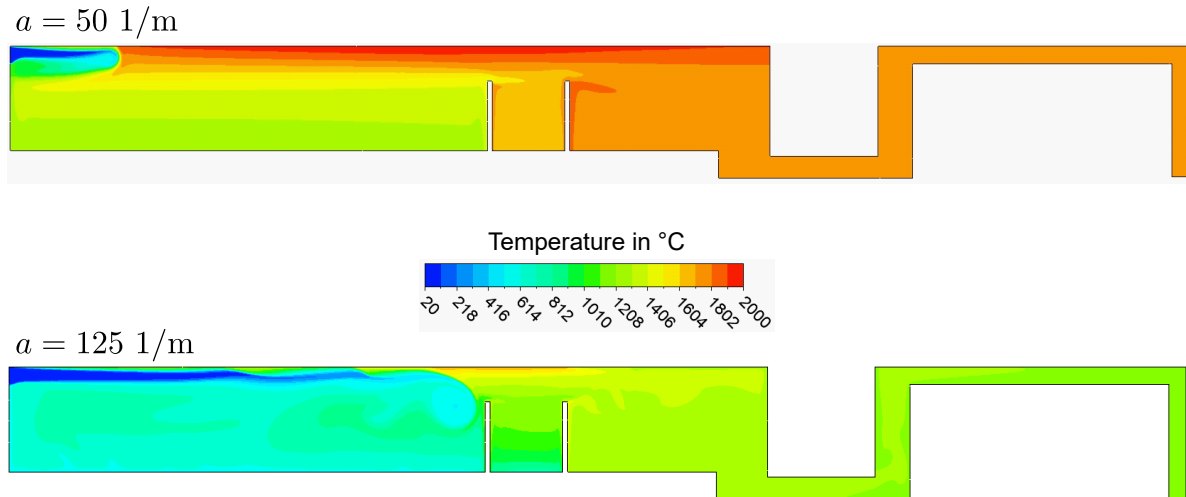
Figure 5.18: Temperature fields at the glass tank for the different absorption coefficients.

In Figure 5.19 the viscosity fields at the glass tank are shown for the absorption coefficients under investigation. High values of dynamic viscosity, coloured in red, indicate the solid phase of the glass batch, while low values, colored in blue, represent the liquid glass melt. For the interpretation of the results, the theoretical principles of optical thickness have to be considered. The optical thickness of a medium is defined according to Equation (3.4). Since the scattering coefficient for glass was set to zero in this work, this formulation is simplified to:

$$\tau_\lambda = a \cdot L \tag{5.25}$$

In optically thick media an increasing amount of incident radiation is absorbed by the medium and a reduced amount will pass through it. In other words, with increasing absorption coefficient the upper layers of the glass melt will absorb more radiation and emit less radiation to the lower layers in the glass tank. This relationship is reflected in Figure 5.19 in a way, that at a = 50 1/m a significantly better melting was achieved, whereas at a = 125 1/m there was a larger area of unmelted or insufficiently melted glass batch. At high absorption the red domains close to the front wall below the glass batch inlet and close to the bottom wall up to the electrodes indicated high viscosity in these areas. This may be caused by heat transfer through the glass tank walls and must be kept in mind during further simulations. Differences in the viscosity fields for low and high absorption were just recognized in the glass tank region in front of the electrodes. From the electrodes to the outlet the whole computational domain is coloured in blue, which means that in both cases the glass batch was completely melted before leaving the glass tank.

$a = 50 \ 1/m$

Dynamic Viscosity in Pa s

$a = 125 \ 1/m$
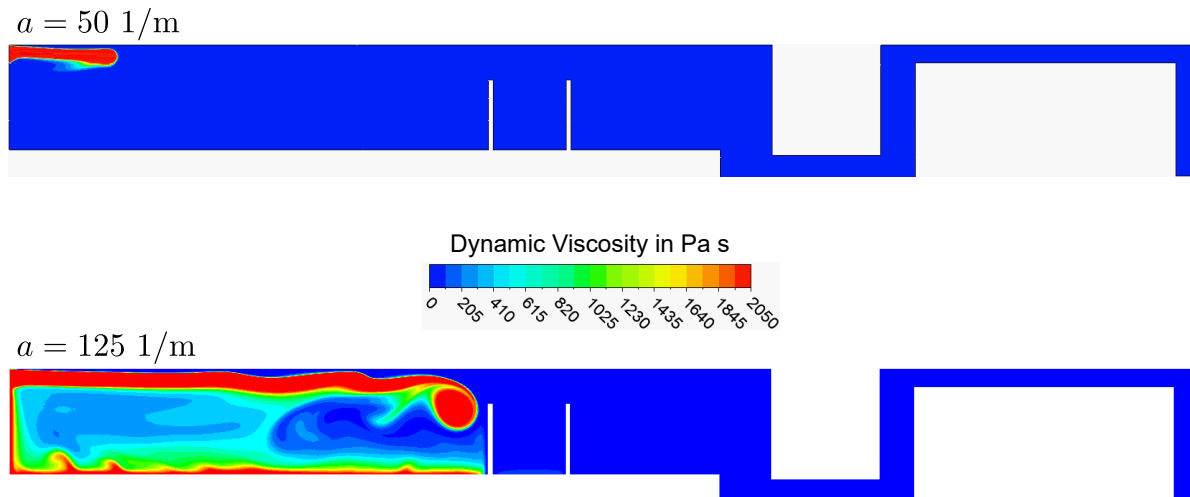
Figure 5.19: Viscosity fields at the glass tank for the different absorption coefficients.

At the flow fields for the investigated cases, shown in Figure 5.20, in the entire glass tank quite small velocity magnitudes with a maximum of 15 mm/s were detected. At low absorption, the convective transport of melted material at the bottom of the glass batch blanket was clearly visible due to the increased velocity magnitudes in connection with the streamline arrows. In all three regions of the glass tank convection vortices were formed for low and for high absorption. Overall, the flow fields in the simulation results corresponded remarkably well with the flow fields described in literature. Nevertheless, a deficit of the 2D simulation already mentioned above, was shown in Figure 5.20. Due to the barrier effect of the electrodes for the flow, the cooler melt was trapped in the inlet region. In addition, there was a vortex formation between the electrodes which led to a further deviation of the results compared to the current flow. This error had to be accepted for 2D CFD simulations and demonstrated the necessity of 3D CFD simulations. Furthermore, the simplification to just one single glass batch inlet resulted in higher flow velocities, which has a negative effect on the glass melting process.

$a = 50 \ 1/m$

Velocity Magnitude in m/s

$a = 125 \ 1/m$
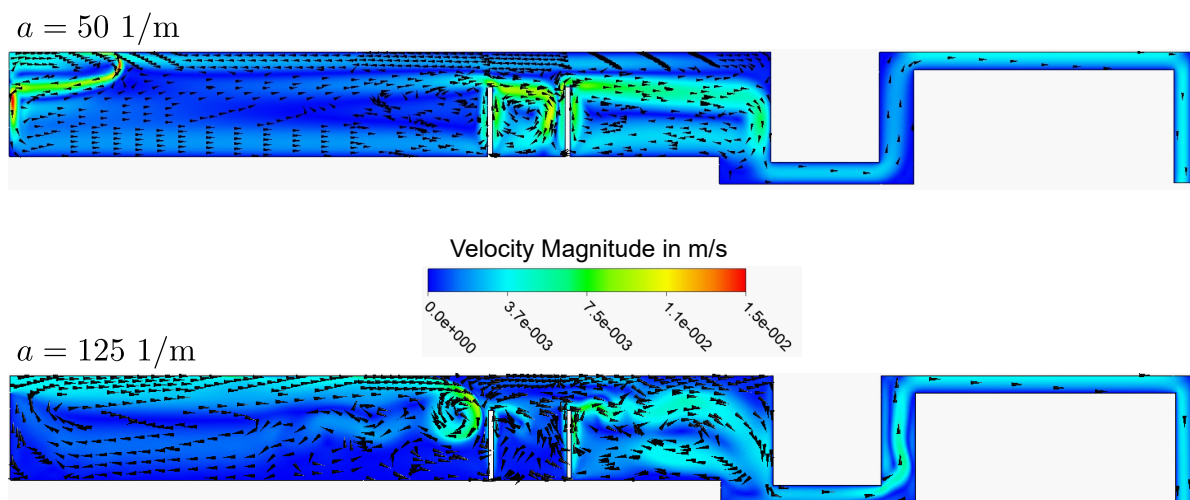
Figure 5.20: Velocity fields at the glass tank for the different absorption coefficients.

Furthermore, an attempt was made to improve the consideration of the actual absorption behavior of glass. Using the gray-band model, the absorption behavior was divided in two bands with different absorption.

The bands were defined as follows:

$$a = \begin{cases} 120\,m^{-1}, & \lambda < 2.5\,\mu m \\ 960\,m^{-1}, & \lambda > 2.75\,\mu m \end{cases} \tag{5.26}$$

The simulation achieved a good compromise with results between those for constant absorption. However, the improvements in gray-band modeling could not be justified by the disproportionate increase in calculation time.

In general, the glass tank simulations were more challenging and less stable compared to those at the combustion chamber. First, this may be due to the strong temperature dependence of some material properties of glass. Second, natural convection is predominant in the glass tank. In this context, small deviations in glass temperature and density have considerable effects on the entire flow field.

Based on the results of the 2D simulations of the glass tank the following conclusions were formulated:

1. Basic physical relationships regarding the absorption coefficient could be reproduced with the numerical models. In order to ensure a calculation that is as time efficient as possible, a constant absorption coefficient should be assumed for the entire wavelength spectra.

2. In general, the temperature levels at the simulations with high absorption were more reasonable. Even though the viscosity results in the tank region between inlet and electrodes still showed potential for improvement. Thus, system coupling in 2D and all 3D simulations should be performed with an absorption coefficient of 125 1/m.

3. For all simulations of the glass tank the computing time was considerably longer compared to the combustion chamber. Therefore, it was derived to create a glass tank mesh with as few elements as possible for the 3D simulations. At the same time, mesh studies showed that in order to achieve a convergent solution, a high resolution of the mesh must be achieved in the transition region between solid and liquid phase.

4. A transition to 3D simulations is necessary, because the 2D abstraction of the geometry led to intolerable simplifications and a quantitative comparison with measurements was not possible.

With the finalization of the stand-alone 2D CFD simulations, in several aspects a solid base for the following system coupling in 2D and further simulations in 3D was created. Numerical models were checked for plausibility and additional conclusions were made about the computational effort and meshing strategy for the combustion chamber as well as for the glass tank.

5.5 System Coupling

In order to simulate the heat transfer between combustion chamber and glass tank and to have an idea of the total system behavior at the glass melting furnace, an iterative, coupled method was used. The glass surface acts as an interface between the two calculation domains, which are treated in the submodels.

5.5.1 The Iterative Coupled Method

A flow chart of the underlying iterative loop is shown in Figure 5.21. In the first iteration step of the combustion chamber an empirically determined constant temperature of $T_0 = 1400\,°C$ was applied to the glass surface. The heat flux profile on the glass surface $\dot{Q}_{melt,i}$ resulted from the simulation of the combustion chamber submodel. Since the heat was transferred from the combustion chamber to the glass tank (negative sign), a sign reversal was performed externally in Matlab. In the next step, the heat flux profile $\dot{Q}_{melt,i,new}$ obtained with Matlab was applied to the glass tank submodel in form of a boundary condition on the glass surface. After performing the simulation of the glass tank the corresponding temperature profile on the glass surface T_{i+1} was compared with the profile of the previous iteration step T_i, as written in Equation (5.27).

$$E_{rel,T} = \frac{T_i - T_{i-1}}{T_{i-1}} \cdot 100 \tag{5.27}$$

Beginning with the second iteration step, the heat flux profiles were additionally compared according to Equation (5.28).

$$E_{rel,\dot{Q}} = \frac{\dot{Q}_{melt,i} - \dot{Q}_{melt,i-1}}{\dot{Q}_{melt,i-1}} \cdot 100 \tag{5.28}$$

If the mean values of both relative deviations $\bar{E}_{rel,T}$ and $\bar{E}_{rel,\dot{Q}}$ were less than 0.5 %, the precedure was aborted. If this was not the case, the two temperature profiles were averaged externally in Matlab according to Equation (5.29).

$$T_{i+1,new} = \frac{T_i \cdot i + T_{i+1}}{i + 1} \tag{5.29}$$

Hereby i was the number of the current iteration step. The given equation averaged the temperature profiles of all iteration steps. Furthermore, this damping had positive effects on the convergence behavior of the iteration procedure. After averaging the resulting temperature profile, $T_{i+1,new}$ was again applied as boundary condition to the combustion chamber submodel.
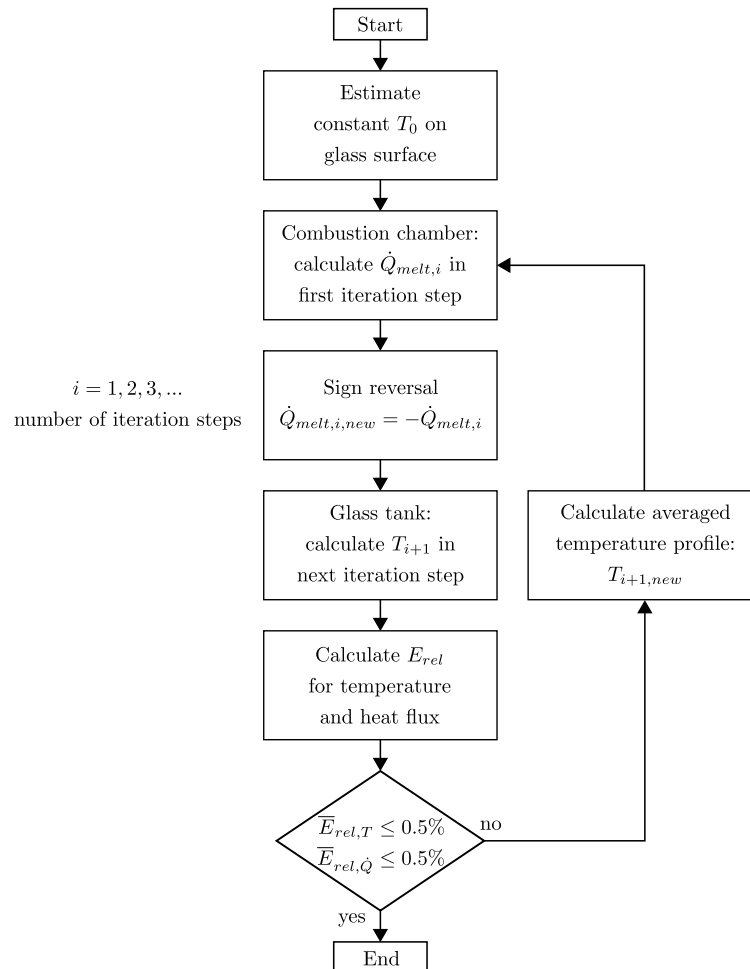
Figure 5.21: Flow chart of the iterative coupling procedure.

The procedure presented here differs in three essential points from previously used iterative methods [1, 8, 12]:

1. In previous simulations, either highly simplified geometries were used or convective heat transfer was not taken into account, since it only accounts for about 10 % of the total heat flow. In the method used here no simplifications, neither geometrically nor in terms of heat transfer were made. By using the total surface heat flux on the glass surface for the calculations both radiation and convection (natural and forced) were taken into account.

2. In previous calculations a relative deviation of 1-10 % between the successive iterations was used as termination criterion for the iteration loop described in Figure 5.21. Instead the application presented here assumed a level of 0.5 %. This value was chosen because it is within the tolerance of the used thermocouples for measurements at the production plant. Thus, errors could be minimized by the iterative procedure or set in a metrological context.

3. If the procedure did not converge after one step, the temperature values T_{i+1} were not used for the new calculation, but an averaging was carried out. Depending on the fluctuations between the iteration steps a damping of the results was reached. The damping was achieved by using the formulation in Equation (5.29) instead of a conventional mean value.

5.5.2 Models and Input Parameters

For system coupling the meshes already described at the stand-alone combustion chamber and glass tank simulations were used without any changes. In contrast to the meshes, adaptions were made for the boundary conditions at the interfaces on the glass surface. For this purpose, the two boundaries (e) and (f) at the combustion chamber and the glass tank model were combined to one single boundary. The combustion chamber boundary was specified as temperature boundary and the glass tank boundary was specified as heat flux boundary.

Additionally, the chemical reaction heat $\dot{Q}_{u,glass}$ has not been considered in the stand-alone simulations of the glass tank yet. In Chapter 5.1.1, two different approaches were sketched for implementation of this term in the CFD simulations. In this work, the path by using a negative source term was preferred, since this tool ensured the one-time removal of the chemichal reaction heat. In contrast, the alternative path by adapting the specific heat capacity offered the risk of unpredictable effects in the case of an incomplete crossing of the the corresponding temperature range. The size of the source term was calculated for the 2D simulation by using the hypothetical volume of the glass tank V'_{GT} with a reference depth of 1 m according to Equation (5.30).

$$\frac{\dot{Q}_{u,glass}}{V'_{GT}} = \frac{-132.3\,\text{kW}}{8.8\,\text{m} \cdot 1.2\,\text{m} \cdot 1\,\text{m}} = \textbf{-12.53\,kW/m}^3 \tag{5.30}$$

For the combustion chamber as well as for the glass tank, all further settings for materials, boundary conditions, models and solvers were copied from the stand-alone simulations. In order to apply the temperature and heat flux profiles to the respective boundary conditions, it was necessary to position the coordinate systems of the two submodels in a way that for any point on the glass surface the x- and y-position is identical in both submodels. The origins of the coordinate systems are sketched in Figure 5.8 for the combustion chamber and in Figure 5.17 for the glass tank.

The coupling procedure was done in Ansys by writing the obtained temperature or heat flux profile into a profile file after each simulation. After the required adaptions in Matlab, the new profile was then read into the new simulation and selected as input parameter in the appropriate boundary condition for the glass surface.

5.5.3 Discussion and Results

During the coupling process, sufficient computation steps were performed for each simulation. The first iteration of the combustion chamber required about 4 000 computation steps to reach a convergent solution. In contrast, the glass tank required about 10 000 steps for the first coupling iteration. All further coupling iterations required approximately 2 000 computation steps for the combustion chamber and about 3 000 computation steps for the glass tank. The termination criterion for system coupling according to Equations (5.27) and (5.28) was fulfilled after 8 iteration steps with a value of 0.42 % for the heat flux profile and a value of 0.03 % for the temperature profile. In total the coupling process took about 8 hours.

The profiles for the coupling variables over the iteration steps are given below. The development of the heat flux profile at the glass surface is shown in Figure 5.22. The profiles for the different iteration steps were named from IT 1 to IT 8. They resulted from the combustion chamber simulation and were plotted after a sign reversal. These profiles were subsequently applied to the boundary condition at the glass tank simulation. The profile after the first combustion chamber iteration showed a relatively uniform distribution due to the constant temperature boundary condition at the glass surface. In fact, this was of course not the case, since the glass batch in the inlet area had a much lower temperature compared to the starting temperature of 1400 °C and the temperature in the hot spot was much higher. Since heat fluxes are driven by temperature differences, a high heat flux with a maximum value of about 700 kW/m² was observed in the first 3.5 m of the combustion chamber during the following iterations due to the unmelted glas batch in this region.The heat flux drop at an x-position of about 4.2 m was not reasonable and possibly due to the simplifications made in the 2D geometry. The next drop corresponded to the position of the first row of electrodes. Between iteration 2 and iteration 5, there were observed even negative heat fluxes towards the outlet. However, with further iterations a strong smoothing of the profile was achieved at this point, so that the drop almost disappeared. The further profile showed a constant distribution with a slightly lower heat flux on the last 0.5 m. This reduction was probably due to the more indirect influence of the burner flame in this region.

Additionally in Figure 5.23 the distribution of the temperature profile at the glass surface is depicted. Here the profiles resulted from the glass tank simulation. These profiles were subsequently externally averaged in Matlab with the previous temperature profiles and then applied to the boundary condition at the combustion chamber simulation of the following iteration step. The profile after the first glass tank iteration showed a sharp temperature increase at the inlet region, starting at almost 390 °C directly at the inlet. At the end of the increase, the temperature stabilized at a level of 1420-1430 °C. At the first row of the electrodes located at $x = 5.5\,m$ another local maximum was observed due to the electric power input. In the region between the first and the second row of electrodes the temperature reached a maximum value of 2060 °C. After a minor decrease to 2000 °C a slightly higher temperature drop was also visible on the last 0.5 m of the glass tank. With further iterations the temperature increase at the inlet became much sharper with a starting temperature directly at the inlet of just below 900 °C. About 3.2 m after the inlet a second local maximum was formed from a temperature level of 1530 °C to a level of 1750 °C. With respect to the sudden drop of the heat flux at the same position in Figure 5.22, this clearly indicated the expansion limit of the glass batch blanket there. In the region before, relatively strong fluctuations were still detected even between the last iteration steps. This again indicated the difficulties for a satisfying modelling of the melting process in CFD. At the first row of electrodes, the high temperature gradients developed with increasing iteration steps into a rather smooth and only weakly visible, temporary temperature drop of about 25 K, which was also observed at the heat flux profiles. Towards the end of the glass tank, a quite stable temperature profile is obtained. Only on the last 0.5 m the temperature in the indirect zone droped again by 30 K to a level of 1670 °C and stabilized in this range.
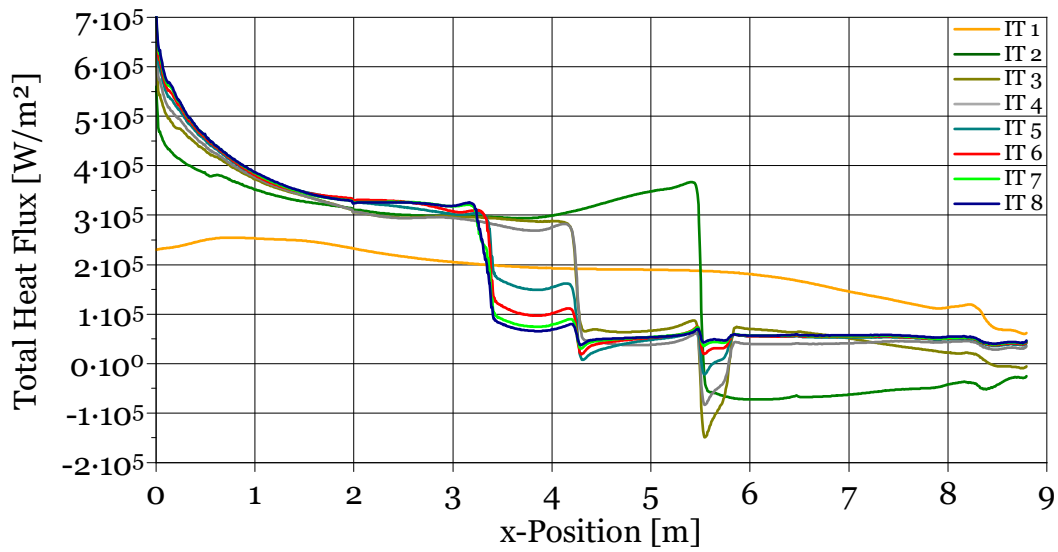
Figure 5.22: Iteration steps of the heat flux profiles at the glass surface in the glass tank.
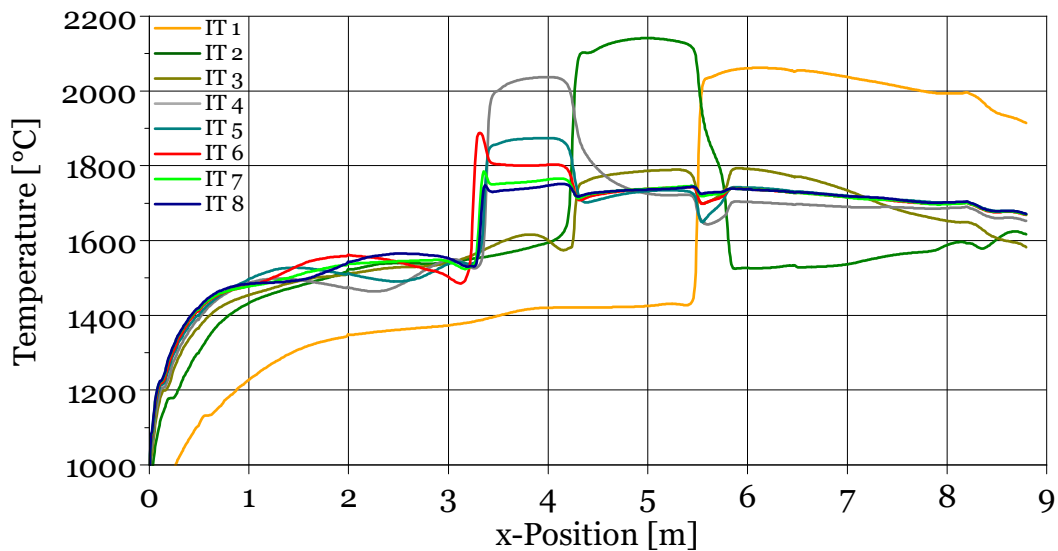
Figure 5.23: Iteration steps of the temperature profiles at the glass surface in the combustion chamber.

The results of the system coupling process in terms of the temperature and flow field of the last iteration step performed were summarized in Figure 5.24 and 5.25. At the temperature field in Figure 5.24 the interface between both submodels was marked with a dashed black line. The temperature distribution in the combustion chamber was characterized by a rather homogenous development with a magnitude of 1500-1800 °C in the whole domain outside the region with direct influence of the combustion. This region of direct influence had an extent from the burner inlets to the opposite end of the glass surface, similar to that in the uncoupled simulation of the combustion chamber. The temperature level in this region was noticeably higher. The highest value of 2991 °C was computed inside the burner flame. In contrast to the uncoupled simulation the maximum value was 91 K or almost 3 % higher. In the combustion chamber close to the glass surface, the coupled simulation results showed similar temperature values but significantly lower temperature gradients. This was due to the higher values in the temperature profile compared to

the constant temperature boundary condition at the uncoupled solution. Above the glass batch blanket, directly at the glass batch inlet, the temperature decreased rapidly from over 2100 °C to about 1770 °C. The secondary vortex in the lower right corner formed similarly to the uncoupled solution with a temperature of around 1000 °C in this region.

In the glass tank the temperature level in the region between glass batch inlet and the first row of electrodes was approximately 200 K higher than in the uncoupled solution. As a result, the batch blanket was only half as long as in the uncoupled simulation. The heat dissipation at the bottom of the glass tank was now particularly visible in this region with the three cold spots with a temperature below 600 °C. Furthermore, a steady temperature increase in the regions before, between and after the rows of electrodes was observed due to the significant electric power input. Nevertheless, the glass tank was thermally separated into three regions due to the barrier effect of the electrodes in the 2D geometry even in the coupled solution. After leaving the glass tank, the temperature in the glass channel and the outlet geometry dropped slightly by 100 K. The temperature at the glass outlet had a value of 1400 °C. In general, the temperature results were very promising, since the new source term considered also the dissipated reaction heat of the glass melting process. In addition, the overall temperature level was significantly higher and more plausible than in the uncoupled solution results.

In Figure 5.25, the velocity magnitudes with streamlines and direction vectors are depicted for the coupled solutions of the combustion chamber and the glass tank. The velocity magnitudes at the combustion chamber were given in m/s and at the glass tank in mm/s. Similar to the uncoupled simulations, the results at the combustion chamber showed a flame shape that did not correspond to reality. Approximately 1 m after leaving the burner, the flow field was significantly deflected downwards and separated into the secondary vortex in the lower right corner and the main path along the glass surface towards the flue gas outlet at the chimney. Below the furnace crown not far from the outlet moderate secondary flows were detected. A possible reason is the deflection of the main stream into the chimney. Above the glass surface the velocity magnitude in the flow field reached maximum values of 7 m/s - 8 m/s. At the fuel and oxidizer inlet the velocity magnitudes were below 1 m/s. However, the actual magnitudes at the inlets were within a range of 14 m/s - 16 m/s. The reason for this significant lower velocity magnitudes in the simulation results was the neglected combustion chamber depth normal to the view plane, as already explained in detail at the uncoupled combustion chamber simulation results.

At the glass tank quite small velocity magnitudes with a maximum of 12 mm/s were detected. The convective transport of melted material at the bottom of the glass batch blanket was clearly visible due to the increased velocity magnitudes in connection with the flow arrows. Compared to the flow field for the uncoupled solution with the same absorption coefficient of $a = 125\,1/m$ the glass batch blanket was significantly reduced in size. This was certainly due to the increased glass surface temperature with system coupling in this region. In all three regions of the glass tank convection vortices were formed also in the coupled state. Even if the specific characteristics varied quite remarkably from the uncoupled solution at some places. For instance the main vortex below the glass batch blanket was much more clearly visible by the arrows. Additionally, the vortice between the rows of electrodes was noticably stronger with velocity magnitudes of about 7 mm/s compared to approximately 3.5 mm/s at the uncoupled solution. Also in the last third of the glass tank a vortice with significantly higher velocity but even smaller size was recognized. Nevertheless, the earlier mentioned modelling deficits in 2D, especially the barrier effect of the

boosting electrodes, were also found in the coupled solution. Overall, the velocity magnitudes in the glass tank flow field were slightly increased, which corresponded with the higher mean temperature at the glass surface of 1625 °C. Compared to the lower temperature with a constant value boundary at the uncoupled solution this was a significant temperature difference of 225 K.

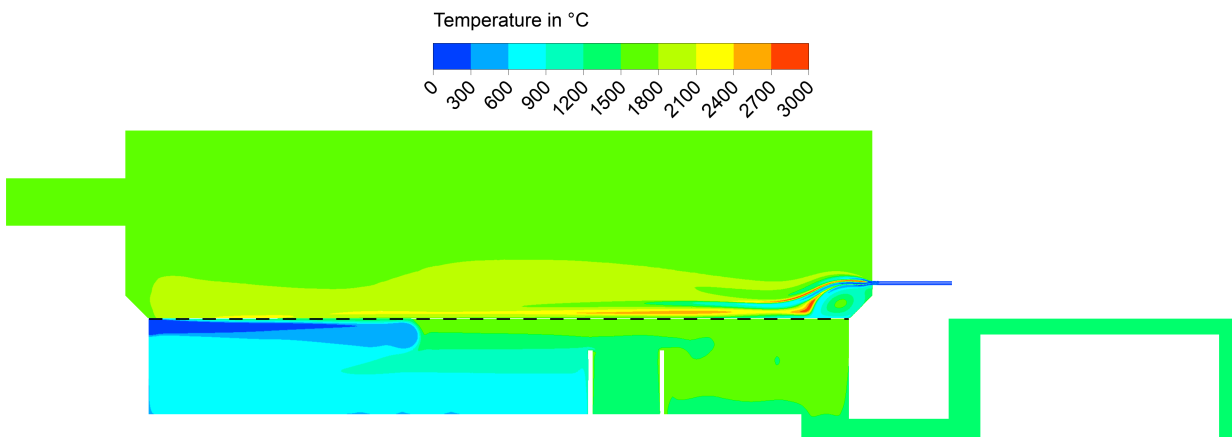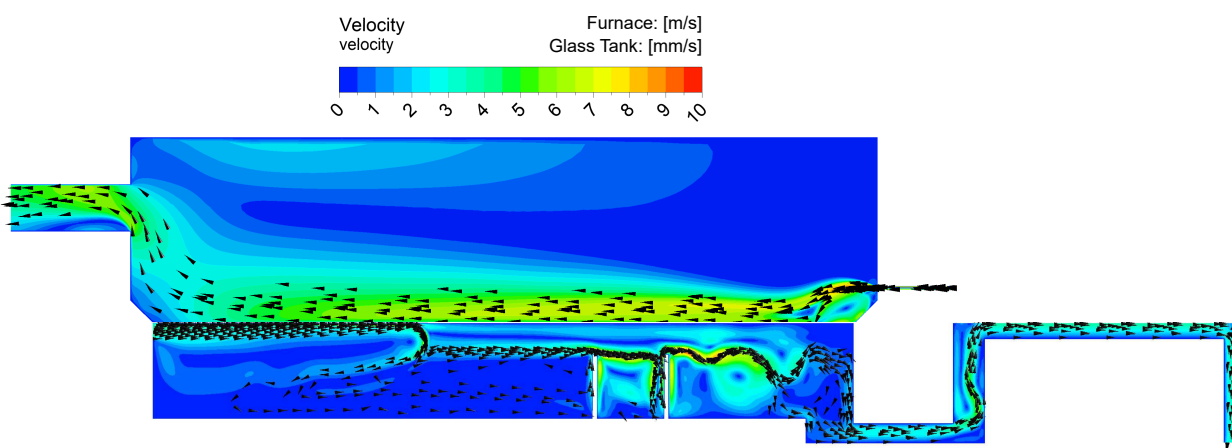Figure 5.24: Temperature field in the coupled 2D glass melting furnace.

Figure 5.25: Flow field in the coupled 2D glass melting furnace.

In summary, with system coupling the applicability of the created materials, the used models and the defined boundary conditions was confirmed. The simulation setup for both submodels was found to be suitable for the subsequent 3D simulations. In addition, the successful proof of concept for the chosen approach of system coupling was provided with the completion of the 2D investigations.

5.6 3D Simulation Model

After completing the preliminary CFD work in 2D, the gained knowledge was transferred to a much more realistic 3D geometry and applied there. The goal of this step was to model a system that corresponds to the actual system. By considering the third dimension, the already mentioned inaccuracies in the 2D CFD simulations based on a general assumption for a virtual depth of the entire domain were eliminated.

5.6.1 Geometry and Mesh

In order to carry out the simulations, 3D geometries were first created for the combustion chamber and the glass tank. For both geometries the walls were resolved geometrically. The reason for this was the arrangement of the measuring points required for validation. Those in the bottom of the glass tank were located inside the wall and as a consequence the heat transport in the wall material had to be considered in the CFD calculation. The geometrical resolution of the walls did not lead to a significant increase of computation costs.

In the 3D geometry of the combustion chamber, at each burner an extended inlet zone was resolved, thus making the modelling of a developed flow possible. With regard to meshing, special attention was given to the reaction zones for cumbustion. One of these zones was shown in Figure 5.26.
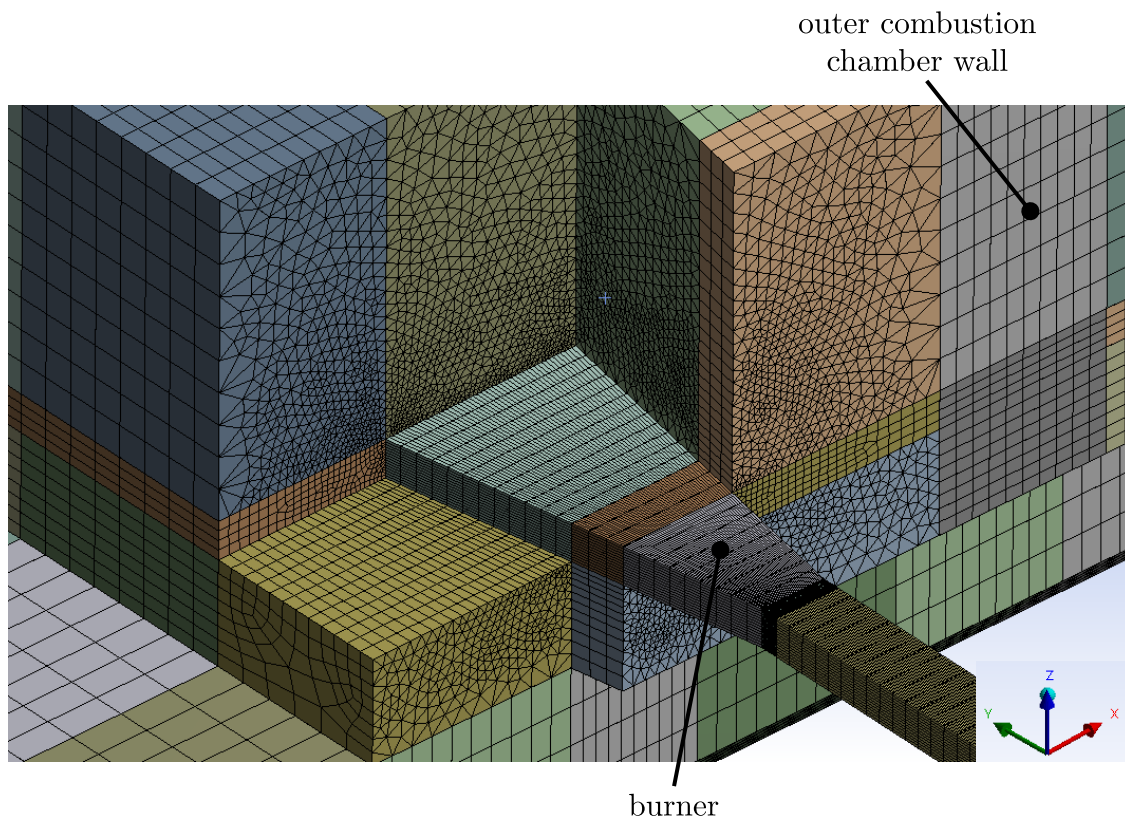
Figure 5.26: 3D mesh grid of the combustion chamber at the burner inlet.

In order to avoid numerical errors, the growth rate was kept low. Additionally, to avoid negative effects of a directional mesh on flame propagation, the directly neighboring areas were meshed with polyhedra elements. Regarding the cell size, the smallest cross sections were resolved with at least six elements along the short side. The combustion chamber walls were resolved with at least five elements in thickness. This was sufficient due to the linear temperature distribution through the solid wall.

In the 3D geometry of the glass tank the batch inlets were resolved with Quads, as depicted in Figure 5.27. Each of the inlets had a cross sectional area of 20 x 40 cm. In contrast to the burner inlets an extended inlet zone was not necessary due to the high viscosity and the low velocity of the glass batch in this region. In order to achieve accurate simulation results at the glass melting zones, the grid was resolved with smaller cells in those regions.
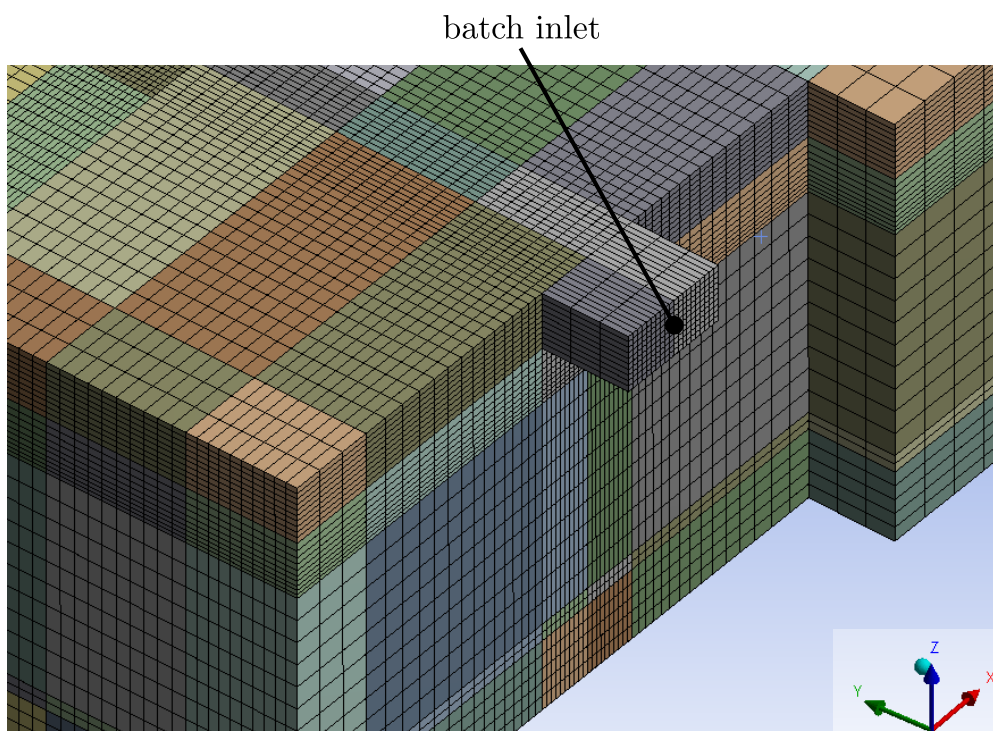
Figure 5.27: 3D mesh grid of the tank at the glass batch inlet.

Furthermore, the six electrodes for electric boosting were modelled as cylinders, which were cut out of the geometry. In the zones close to the electrodes, the mesh was refined to guarantee an appropriate heat transfer and flow. The same strategy was applied to the zones above the electrodes.

The 3D meshes of both submodels had significantly higher numbers of cells. This was due to the increased requirements on mesh accuracy for each of the burners and electrodes. The detailed mesh grid parameters were listed in Table 5.14. The substantially higher number of cells at the combustion chamber was due to the complex task of mesh grid generation at the burners and the regions affected by them. The mesh quality was in an acceptable level with maximum skewness values below 0.9 for both mesh grids and a maximum aspect ratio of 71.3 at the combustion chamber.

Table 5.14: Mesh grid parameters of the 3D submodels.

Submodel	Parameter	Value
Combustion chamber	Number of bodies	3002
	Number of cells	3163190
	Max. skewness (Q_{EAS})	0.90
	Mean skewness (Q_{EAS})	0.22
	Max. aspect ratio	71.29
	Mean aspect ratio	3.55
	Min. orthogonal quality	0.10
	Mean orthogonal quality	0.80
Glass tank	Number of bodies	756
	Number of cells	582599
	Max. skewness (Q_{EAS})	0.76
	Mean skewness (Q_{EAS})	0.024
	Max. aspect ratio	31.16
	Mean aspect ratio	3.59
	Min. orthogonal quality	0.24
	Mean orthogonal quality	0.99

5.6.2 Input- and Model Parameters

The input parameters for the 3D simulation were transferred nearly unchanged from the 2D system coupling. The resolved walls at the combustion chamber and the glass tank were assigned with the refractory material. At the six different burner inlets in the combustion chamber, named in Figure 4.1, the fuel and oxidizer mass flows were defined according to Table 5.15.

Table 5.15: Fuel and oxidator mass flows at the six burners.

	Fuel mass flow $\dot{m}_{CH_4}$ [kg/s]	Oxidator mass flow $\dot{m}_{Ox}$ [kg/s]
B1	0.011	0.054
B2	0.013	0.060
B3	0.015	0.069
B4	0.012	0.057
B5	0.008	0.038
B6	0.008	0.038

For electric boosting in the glass tank, a uniform input of the electrical power at all six electrodes was defined. However, the total power input of $P = 600\,\text{kW}$ was distributed to six cylindrical surface geometries. This resulted in a heat flux of $738.5\,\text{kW/m}^2$ applied to the electrode boundaries. The incoming glass batch mass flow was split equally between the two lateral glass batch inlets with respective mass flows of $0.543\,\text{kg/s}$. Furthermore, the source term for the chemical reaction heat $\dot{Q}_{u,glass}$ in the glass melt was adjusted to the actual glass tank volume V_{GT}. This resulted in a new value according to Equation (5.31).

$$\frac{\dot{Q}_{u,glass}}{V_{GT}} = \frac{-132.3\,\text{kW}}{8.8\,\text{m} \cdot 3.8\,\text{m} \cdot 1.2\,\text{m}} = \textbf{-3.3\,kW/m}^3 \tag{5.31}$$

In order to estimate the influence of different parameters on the simulation results, three different simulations were carried out in total. The settings of all 3D simulations are listed in Table 5.16. In the first simulation (Sim V1) no batch chemistry was considered yet. In the next two simulations (Sim V2 and Sim V3) the negative source term for the chemical reaction heat was considered as well as the CO_2 released from the glass batch in the oxidizer mass flows. Thus, the amount of the released CO_2 was subtracted from the mass flow of the incoming glass batch and subsequently considered in the oxidizer mass flow at the combustion chamber proportionally to the individual burner capacities. In Sim V3, however, slightly increased values of the thermal conductivities for the refractory material at the combustion chamber and at the glass tank were assumed.

Table 5.16: Parameters of the different simulation settings.

	$k_{CC,W}$ [W/m K]	$k_{GT,W}$ [W/m K]	Source term [kW/m³]	CO_2 in $\dot{m}_{Ox}$?
Sim V1	1.5	3	0	no
Sim V2	1.5	3	-3.3	yes
Sim V3	2	4	-3.3	yes

5.6.3 Validation of the Simulation Results

To guarantee an operation of the glass melting furnace at the most efficient point, temperatures are continuously measured with thermocouples (TC) at several locations. The measuring points were named with TC1-TC6 at the positions given in Figure 5.28. For validation of the simulation results the temperature values of these six measuring points were recorded and stored by an external software. In particular, three measuring points at the furnace crown and three measuring points in the glass tank insulation were used to verify the numerical models presented here. The measured temperatures at the different thermocouples were noted in Figure 5.28. The used thermocouples were of type B in tolerance class 3 and had a sheath diameter of 15 mm. Since glass melting furnaces are operated in steady-state, deviations of the measured temperatures were small and within the tolerance of the thermocouples with about 0.5 % of the measured value.

In Figure 5.29 the computed temperatures in the simulations were compared to the measured values. In Figure 5.30 the absolute deviations E_{abs} of the simulation values T_{Sim} to the measured temperatures T_{Meas} are shown at the top and the relative deviations E_{rel} are depicted at the bottom. The formulations of the absolute and relative deviation are given in Equations (5.32) and (5.33).

$$E_{abs} = T_{Sim} - T_{Meas} \tag{5.32}$$

$$E_{rel} = \frac{T_{Sim} - T_{Meas}}{T_{Meas}} \tag{5.33}$$
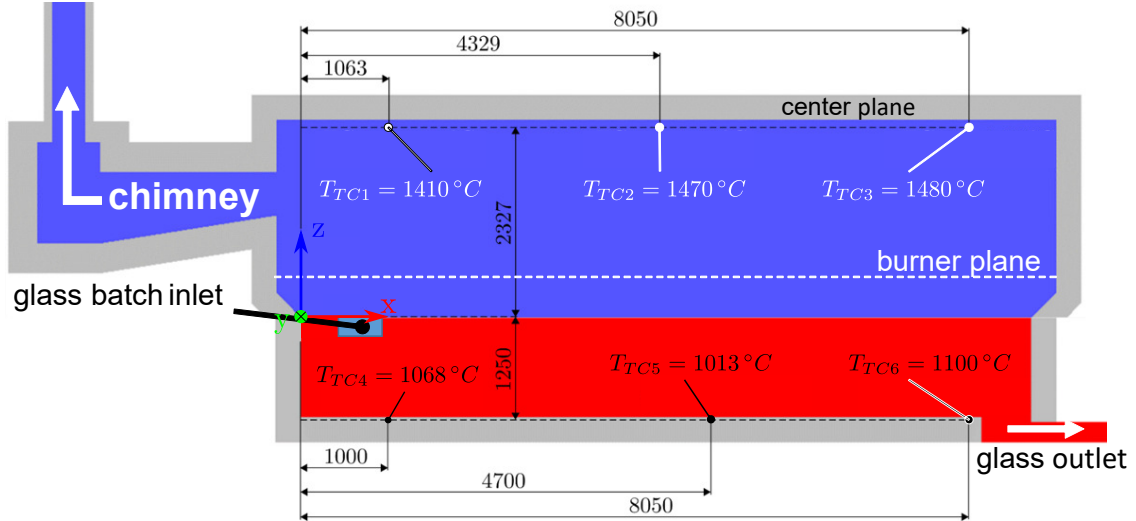
Figure 5.28: Schematic structure of the system and location of the thermocouples.

Due to the abscence of the source term, in Sim V1 the highest temperatures were computed with a maximum absolute deviation of 137.7 K at TC1 and a maximum relative deviation of 9.55 % at TC5. If the source term was taken into account for the whole glass tank with a negative heat flux density of -3.3 kW/m³, the results were within the desired tolerance range. This was especially the case in Sim V2, where the maximum absolute deviation of 53.7 K at TC1 and a maximum relative deviation of 3.7 % at TC5 was calculated. All values in Sim V2 were within the desired range of $E_{rel} \leq \pm 5$ %. Thus, the correctness of the presented numerical models was confirmed. During the validation it was also found that in Sim V3 the lowest temperatures in the combustion chamber and in the glass tank were computed. This was reasonable and at the same time the applicability of the thermal conductivity values for the refractory material provided by the project partner was confirmed.
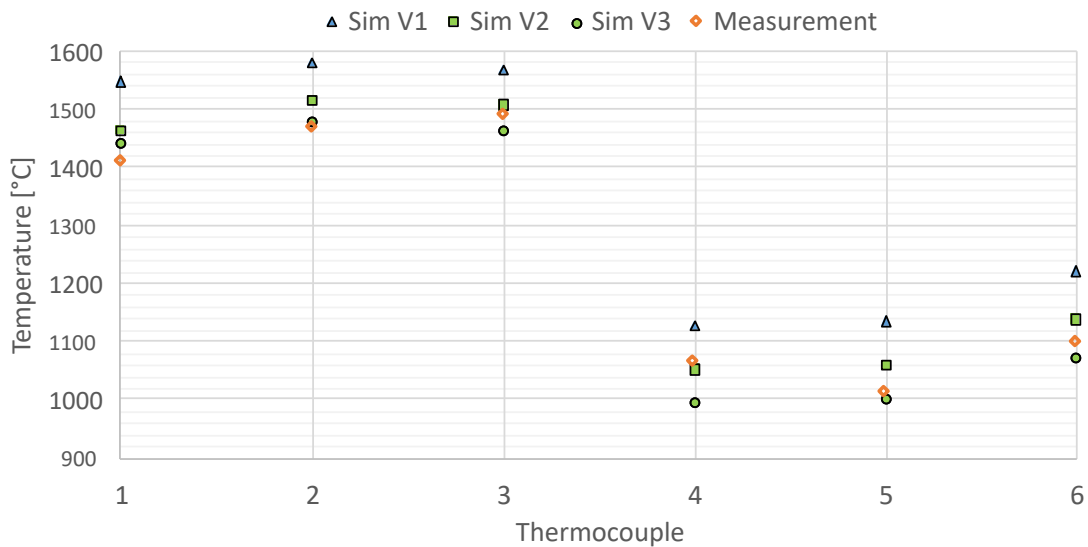
Figure 5.29: Comparison of the computed 3D simulation values with the measurements.
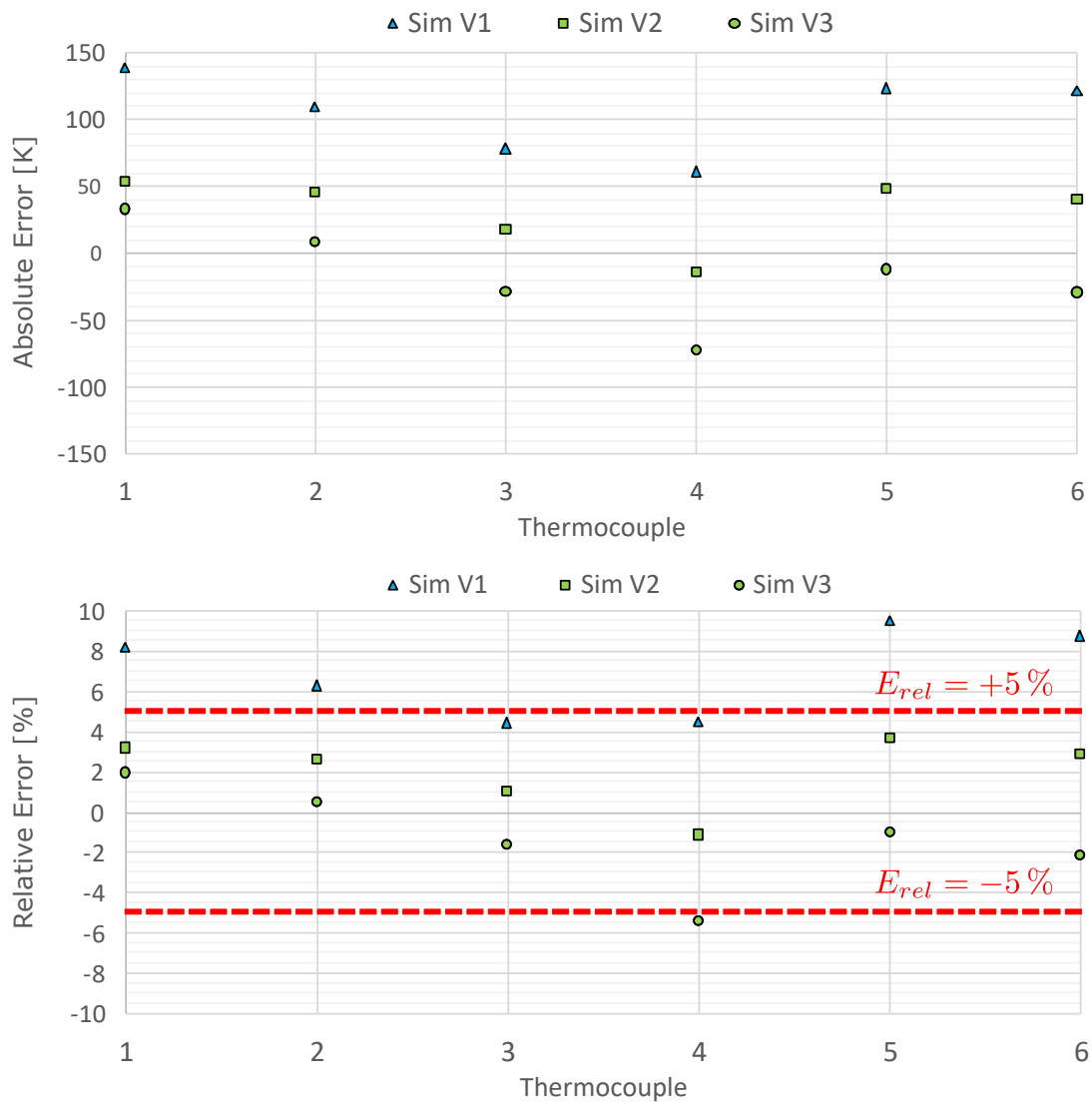
Figure 5.30: Absolute deviations (top) and relative deviations (bottom) between the 3D simulations and the measurements.

Based on the validation of the simulation results, Sim V2 was determined as the simulation setting that best represents the physical glass melting furnace. For this reason, Sim V2 was considered for all further investigations.

5.6.4 Discussion and Results

Subsequently, the results of the validated 3D simulation were analyzed in detail. In Figure 5.31 the temperature and velocity field in the center plane of the glass melting furnace is depicted. Overall, the temperature field in the combustion chamber indicated a reasonable temperature distribuition with maximum temperatures at around 1800 °C in the burner flames. Towards the chimney, the flue gas temperature decreased to a level of about 1400 °C. The variable fuel supply at the burners led to the formation of a hot spot in the burner plane slightly behind the center of the glass surface. The burner with high fuel supply generated more heat input, which was indicated by the big red zones at the inner burners. A look to the glass surface showed a tendency to high temperatures below the inner burners. This fact could lead to the formation of a hot spot on the glass surface. A hot spot would be even desired to support the essential convection vortices in the glass tank. The slightly elevated red spots of the outer burners, especially of the burner at close to the outlet, indicated there an upwards deflection of the burner flames towards the furnace crown due to the low stream velocity in relation to the thermal lift. This undesired effect had the consequence of a non-ideal heat transfer between these burners and the glass tank. The thermal lifting effect was further evident in the computed temperatures, which showed a maximum in all three simulations at TC2.

The velocity field in Figure 5.31 at the bottom is dominated by the momentum input of the oxy-fuel burners. The effects of individual fuel supply at the burners were also visible here. For instance, at high speeds, colored in red, the burners operated at a high power input. In the further course the burned flue gases streamed primarily along the glass surface towards the chimney and the flue gas outlet. In the central plane, an insignificant part of the flue gases also reached the chimney via the furnace crown. Another interesting aspect was the rather high velocity in the entrance region of the chimney.
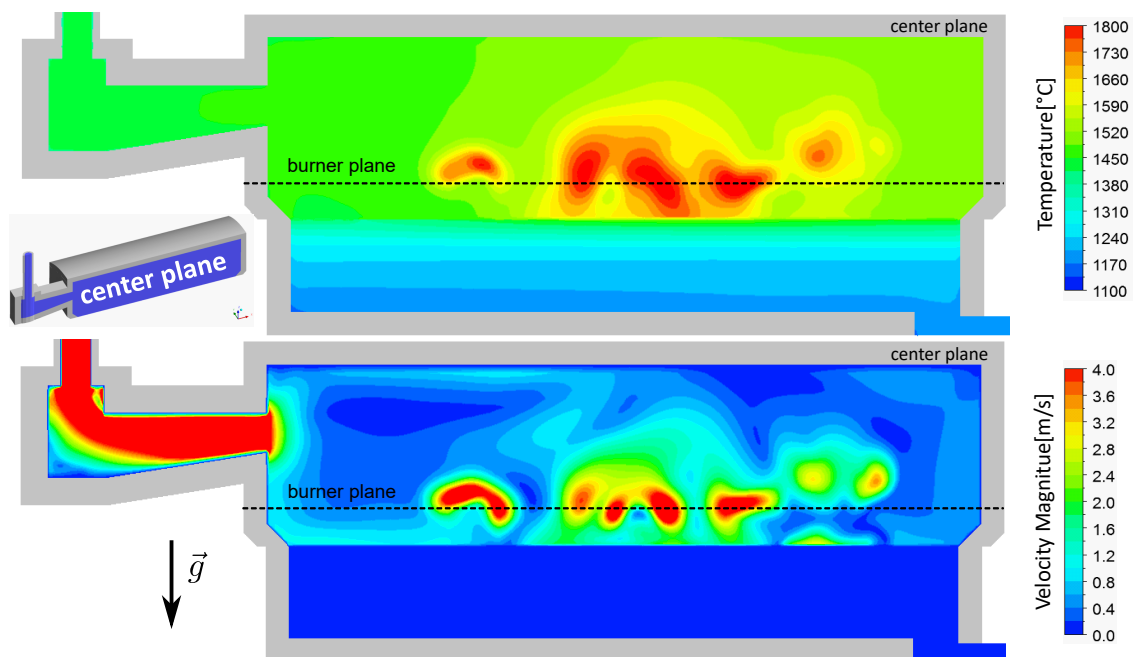
Figure 5.31: Temperature and velocity field in the center plane of the glass melting furnace.

In Figure 5.32 the velocity magnitudes, streamlines and direction vectors in the burner plane were combined. Additionally the velocities of the fuel and the oxidator at the inlet were given individually for each burner. The different velocities with a maximum velocity for the fuel at burner B3 caused different characteristics of the flow field at each burner. Furthermore, mutual influences of the burners were observed due to their crosswise arrangement. A first look at the velocity field made clear, that the flame fronts of burner B2 and burner B3 clashed in the center plane. This led to a mutual reduction of the momentum at both streams. The heat transfer over the glass surface therefore had some potential for improvements. However, this deficit could be eliminated by changing the position of burner B2. Apart from this, the flame lengths reached an almost ideal level and slightly exceeded the center plane of the combustion chamber at high fuel input. With ideal crosswise arrangement of the burners, larger overlaps than those seen here are still possible. The streamlines indicated a movement of the burned flue gases along the side wall at the opposite side of the particular burner. The flow continued towards the middle of the front wall to the entrance of the chimney. Additionally, some secondary vortices were detected in the corners of the combustion chamber.
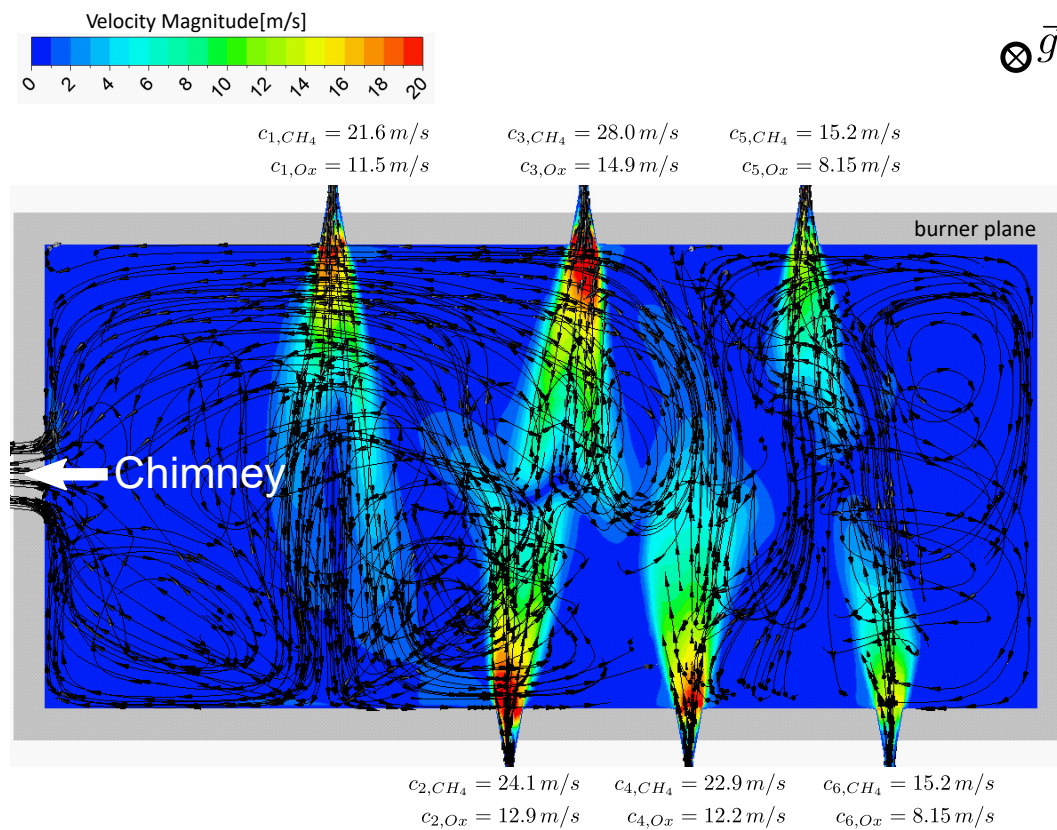
Figure 5.32: Velocities, streamlines and direction vectors in the burner plane.

Furthermore, Figure 5.33 showed the temperature distribution on the glass surface. Additionally, all cells in the combustion chamber with a flame temperature above $1900\,°C$ were marked in red. This allowed to identify the flame pattern in the combustion chamber and to discuss its effects on the glass surface. Blue color tones in the temperature distribution indicated the regions where the glass batch was inserted into the glass tank as bulk material. The enormous temperature rise from $27\,°C$ to more than $930\,°C$ within a few centimeters immediately behind the glass batch inlets was remarkable. Consequently, a temperature gradient from the glass batch inlets towards the

glass outlet was observed with a global maximum above the electrodes $E_1 - E_6$. In the region of the electrodes the formation of a hot spot was observed, as it should be present on the surface of the glass melt according to literature [11]. In addiation to the the very high fuel input in this region, the formation of the hot spot was also supported by the heat input via electric boosting at the electrodes. Nevertheless, unaffected by electric boosting the heat input into the glass melt in the vicinity of the burners became clearly visible. A further effect on the glass surface was recognized below the entrance to the chimney. Immediately in front of the entrance there was a local maximum, as all the hot flue gases had to pass this place for leaving the combustion chamber. In general, the temperature on the glas surface outside the two melting zones was in a range of 1350-1500 °C.
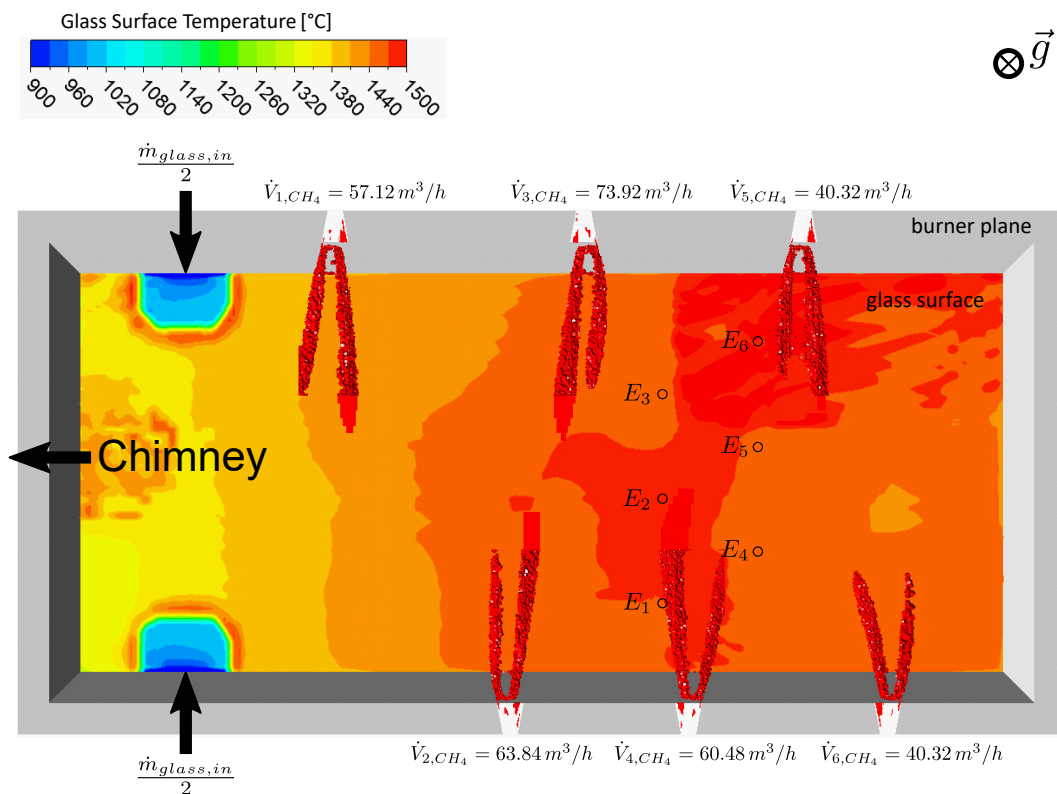
Figure 5.33: Temperature distribution at the glass surface.

The temperature distribution in several planes at the glass tank was shown in Figure 5.34. The center plane is a xz-plane at $y = 0$ mm. The inlet plane is a yz-plane at $x = 1000$ mm and the electrode planes are yz-planes at $x = 5550$ mm and $x = 6450$ mm. In the center plane a uniform temperature distribution of the thermal layering was achieved across the glass tank. The temperatures at the bottom of the tank were around 1170 °C and at the glass surface around 1500 °C. At the glass outlet a temperature of 1090 °C was reached. Obviously the thermal separation due to the barrier effect of the electrodes in 2D was not present anymore in the glass tank. Due to this fact, the chosen procedure was confirmed despite the unavoidable thermal separation in 2D. In the inlet plane a rapid melting of the glass batch was observed with an expansion of the glass batch blanket of about 0.5 m at each inlet. At the electrode planes only an influence on the glass temperature limited to a small area next to the electrode shell was detected. In contrast, considerable influence on the temperature above the electrodes was detected. A possible reason could be lifting effects and thus a rapid rise of the hot glass melt on the shell surfaces.
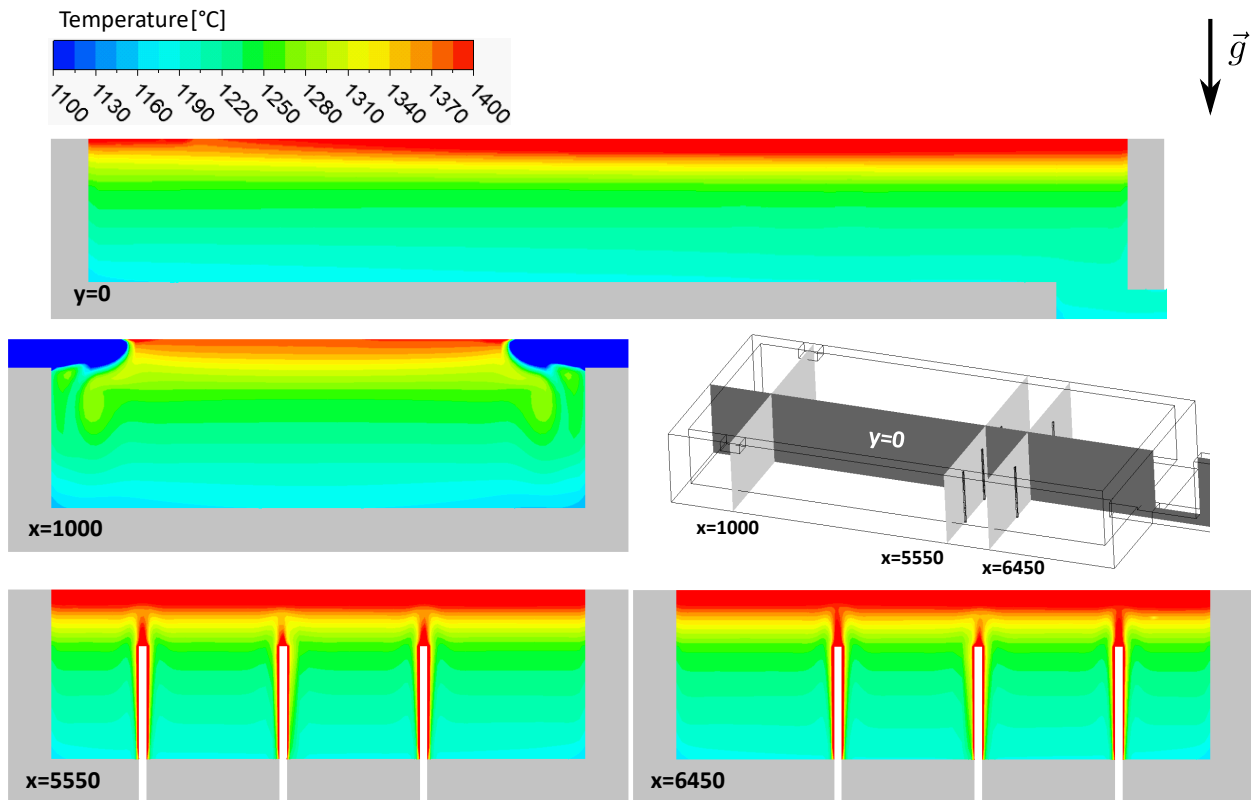
Figure 5.34: Temperature distribution in the glass tank in several planes.

The flow fields with streamlines and direction vectors at the glass tank in Figure 5.35 underlined the laminar character of the flow in the glass tank with maximum velocities in the range of 5 mm/s. With the flow fields in the center plane and the inlet plane the flow pattern of the glass was characterized. Behind the inlet, the glass batch material sank to the bottom of the glass tank, where melting already occured. The melt continued movement towards the heating electrodes, where it rised due to natural convection to the glass surface and moved back at the surface towards the inlets on both sides. This resulted in the formation of a primary vortex, which supported the melting process, mixing and the removal of batch gases in the glass melt. The presence of this vortex in the 3D simulation results was a further confirmation of the 3D CFD model. In the electrode planes, flow velocities above 5 mm/s were observed both laterally and above the electrodes. As already suspected before, the lateral influence of the flow field was less than the influence above the electrodes. From this it was derived that due to the lifting effects by electric boosting the glass melt was transported almost to the glass surface.
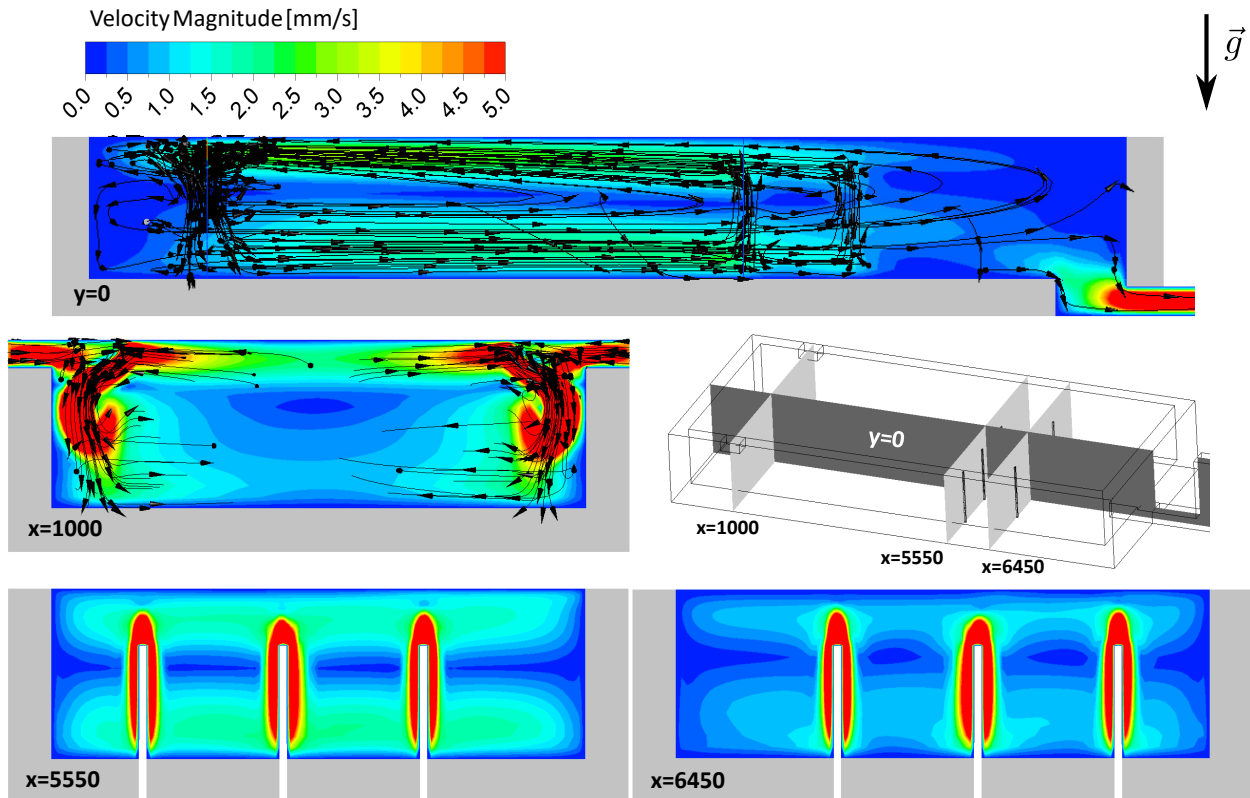
Figure 5.35: Velocities, streamlines and direction vectors in the glass tank in several planes.

Finally, the main advantages of the developed numerical method are briefly summarized here. The model differs from state-of-the-art calculation models in so far, that:

1. Previous calculation models did not take into account the mixture gases that rise into the combustion chamber during the melting of the raw material mixture. The developed model achieves this by using a verified combustion model, the "partially premixed steady diffusion flamelet model", in combination with a precise combustion chemistry, the "skeletal25" reaction mechanism.

2. Existing coupling mechanisms assume either a highly simplified glass melting furnace geometry or a simplification of the heat transport on the glass surface. The developed model considers both, convection and radiation, and introduces a rigorous termination criterion based on metrological considerations.

Compared to all previous simulations in 2D, the 3D simulations were significantly more time-consuming. Usually the iterative procedure converged after seven iteration steps. On a six-core processor the first iteration step of the combustion chamber as well as of the glass tank was quite expensive in terms of time and it required one week for each submodel until convergence was reached. All further iteration steps of the combustion chamber in 3D took about 12 hours per step and for the glass tank about seven days per step.

6 Conclusion and Outlook

In the scope of this work, the heat transfer in a continuous glass melting furnace was analysed using CFD, with a focus on the temperature and flow distributions. For this purpose, a coupled simulation model consisting of two interacting submodels was developed with the software package Ansys Fluent 19.0. The simulation results were validated with experimental data from wall temperature measurements in the combustion chamber and glass tank. The programme CFD-Post 19.0 was used to evaluate the results.

Due to the high computation costs in 3D, the simulation model was first developed and tested in 2D to check it for plausibility. At the beginning, stand-alone simulations were developed for the two submodels, the combustion chamber and the glass tank. In addition to the investigation of combustion models in the gas phase, different radiation models and absorption coefficients for the glass melt were scrutinized. As a result, a balance between cost and accuracy for further simulations was found. By implementing the system coupling in 2D it was possible to point out the shortcomings of an exclusive 2D approach and underline the necessity of 3D simulations. In 3D, simulations with and without the consideration of batch melting chemistry were conducted.

The stand-alone simulation results of the combustion chamber and the glass tank in 2D indicated that the boundary conditions were chosen correctly. At the glass tank, the best results were achieved with an absorption coefficient of 125 1/m. For the chosen coupling procedure the successful proof of concept was provided in the 2D case, even if the results were not representative due to the high degree of modelling. In the validation of the subsequent 3D simulations, the configuration with thermal conductivities of the refractory material of $k_{CC,W}$ = 1.5 W/(m K) and $k_{GT,W}$ = 3 W/(m K), as recommended by the project partner, achieved the best results. The relative temperature deviation of this solution was below 5 % in each of the six measuring points. Based on the temperature and flow fields, a rapid melting of the glass batch was observed in the glass tank, as well as the formation of a primary vortex to support the melting process, mixing and the removal of batch gases from the melt. The maximum velocity of the laminar flow in the glass melt was around 5 mm/s. The supporting effect of electric boosting could be clearly demonstrated in the CFD simulations. The glass melt showed temperatures in a range of 1090 °C at the glass outlet and close to 1500 °C at the glass surface. In the combustion chamber a high thermal input into the glass tank was achieved by the crosswise arrangement of the burners.

However, the following two factors had a negative effect on heat transfer and thus also on the specific heat demand for glass production: First, the burner axes of the opposite facing burners B2 and B3 had a small horizontal offset. The reciprocal deflection of their respective flame fronts reduced the momentum of flame expansion. Second, as a result of the relatively low burner velocities, the thermal lift from the glass melt deflected the flames upwards to the furnace crown, thus further reducing the heat transfer at the glass surface.

In order to increase the efficiency of glass production, a reduction of the negative effects on heat transfer can be achieved by: First, increasing the horizontal spacing between burner axes of B2 and B3 and second, by installing burners with a smaller cross-section at the inlet, which would increase the flow velocity.

For the further utilization and optimization of the presented CFD simulation model two approaches are proposed:

- Parameter studies are recommended for the investigation of the influence of parameter changes on the simulation results. Purpose of the parameter studies is to find the optimum operating point for the glass melting furnace. The major goal is glass production with the lowest possible emissions and fuel consumption. Parameters to optimize are the emissions and fuel consumption per kg melted glass.

- Further optimization can be achieved by the implementation of "Bubbling" into the existing numerical model. With bubbling the last remaining batch gases in the glas melt are discharged through the glass surface into the combustion chamber by means of lifting forces. For this purpose, nitrogen or air bubbles are injected into the melt at the bottom of the glass tank.

Bibliography

[1]   A. Abbassi and Kh. Khoshmanesh. "Numerical simulation and experimental analysis of an industrial glass melting furnace". In: *Applied Thermal Engineering* 28.5 (Apr. 1, 2008), pp. 450–459. ISSN: 1359-4311. DOI: 10.1016/j.applthermaleng.2007.05.011 (cit. on p. 59).

[2]   Bengt Andersson, Ronnie Andersson, Love Håkansson, Mikael Mortensen, Rahman Sudiyo, and Berend van Wachem. *Computational Fluid Dynamics for Engineers*. Dec. 2011. DOI: 10.1017/CBO9781139093590 (cit. on pp. 11, 13, 14, 17, 20).

[3]   Ansys Inc. "ANSYS Fluent Meshing User's Guide Release 18.2". 2017 (cit. on pp. 15, 16).

[4]   Ansys Inc. "Fluent Theory Guide Release 18.2". 2017 (cit. on pp. 17–20).

[5]   Hans Dieter Baehr and Karl Stephan. *Wärme- und Stoffübertragung*. Berlin, Heidelberg: Springer Berlin Heidelberg, 2019. ISBN: 978-3-662-58440-8 978-3-662-58441-5. DOI: 10.1007/978-3-662-58441-5 (cit. on pp. 3, 5).

[6]   Charles E. Baukal Jr. *Oxygen-Enhanced Combustion, Second Edition*. Google-Books-ID: Pxes4hlDmkIC. CRC Press, Mar. 15, 2013. 795 pp. ISBN: 978-1-4398-6228-5 (cit. on p. 1).

[7]   Peter Böckh and Thomas Wetzel. *Wärmeübertragung*. 7. Berlin, Heidelberg: Springer Berlin Heidelberg, 2017. ISBN: 978-3-662-55479-1 978-3-662-55480-7. DOI: 10.1007/978-3-662-55480-7 (cit. on p. 6).

[8]   Manoj K. Choudhary, Bruno Purnode, Adriaan Marinus Lankhorst, and Andries F. J. A. Habraken. "Radiative heat transfer in processing of glass-forming melts". In: *International Journal of Applied Glass Science* 9.2 (2018), pp. 218–234. ISSN: 2041-1294. DOI: 10.1111/ijag.12286 (cit. on pp. 53, 59).

[9]   Wilmington Instrument Co. *Bulk Density*. Ed. by BinMaster. 2015. URL: https://www.binmaster.com/_resources/dyn/files/75343622z9caf67af/_fn/Bulk+Density.pdf (visited on 12/11/2019) (cit. on p. 50).

[10]   Reinhard Conradt. "The Glass Melting Process-Treated as a Cyclic Process of an Imperfect Heat Exchanger". In: *Ceramic Transactions Series*. Ed. by James R. Varner, Thomas P. Seward, and Helmut A. Schaeffer. Hoboken, NJ, USA: John Wiley & Sons, Inc., Apr. 20, 2012, pp. 35–44. ISBN: 978-1-118-40594-9 978-1-57498-156-8. DOI: 10.1002/9781118405949.ch2 (cit. on pp. 35, 36).

[11]   Reinhard Conradt. "Werkstoffverarbeitung Glas". Aachen, July 2008 (cit. on pp. 1, 29, 30, 73).

[12] Zhijun Feng, Dongchun Li, Guoqiang Qin, and Shimin Liu. "A New Method to Optimize Furnace Designs Using Daily Flow Rates to Maximize Energy Savings in the Steady Production". In: *Journal of the American Ceramic Society* 92.10 (2009), pp. 2459–2462. ISSN: 1551-2916. DOI: 10.1111/j.1551-2916.2009.03235.x (cit. on p. 59).

[13] Joel H. Ferziger and M. Perić. *Computational methods for fluid dynamics*. 3rd, rev. ed. Berlin ; New York: Springer, 2002. 423 pp. ISBN: 978-3-540-42074-3 (cit. on p. 22).

[14] Heinz Herwig and Andreas Moschallski. *Wärmeübertragung*. 3. Wiesbaden: Springer Fachmedien Wiesbaden, 2014. ISBN: 978-3-658-06207-1 978-3-658-06208-8. DOI: 10.1007/978-3-658-06208-8 (cit. on p. 10).

[15] Jack P Holman. *Heat Transfer*. 10th ed. Mc Graw-Hill series in mechanical engineering. Boston: Mc-Graw-Hill, 2010. 725 pp. ISBN: 978-0-07-352936-3 (cit. on p. 3).

[16] Ansys Inc. "Fluent User's Guide Release 18.2". 2017 (cit. on p. 16).

[17] Eckart Laurien and Herbert Oertel. *Numerische Strömungsmechanik*. Wiesbaden: Springer Fachmedien Wiesbaden, 2018. ISBN: 978-3-658-21059-5 978-3-658-21060-1. DOI: 10.1007/978-3-658-21060-1 (cit. on pp. 9, 10).

[18] Stefan Lecheler. *Numerische Strömungsberechnung*. Wiesbaden: Springer Fachmedien Wiesbaden, 2014. ISBN: 978-3-658-05200-3 978-3-658-05201-0. DOI: 10.1007/978-3-658-05201-0 (cit. on p. 17).

[19] F. Moukalled, L. Mangani, and M. Darwish. *The Finite Volume Method in Computational Fluid Dynamics*. Vol. 113. Fluid Mechanics and Its Applications. Cham: Springer International Publishing, 2016. ISBN: 978-3-319-16873-9 978-3-319-16874-6. DOI: 10.1007/978-3-319-16874-6 (cit. on pp. 7, 8, 17).

[20] Peter Mullinger and Barrie Jenkins. *Industrial and Process Furnaces*. 2nd ed. Elsevier, 2013. ISBN: 978-0-08-099377-5. DOI: 10.1016/B978-0-08-099377-5.01001-7 (cit. on p. 1).

[21] L. David Pye, Angelo Montenero, and Innocent Joseph, eds. *Properties of glass-forming melts*. Boca Raton: Taylor & Francis, 2005. 485 pp. ISBN: 978-1-57444-662-3 (cit. on p. 50).

[22] H. Schlichting and Klaus Gersten. *Grenzschicht-Theorie*. 10. Springer-Verlag, May 1, 2006. 804 pp. ISBN: 978-3-540-32985-5 (cit. on pp. 8, 10, 11).

[23] Rüdiger Schwarze. *CFD-Modellierung*. Berlin, Heidelberg: Springer Berlin Heidelberg, 2013. ISBN: 978-3-642-24377-6 978-3-642-24378-3. DOI: 10.1007/978-3-642-24378-3 (cit. on pp. 14, 15).

[24] J. E. Shelby. *Introduction to Glass Science and Technology*. 2nd ed. Royal Society of Chemistry, 2005. 316 pp. ISBN: 978-0-85404-639-3 (cit. on pp. 27–29).

[25] Termo Refractaires. *Refractories for Glass Furnaces*. Oct. 30, 2019. URL: https://termorefractaires.com/en/applications/glass-furnace.html (visited on 10/30/2019) (cit. on p. 41).

[26]   Wolfgang Trier. *Glasschmelzöfen*. Berlin, Heidelberg: Springer Berlin Heidelberg, 1984. ISBN: 978-3-642-82068-7 978-3-642-82067-0. DOI: 10.1007/978−3−642−82067−0 (cit. on p. 29).

[27]   Jiyuan Tu, Guan Heng Yeoh, and Chaoqun Liu. *Computational fluid dynamics: a practical approach*. 2nd ed. Amsterdam: Elsevier/Butterworth-Heinemann, 2013. xiii+440. ISBN: 978-0-08-098277-9 (cit. on p. 23).

[28]   Frank M. White. *Fluid Mechanics*. seventh edition. McGraw Hill, 2011. 862 pp. ISBN: 978-0-07-352934-9 (cit. on p. 7).

[29]   Zhengzhou Sunrise Refractory Co., Ltd. *Refractories,Fire Refractory,Fire Brick,Insulation Refractory,high temperature refractory*. URL: https://www.sunriserefractory.com/products/ (visited on 10/12/2020) (cit. on p. 41).

List of Figures

List of Tables